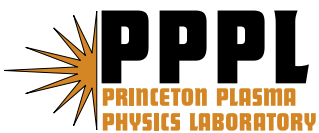


**Status of Recent Experimental and Analytical Investigation
of MHD-induced Energetic Ion Redistribution or Loss
in the National Spherical Torus Experiment**

S.S. Medley, R. Andre, R.E. Bell, D.S. Darrow, E.D. Fredrickson, N.N. Gorelenkov,
S.M. Kaye, F.M. Levinton, B.P. LeBlanc, J.E. Menard, D. Stutman,
A.L. Roquemore, K. Tritz, H. Yuh and the NSTX Team

April 2007



Princeton Plasma Physics Laboratory

Report Disclaimers

Full Legal Disclaimer

This report was prepared as an account of work sponsored by an agency of the United States Government. Neither the United States Government nor any agency thereof, nor any of their employees, nor any of their contractors, subcontractors or their employees, makes any warranty, express or implied, or assumes any legal liability or responsibility for the accuracy, completeness, or any third party's use or the results of such use of any information, apparatus, product, or process disclosed, or represents that its use would not infringe privately owned rights. Reference herein to any specific commercial product, process, or service by trade name, trademark, manufacturer, or otherwise, does not necessarily constitute or imply its endorsement, recommendation, or favoring by the United States Government or any agency thereof or its contractors or subcontractors. The views and opinions of authors expressed herein do not necessarily state or reflect those of the United States Government or any agency thereof.

Trademark Disclaimer

Reference herein to any specific commercial product, process, or service by trade name, trademark, manufacturer, or otherwise, does not necessarily constitute or imply its endorsement, recommendation, or favoring by the United States Government or any agency thereof or its contractors or subcontractors.

PPPL Report Availability

Princeton Plasma Physics Laboratory:

<http://www.pppl.gov/techreports.cfm>

Office of Scientific and Technical Information (OSTI):

<http://www.osti.gov/bridge>

Related Links:

[U.S. Department of Energy](#)

[Office of Scientific and Technical Information](#)

[Fusion Links](#)

Status of Recent Experimental and Analytical Investigation of MHD-induced Energetic Ion Redistribution or Loss in the National Spherical Torus Experiment

S. S. Medley¹, R. Andre¹, R. E. Bell¹, D. S. Darrow¹, E. D. Fredrickson¹, N. N. Gorelenkov¹, S. M. Kaye¹, F. M. Levinton², B. P. LeBlanc¹, J. E. Menard¹, D. Stutman³, A. L. Roquemore¹, K. Tritz³, H. Yuh² and the NSTX Team

¹Princeton Plasma Physics Laboratory, Princeton, New Jersey, 08543, USA

²Nova Photonics, Inc., Princeton, NJ 08543 USA

³Johns Hopkins University, Baltimore, Maryland, USA

Email: medley@pppl.gov

Abstract

The National Spherical Torus Experiment (NSTX) is particularly well suited to investigate fast-ion driven instabilities because large values of the dimensionless parameters $v_{fast}/v_{Alfvén}$ and $\beta_{fast}(0)/\beta_{tot}(0)$ required to drive such instabilities occur routinely in neutral beam heated plasmas. The instabilities can be divided into three categories; chirping Energetic Particle Modes (EPM) in the frequency range 0 – 120 kHz, the Toroidal Alfvén Eigenmodes (TAE) with a frequency range of 50 – 200 kHz and the Global and Compressional Alfvén Eigenmodes (GAE and CAE, respectively) between 300 kHz and the ion cyclotron frequency. These modes are of particular interest because of their potential to cause substantial fast ion redistribution or loss. Both the volume-integrated neutron and the line-integrated charge exchange neutral particle diagnostics show signal depletion due to fast-ion driven instabilities, but cannot distinguish between fast-ion redistribution or loss. Two recently implemented diagnostics on NSTX, the Motional Stark Effect (MSE) and scintillator Fast Lost Ion Probe (sFLIP), facilitate separation of redistribution and loss effects. In discharges with significant MHD activity, outward redistribution of the core-peaked energetic beam ions modifies the beam-driven current profile and hence the core q-profile. MSE-constrained q-profiles are being used to assess this effect. sFLIP measures the pitch and energy of fast ions that are ejected from the plasma and intercept the wall-mounted probe thus identifying fast-ion loss. For certain H-mode discharges where NPA measurements of the NB energetic ion spectra exhibit MHD-

induced fast-ion depletion, the sFLIP data confirm the existence of an ion loss that occurs primarily for passing particles near the NB full injection energy. Observations and TRANSP simulations representing fast ion instability-induced redistribution or loss phenomena in NSTX are presented.

1.0 Introduction

The National Spherical Torus Experiment (NSTX) [1] is a midsize low aspect ratio fusion research facility with auxiliary heating from Neutral Beam Injection (NBI) and High Harmonic Fast Wave (HHFW) launch. Typical NSTX parameters are major radius $R_0 = 0.85 - 0.9$ m, minor radius $a = 0.67$ m resulting in an aspect ratio of $A = R_0/a \sim 1.3$, plasma current $I_p = 0.3 - 1.5$ MA and toroidal field $B_T = 0.3 - 0.6$ T. Three co-directed deuterium neutral beam sources have injected power up to $P_{NB} = 7$ MW at full neutral energies up to $E_b = 100$ keV. HHFW heating at 30 MHz has delivered up to $P_{RF} \sim 6$ MW to deuterium and helium plasmas.

Determining the attractiveness of the spherical torus concept [2] in the areas of high- β stability, confinement, non-inductive current drive and divertor physics for pulse lengths much longer than the energy confinement time is the mission of the NSTX device. The performance milestones that were achieved to date in NSTX have been reported elsewhere [3-5]. H-modes triggered by NBI heating are routinely obtained in NSTX and have become a standard operational scenario [6]. L-H transitions triggered by NBI heating have been obtained over a wide parameter range in $I_p \leq 1.2$ MA, $B_T \leq 5.5$ kGauss, and $n_e \leq 8 \times 10^{13}$ cm⁻³ in either lower-single-null or double-null diverted discharges with elongation $\kappa \leq 2.6$, triangularity $\delta \leq 0.85$ and plasma pulse length exceeding 1.5 s. To date NSTX has achieved, non-simultaneously, stored energies up to 0.39 MJ, energy confinement times $\tau_E \leq 0.12$ s and $\beta_T \leq 40\%$; $\beta_T = \langle p \rangle / (B_0^2 / 2\mu_0)$ where $\langle p \rangle$ is the volume averaged total pressure and B_0 is the vacuum magnetic field at R_0 .

The physics of plasmas that contain large populations of super-Alfvénic energetic particles is an important outstanding issue for burning plasma experiments, such as ITER. Significant energetic ion loss could degrade performance or damage first wall structures.

The National Spherical Torus Experiment (NSTX) is particularly well suited to investigate fast-ion driven instabilities and their influence on fast particle confinement, since the NBI heated plasmas can match or exceed the ITER dimensionless parameter regime for $v_{fast}/v_{Alfvén}$ and $\beta_{fast}(0)/\beta_{tot}(0)$ as demonstrated in Fig. 1 (albeit at much higher fast-ion ρ^*). As illustrated by the Mirnov spectrogram shown in Fig. 2, a wide variety of fast ion driven instabilities are excited during high-power NBI in NSTX. TAEs [7] and other Alfvén eigenmodes [8] are destabilized when the fast-ion velocity v_b is larger than the Alfvén speed v_A . The modes can be divided into three categories; chirping Energetic Particle Modes (EPM) in the frequency range 0 – 120 kHz, the Toroidal Alfvén Eigenmodes (TAE) with a frequency range of 50 – 200 kHz and the Global and Compressional Alfvén Eigenmodes (GAE and CAE, respectively) between 300 kHz and the ion cyclotron frequency. Some of the higher frequency modes exhibit a frequency splitting characteristic of what would be expected from “hole-clump” theory [9]. The TAEs can appear either as saturated modes or as bursting modes and the bursting TAEs observed in NSTX [10] can cause significant fast ion losses. Compressional Alfvén modes (CAE) have a frequency scaling, polarization, dependence on the fast-ion distribution function, and low frequency limit that are qualitatively consistent with CAE theory. Thus far, CAE and GAE modes do not appear to cause fast ion loss in NSTX.

In addition to Alfvénic modes, energetic ion redistribution associated with low frequency internal kink-type magnetohydrodynamic (MHD) activity has been observed [11,12]. Outward redistribution of the core-peaked energetic beam ions due to Alfvénic modes can modify the NBI-driven current profile and hence the core q-profile, as also reported in DIII-D [13, 14].

If MHD-induced energetic ion redistribution is sufficiently severe then ion loss to the NSTX first-wall structures can occur in addition to bad-orbit driven prompt loss to the walls. The prompt loss of neutral beam ions from NSTX is expected to be between 12% and 42% of the total beam power [33]. Such losses are diagnosed either from temperature measurements of ion deposition on first wall structures or by Faraday cup probes [15] which detect ions on loss orbits. Losses of ions with energy above 1 keV in NSTX have been measured with a Faraday cup probe located at the vessel mid-plane [16]. In addition

to prompt loss to first wall structures, orbit excursions beyond the separatrix combined with high atomic and molecular density enveloping the plasma can result in a depletion of the energetic ion population due to the energy dependent charge exchange losses and a potentially ensuing ‘bump-on-tail’ in the energetic ion distribution [17] that could lead to further loss processes.

Resonant interaction of high-energy particles with magnetic perturbations in toroidal devices can produce large-scale modification of the particle distribution, sometimes leading to particle loss. Spherical tokamaks, including NSTX [18 - 20], START [21] and MAST [22, 23], are particularly susceptible to fast ion driven instabilities, due primarily to their relatively low toroidal field, but also in some instances due to the direct effect of the low aspect ratio. The Alfvénic modes are readily excited in NSTX as the neutral beam full energy ion velocity is typically two to four times the Alfvén speed and because the Larmor radius of the fast ions is large compared to the minor radius, enhancing mode-particle interactions. Several classes of energetic-ion-induced MHD modes have been observed in NSTX and clear evidence of energetic ion losses have been seen in conjunction with at least two forms these modes [8]. For most NSTX beam heated plasmas, TAE modes are quasi-continuous and have no detectable effect on plasma performance. However, in experiments in which H-modes with broad density profiles were created in plasmas with relatively high q on axis the TAE can become strongly bursting. Concurrently with the bursts, rapid drops (10% - 15%) in the neutron rate were observed as well as bursts of energetic-ion losses and D_α bursts. These observations suggest substantial losses of core energetic beam ions. From the burst frequency and estimated slowing down time, these modes in steady state would result in an average 40% reduction of the energetic ion population. The loss of energetic ions has also been independently confirmed by direct measurement of ion losses with a fast-ion loss probe [15, 16].

Bursting, chirping “fishbone” modes could also be seen to cause energetic ion losses at rates up to 20% per energetic ion loss per burst. This would correspond to as much as a 50% reduction in energetic ion population in steady state. These modes differ substantially from the usual precession-resonance fishbone mode seen in conventional aspect ratio tokamaks. They have been identified as bounce precession frequency

fishbone modes that are predicted to be important in high current, low shear discharges with a significant population of trapped particles having a large mean bounce angle, such as produced by near tangential beam injection into a small aspect ratio device like NSTX [18].

Although redistribution or loss of energetic ions due to bursting and kink-type MHD activity has been reported elsewhere [8,11,12,18,20] and will be discussed further in this work, the primary goal is to study redistribution or loss due to continuous EPM/TAE Alfvénic modes, a topic that heretofore has not been investigated in detail for NSTX plasmas. TRANSP [24,25] simulations using space, energy and time dependent anomalous fast ion diffusion and Motional Stark Effect (MSE)-constrained q-profiles [26] to assess fast-ion redistribution effects are reported. For reference purposes, the diagnostics used for investigation of MHD-induced energetic ion redistribution in NSTX are presented in Section 2.0. The phenomenology of ‘faux’ diagnostic signatures that can misleadingly mimic MHD-induced energetic ion redistribution effects are presented in Section 3.0. In Section 4.0, several cases representative of MHD-induced energetic ion redistribution scenarios in H-mode discharges are presented along with TRANSP code simulations of energetic ion effects using an anomalous fast ion diffusion model. In Section 5.0, measurements of the MHD-induced spatial redistribution of energetic ions obtained by horizontal and vertical scanning of the Neutral Particle Analyzer (NPA) diagnostic are presented along with TRANSP simulations of these results. Examples of contravening NSTX discharges showing null energetic ion effects in the presence of MHD activity are given in Section 6.0. ORBIT modeling that supports and extends the foregoing TRANSP analysis is presented in Section 7.0. Discussion of the reported experimental observations and numerical simulations is given in Section 8.0 and the paper concludes with a summary in Section 9.0.

2.0 Diagnostics for Investigation of MHD-induced Effects on Energetic Ions in NSTX

On NSTX, the amplitude and structure of Alfvén modes are measured using a suite of diagnostics, including Mirnov magnetic coils, Ultra Soft X-Ray (USXR), and

reflectometry diagnostics. Neutron yield data supported by Neutral Particle Analyzer (NPA) and scintillator Fast Ion Loss Probe (sFLIP) diagnostics are used to assess fast-ion redistribution or loss due to MHD-induced effects. Some characteristics of these diagnostics are discussed in this section.

The neutron production in NSTX is predominantly from beam-target reactions. Thus the neutron rate is a robust measure of the energetic ion population and serves as the primary diagnostic for identification of MHD-induced ion redistribution or loss. In the 2002-2004 run periods, a change in the response of the neutron detectors on NSTX occurred due to inexplicable changes in the detector biases. This situation was corrected [27] and all neutron rates cited in this report were derived from the fission chamber neutron detector using the legacy calibration factor of 9.0×10^{13} neutrons/volt.

The energetic ion distributions are measured using the NPA diagnostic [28]. This diagnostic utilizes a PPPL-designed EIB spectrometer [29] which measures the mass-resolved energy spectra of H and D neutrals simultaneously with a time resolution of ~ 1 ms set by signal-to-noise levels. The calibrated energy range is $E = 0.5 - 150$ keV and the energy resolution varies from $\Delta E/E = 3 - 7\%$ from high to low energy. The NPA measures Maxwellian spectra of residual H^+ to obtain ion temperatures [30] and D^+ energetic ion spectra produced by injection of neutral beams into deuterium plasma [31, 32]. As shown in Fig. 3, the NPA views across the co-injection paths of the three NBI lines on NSTX that inject at major radii $R_{NB} = 69.4$ cm (source A), $R_{NB} = 59.2$ cm (source B) and $R_{NB} = 48.7$ cm (source C) and can be scanned horizontally over a wide range of tangency radii (as well as vertically) on a shot-to-shot basis. In NSTX, by convention the neutral beam tangency radii are positive for *injection* in the co-direction. On the other hand, the convention adopted for the NPA is that positive sightline tangency radii correspond to *viewing* co-directed ions.

Spatial localization of the NPA flux arises from the intersection of the diagnostic sightline with the NBI sources as illustrated in Fig. 4a. The inset in panel(a) of this figure shows TRANSP calculation of the charge exchange emissivity for 60 keV deuterium ion energy and a sightline tangency radius of $R_{tan} = 70$ cm (blue curve) overlaid with the total beam neutral density for Source A (red curve). The curves are plotted as a function of

distance along the NPA sightline measured from the pivot point of the diagnostic (see Fig. 3). Also shown is the pitch angle variation along the sightline (black curve). As can be seen, the charge exchange emissivity is significantly localized in space due to charge exchange on the beam primary neutrals. In this case, approximately 2/3 of the integrated flux originates from the intersection of the NPA sightline with the NB region where ions are born on passing orbits. The remainder originates in the outboard regions of the plasma where ions are more likely to be deposited on trapped orbits. *(Actually, the emissivity ‘step’ in the range $R_{tan} \sim 100 - 150$ cm is an artifact that arises in TRANSP due to improper treatment of the beam halo neutrals; i.e. the halo neutrals are volume averaged both poloidally and toroidally rather than being localized around the beam footprint.)* The pitch angle ‘range’ sampled by the NPA is obtained from this plot by noting the values of the pitch angle at the rising and falling edges of the beam neutral density curve. This process was repeated for Sources B and C and for other NPA tangency radii to obtain the curves shown. The spatial localization weakens at smaller NPA tangency radii, R_{tan} , due to attenuation of the beam neutral density with increasing penetration distance. Panel(b) shows the spatial localization of the NPA measurement in terms of the major radius of the intersection of the NPA sightline with the NB axis. For vertical scanning, the maximum accessible elevation minor radius depends on the choice of horizontal tangency radius (panel (d)).

As shown in panel(c) of Fig. 4a, the localization of the NPA measurements in space and pitch angle discussed above is strongest near the NBI full energy, but remains substantial over the entire slowing down distribution. This data was obtained using a discharge with a NB notch as shown in Fig. 4b (top panel). The bottom panel shows the neutron yield (blue curve) as well as the measured (black curve) and TRANSP calculated (red curve) NPA signals around the period of the NB notch. The NB turn-off and hence the disappearance of the beam primary neutrals occurs on a sub-millisecond time scale. The response of the measured and calculated neutrals at $E_D = 70$ keV is slower, in part because both have a time resolution of $\Delta t = 2$ ms and in part because the halo neutrals decay on a longer time scale than the NB turn-off. As evidenced by the neutron yield, the beam ion energy distribution decays on a longer time scale than both the primary and halo

neutrals. Thus the abrupt decrease in the measured and calculated S_{npa} signals around the onset of the NB notch was determined for a range of energies to obtain the results shown in Fig. 4a, panel(c).

Both the volume-integrated neutron and the line-integrated NPA diagnostics show signal depletion due to fast-ion driven instabilities, but cannot distinguish between fast-ion redistribution and loss. Two recently implemented diagnostics on NSTX, the Motional Stark Effect (MSE) and scintillator Fast Lost Ion Probe (sFLIP), facilitate separation of redistribution and loss effects. In particular, sFLIP measures the pitch and energy of fast ions that are ejected from the plasma and intercept the wall-mounted probe thus discriminating fast-ion loss versus redistribution. As illustrated in Fig. 5, for certain H-mode discharges where NPA measurements of the NBI energetic ion spectra exhibit MHD-induced fast-ion depletion, the sFLIP data confirm the existence of an ion loss that occurs primarily for passing particles near the NBI full injection energy.

Diagnostics for spatial localization of MHD activity in NSTX H-mode discharges are limited. Reflectometry is ineffectual because of density cutoff and horizontal mid-plane interferometry has sparse coverage. The most effective measurement is provided by multiple USXR arrays as illustrated in Fig. 6.

3.0 “Faux” Signatures of MHD-induced Energetic Ion Redistribution

This section deals with erroneous or ‘faux’ diagnostic signatures that misleadingly imply MHD-induced energetic ion loss as evidenced by depletion of the neutron yield and NPA flux. Most frequently, faux signatures occur simultaneously with the onset of strong MHD activity making it problematic to separate their contribution from that due to the MHD-induced effects of interest. The examples discussed below represent the most robust and commonly occurring source of faux signatures, but there can be others: e.g. the location and magnitude the gas puffing used to fuel the plasma.

3.1 Outer Gap Excursions

Excursions in the width of the outer gap (Δ_{gap}) between the plasma boundary and the machine first wall structures occur frequently in NSTX discharges, sometimes by intentional programming but mostly due to transient loss of equilibrium control due to plasma events. Generally, the inner gap remains stable so a decrease in the outer gap corresponds to an increase in the plasma volume. An extreme case wherein the outer gap was programmed to change abruptly by ~ 7 cm was selected to illustrate the gap effect. As shown in Fig. 7 for SN117299, the outer gap width (panel (b), black curve) decreases during current ramp up to a relatively stable value of $\Delta_{\text{gap}} \sim 12$ cm. At $t \sim 0.2$ s, the gap is intentionally reduced to $\Delta_{\text{gap}} \sim 5$ cm in order to facilitate coupling of HHFW injection. This gap excursion resulted in a transient drop in the neutron yield (panel (b), red curve) and a sustained reduction of the NPA energetic ion flux (panel (c), black curve) that occurs in the energy range $E > E_b/2$ (panel (d)). After the transient drop, the neutron yield recovers due to rising plasma density (panel (c), red curve). As shown in Fig. 8, the measured NPA flux depletion (black curve) due to the gap excursion is also reflected in the TRANSP simulation of the NPA signal (red curve). The cause of this behavior is primarily due to a very strong increase in the prompt loss of beam ions to first wall structures as shown by the blue curve wherein beam loss increases from ~ 0.8 MW prior to the gap excursion to ~ 3.3 MW following the gap excursion. To a lesser extent, a possible contributing effect of the gap excursion is a modification the attenuation and deposition of beam injected neutrals as well as increased attenuation of the core-born charge exchange neutral efflux.

During the NB ramp up phase, an initial transient spike on the NPA signal as seen in Fig. 7(c) is a common occurrence. This spike is driven by prompt loss of NB injected energetic ions that can be caused either by injection into a low-density plasma target as is the case here or by injection during a period of rapid outer gap evolution [33] as is common during discharge initiation.

As shown in Fig. 9, strong MHD activity occurs in SN117299: (a) mode amplitude for $f = 0$ -100 kHz (black curve) and $f = 200$ -2000kHz (red curve) and Mirnov spectrograms

for (b) $f = 200\text{-}2000$ kHz and (c) $f = 0\text{-}100$ kHz with the outer gap excursion overlaid (red curve, arbitrary units). At the gap excursion, the low frequency $n = 1$ activity transitions from $f \sim 70$ kHz to $f < 20$ kHz and the mode amplitude increases sharply (panel (a), black curve) while the high frequency activity changes only modestly. This raises the following dilemma: were the evolutions of the neutron yield and NPA signals at the gap excursion driven by the concomitant change in MHD activity or by the gap excursion itself, independent of MHD effects? The latter is argued to be the case based on Fig. 8 wherein the temporal behavior of the TRANSP simulation (that contains no model for MHD effects) closely emulates the NPA measurements. Furthermore, although not shown, the measured and calculated drops in the neutron yield match closely at $\Delta S_n/S_n = 77 \pm 1$ %. Thus outer gap evolution alone can cause ‘faux’ signatures of MHD-induced energetic ion redistribution or loss.

3.2 Plasma Profile Changes

In NSTX discharges, reconnection events can trigger changes both in the type of MHD activity as well as in radial profiles of such plasma parameters as electron density, $n_e(r,t)$, electron temperature, $T_e(r,t)$, toroidal rotation velocity, $v_\phi(r,t)$ and $Z_{\text{eff}}(r,t)$. Separation of these effects is difficult as will be illustrated using SN117449 shown in Fig. 10. As seen in panel (d), early bursting EPM MHD transitions to TAE activity around $t \sim 0.2$ s at the H-mode onset and sawteeth or a reconnection events around $t \sim 0.6$ s trigger low- n , low- f kink-type activity. The reconnection event produces an abrupt drop in the neutron yield (panel (b), black curve) and a transition in the electron density evolution (panel (c), red curve). During the remainder of the discharge, the neutron yield and NPA flux (panel (c), black curve) gradually rise. Recalling that neutron production in NSTX arises mainly from beam-target interactions involving ions close to the full NB injection energy, it can be seen from the MPTS [34] contour plot in the top panel of Fig. 11 that the reconnection event leads to a collapse in the core electron density thus reducing the target density and hence the neutron production. This is to some degree offset by an increase in the core electron temperature (bottom panel) that increases energetic ion slowing down time that tends to

increase neutron production. From the CHERS [35, 36] contour plots shown in Fig. 12, it can be seen that the toroidal rotation velocity abruptly collapses (top panel). This leads to a loss in the $n_e(r,t)$ profile of the ‘density ears’ that are sustained by carbon impurities which subsequently migrate into the plasma core causing the rise in $Z_{\text{eff}}(r,t)$ seen in the lower panel. Increasing core $Z_{\text{eff}}(r,t)$ tends to depress neutron production due to depletion of the deuterium target density. These effects commingle with low-n, kink-type MHD-induced redistribution of energetic ions, a topic that will be addressed in Section 4.2 with the aid of TRANSP simulations using anomalous fast ion diffusion to emulate MHD-driven effects.

3.3 Edge Neutral Density Affects TRANSP-calculated Neutron Rates

In TRANSP, the 1-D slab-model FRANTIC code is used to calculate the transport of neutral particles into the plasma from sources surrounding the plasma. The computed neutral profile is then averaged over flux surfaces to provide a 2-D distribution. Two types of neutrals are treated: ‘cold’ neutrals associated with gas fuelling and ‘warm’ neutrals due to recycling of escaping particles. The energy and density of the source neutrals is specified as input parameters to the TRANSP code. In this work, typical values are $E_{\text{cold}} = 0.025$ eV, $E_{\text{warm}} = 20$ eV and $n_o(a) = 4.5 \times 10^{10}$ cm⁻³ for both the cold and warm neutrals. To date, the edge neutral density in NSTX has not been measured though capability to do so is scheduled for implementation in 2007. At the present time, therefore, the treatment of the edge neutral density gives rise to uncertainties in the TRANSP code modeling of the NPA efflux and a host of other computed quantities.

The magnitude of the edge neutral density, $n_o(a)$, used in TRANSP analyses can affect the calculated neutron yield. The results of a study of $n_o(a)$ effects using SN117449 discussed in the previous section are shown in Fig. 13. The top panel shows the neutron rate as a function of time for several values of the edge neutral density (red curves) along with the measured waveform (black curve). From this plot it is evident that the increasing values of the edge neutral density reduce the calculated neutron yield.

As shown in the bottom panel, the calculated neutron yield decreases in the range

$n_o(a) = 4.5 \times 10^{10} - 4.5 \times 10^{13} \text{ cm}^{-3}$ but asymptotes at lower and higher values. In addition, the reduction in calculated neutron yield with increasing $n_o(a)$ appears to be larger in the early phase of the discharge when the electron density is low. A possible explanation of this behavior follows from examination of the calculated beam power loss by charge exchange in the TRANSP analysis. It appears that below a certain density the beam power loss becomes so small that any further decrease in the neutral density has no effect. Above a certain density, the beam power loss by charge exchange becomes so large that little additional power can be lost by further increasing the edge density.

The TRANSP simulation of the NPA signal, $S_{\text{nap}}(t)$, is also affected by $n_o(a)$ as shown in Fig. 14a but in a manner that is counter intuitive. Early in the discharge when the electron density (blue curve) is low, the calculated flux is largest at the minimum $n_o(a)$ and decreases with increasing $n_o(a)$ up to $\sim 4.5 \times 10^{12} \text{ cm}^{-3}$ but saturates at higher values. This behavior of the NPA signal can be understood with the aid of Fig. 14b. Panel (a) shows typical profiles of the neutral density components as a function of distance along the NPA sightline from the pivot point that is used in the TRANSP analysis. The cold (black curve) and warm (blue curve) wall components are strongly attenuated from the user-specified edge source as they penetrate into the plasma core. The beam halo neutral component (green curve) is flat, an unphysical consequence of volume averaging in the TRANSP model as mentioned earlier. The beam primary neutral component (red curve) dominates all the others by approximately two orders of magnitude. The profile is rather broad because of the oblique trajectory of the NPA sightline through all three NB footprints that was chosen in this example (see Fig. 38 for a single source footprint). Thus the edge neutral density plays an insignificant role in the production of charge exchange neutrals measured by the NPA. The remaining curve maps distance along the NPA sightline onto normalized minor radius. Panel (b) illustrates the cause of the observation in Fig. 14a that the NPA signal decreases with increasing edge neutral density. As can be seen, the fast ion power loss increases markedly with increasing $n_o(a)$, presumably driven by fast ion orbits passing near the outboard plasma periphery where the wall neutral density component is large. Thus increasing $n_o(a)$ depletes the energetic ion population itself and hence the NPA signal. Increasing $n_o(a)$ does not elevate the NPA signal because charge

exchange production is strongly dominated by NB primary neutrals. At higher electron densities, the calculated $S_{\text{npa}}(t)$ is even less sensitive to $n_o(a)$, presumably because of screening of the neutral penetration into the plasma due to the sharp rise in the edge electron density profile characteristic of H-mode discharge.

4.0 Representative MHD-induced Energetic Ion Redistribution or Loss Scenarios in NSTX H-mode Discharges

In recent years, a rapidly expanding interest has developed in energetic ion redistribution or loss driven by Alfvén instabilities [37 – 44] and internal kink modes [45].

A rich variety of energetic deuterium ion behavior resulting from MHD activity has been observed in NSTX [11,31,32] using the neutral particle analyzer diagnostic. The appearance of MHD activity can have a pronounced effect on ‘energetic’ ($E \sim 10 - 100$ keV) ion populations in NSTX. For the purposes of this report, it is convenient to categorize the various types of MHD activity according to the scheme shown in Fig. 15. Fast, bursting modes such as fishbones, internal reconnection events (IREs) and chirping Energetic Particle Modes (EPMs) occur on times scales $\Delta t \sim 1$ ms that are short compared with evolution of plasma parameters and can drive abrupt but modest ($\Delta S_n/S_n \leq 10\%$) redistribution or loss of energetic ions. On the other hand, slow, continuous modes evolve on times scales $\Delta t \sim 100$ ms or more and include $n = 1 - 2$, $f < 10$ kHz kink-type MHD and a host of Alfvénic modes as illustrated in Fig. 2 that span a range of frequencies at $f \gg 10$ kHz. Plasma parameters also evolve on the same time scale and this often complicates analysis of significant ($\Delta S_n/S_n \sim 10\% - 70\%$) MHD-induced redistribution or loss of energetic ions [11,12]. Several examples of bursting and continuous MHD behavior are presented below.

4.1 Bursting MHD Activity

Significant fast ion losses are seen in many NSTX shots correlated with ‘bursting’ EPM and TAE modes as well as fishbone and sawtooth activity. Bursting modes that exhibit rapid downward frequency shifts (chirping) on the time scale of a few milliseconds

or less are a characteristic feature of EPM modes. The modes can chirp because the frequency is determined by the fast-ion distribution function, which can be directly modified by the modes rather than thermal plasma parameters. An example of such activity is shown in Fig. 16 where cyclic neutron rate drops of order 5 – 10% associated with the destabilization of EPMs occur. The NPA deuterium energy spectra show the strongest particle density modulation below the NBI half-energy and the density modulation of the highest energy ions is roughly 10%. As illustrated in Fig. 17, when multiple MHD modes overlap the neutron loss is somewhat larger than for single modes [46, 47]. In Fig. 17(b), for example, the initial drop in the neutron rate when the overlapping mode amplitudes are strongest is $\sim 15\%$.

While significant drops in the neutron are seen with some fishbone events, in many cases the neutron rate is virtually unaffected [18]. An example of MHD-induced loss due to sawtooth activity is shown in Fig. 18a. In contrast to EPM bursts, sawteeth can produce drops in the neutron rate exceeding 50%. Also, the associated spikes in the NPA flux (bottom panel) extend over all energies. As shown in Fig. 18b, good correlation is observed between the neutron crash and the spike in the NPA flux.

From TRANSP modeling results, large neutron-rate drops generally indicate the loss from the plasma of a substantial fraction of the energetic fast ions that are most responsible for the neutron production. Smaller neutron-rate drops could indicate either that the fast ions are just redistributed within the plasma, or that only the lower energy fast ions are expelled.

A high-speed (up to 40,500 frames/s) video camera has been used to record the energy and pitch angle distributions of neutral beam ions lost from NSTX plasmas during MHD activity, including fishbone instabilities. Non-fishbone MHD instabilities have previously been seen to augment loss of beam ions at the largest (most perpendicular) pitch angles. During fishbone bursts, however, the fast camera images reveal loss of full energy (80 keV D) ions over an extended range of pitch angles simultaneously, with no evidence that the loss is sweeping in pitch angle, including at the fastest framing rates used. The losses are often seen to vary significantly between video frames, meaning that the loss behavior is changing on a timescale of $\sim 25 \mu\text{s}$.

4.2 Continuous MHD Activity

Unlike bursting MHD activity, continuous MHD persists over 100's of milliseconds during which time plasma parameters such as n_e , Z_{eff} , and plasma equilibria usually evolve significantly. This drives changes, for example, in the neutron rate, NPA measurements and sometimes even the nature of the MHD activity itself. The depletion of the NPA signal is a combination of two effects: 1) changes in the charge exchange emissivity driven primarily by the n_e evolution and 2) the MHD-induced redistribution or loss of energetic ions. The TRANSP simulation of the NPA diagnostic is used to correct for the emissivity component leaving a 'residual' depletion attributed to MHD effects.

In Fig. 19, the NPA energetic ion spectrum for the selected discharge SN117449 shows significant flux depletion above $E_b/2$ (encircled region) where $E_b = 90$ keV is the NBI energy. A smaller depletion occurs around $E_b/3$. Onset of the depletion correlates with onset of strong TAE activity at $t \sim 0.2$ s.

The waveforms for this discharge shown earlier in Fig. 10 are I_p and total NBI power (panel (a)), neutron rate and core safety factor (panel (b)), NPA signal at $E_d = 60$ keV and electron line density (panel (c)), and finally the Mirnov MHD spectrogram (panel (d)). Depletion of the NPA signal commences at $t \sim 0.2$ s concurrent with onset of TAE activity and continues through bursting EPM activity at $t \sim 0.5 - 0.6$ s. A transition to $n = 1$, $f \sim 10$ kHz kink-type MHD occurs beyond $t \sim 0.6$ s. A modest recovery of the NPA signal occurs during this period because a drop in n_e slightly relaxes the emissivity contribution to the signal depletion.

In TRANSP, an Anomalous Fast Ion Diffusion (AFID) model can be applied to simulate MHD-induced redistribution or loss of NBI slowing down ions. In this model the diffusivity can be specified as a function of time and space in the discharge corresponding to localization of the MHD activity as shown in the upper panel of Fig. 20 as well as over a specified ion energy range to accommodate the energy-selective loss observed in the NPA measurements as shown in the lower panel. The choice of the AFID spatial dependence is supported by USXR measurements of the mode location as shown in Fig. 21 where the

USXR emission peaks in the region of the Shafranov-shifted plasma major radius, $R_{\text{maj}} \sim 110$ cm. Two criteria were employed for determining the fast ion diffusion parameters. The first was to match the TRANSP-calculated and measured neutron rates. The second was to simultaneously obtain agreement between the TRANSP-simulated and measured NPA signal evolution and energetic ion distributions.

Note that energetic ion diffusion in ‘MHD-quiescent’ discharges is generally small in conventional tokamaks [48] and there is no evidence so far that this is not the case in spherical tokamaks as well. So the use of enhanced energetic ion diffusion to emulate the observed MHD ion loss must not be construed as implying that elevated energetic ion diffusion is a feature unique to spherical tokamaks.

The TRANSP analysis results are shown in Fig. 22 for the neutron rate (top panel) and NPA signal (bottom panel). Without AFID the TRANSP calculations are well above measurements. However, the calculations with AFID agree reasonably well with measurements, particularly during the time of interest from $t = 0.6 - 1.0$ s. Simultaneously, good agreement between measured and simulated NPA energetic ion spectra is obtained as shown in Fig. 23.

The effect of MHD-induced energetic ion redistribution on plasma current density profiles is assessed by comparing measured and calculated current profiles as shown in Fig. 24. An equilibrium code is used to compute the inductive (orange) and bootstrap (red) current profile components as described in [12]. The NBICD component (blue) from TRANSP calculation and the summation of the aforementioned components yields the calculated total (black) toroidal current profile. The measured current profile (gray) is derived from an MSE-constrained reconstruction that uses the CHERS radial electric field profile from carbon impurity force balance to correct the MSE [47] pitch angle data.

In Fig. 24(a), it can be seen that the calculated total current density exceeds the MSE-reconstruction value by $\sim 25\%$ in the core region. However, as shown in Fig. 24(b), the TRANSP-calculated redistribution of fast ions using the AFID model reduces the NBICD component and hence the calculated total current density in the core to essentially the same value as the MSE reconstruction.

Thus far in the analysis of SN117449 it has been implicitly assumed that energetic ion redistribution or loss was driven by low frequency MHD activity (i.e. $f < 100$ kHz). As shown in Fig. 25, however, persistent high frequency ($f = 200 - 2000$ kHz, panel (b)) and low frequency ($f = 0 - 100$ kHz, panel (c)) MHD activities coexist albeit with high frequency mode amplitudes approximately which are two orders of magnitude below that for low frequency (panel (a)). Opportunity exists to validate this assumption as illustrated by the waveforms for SN120001 in Fig. 26 that are very similar to SN117449 with the exception that low frequency activity becomes 'quiescent' beyond $t \sim 0.6$ s. The criterion for 'quiescent' is that the low frequency mode amplitude, δB , according to the Mirnov spectrogram is reduced by an order of magnitude or more. Since MHD-driven diffusion of energetic ions scales as $(\delta B/B)^2$, redistribution should be reduced by a factor of $\sim 10^{-2}$ or more. Thus the period $t \sim 0.6 - 1.0$ s provides a window to investigate the effect of $f > 200$ kHz activity during a quiescent period of $f < 100$ kHz activity. For SN120001, panel (c) of Fig. 26 shows that during the EPM/TAE phase starting at $t \sim 0.2$ s, the mode amplitude for the $f < 100$ kHz activity was $(\delta B)_{\text{rms}} \sim 0.3$ Gauss but decreases an order of magnitude by $t \sim 0.6$ s. The mode amplitude for $f > 200$ kHz is $(\delta B)_{\text{rms}} \sim 1.5 \pm 0.5 \times 10^{-3}$ Gauss throughout the discharge. These values are reasonably equivalent to those for SN117449 as shown in Fig. 25(a).

The TRANSP analysis for SN120001 is shown in Fig. 27. In panel (b), it can be seen that a modest mismatch between the measured (black curve) and TRANSP-calculated (blue curve) neutron yields exists only for $t < 0.6$ s. Application of anomalous fast ion diffusion shown in panel (a) corrects this mismatch as shown by the red curve in panel (b) while at the same time providing a reasonable match between the measured and TRANSP-simulated NPA signal evolution at $E_d = 70$ keV as shown in panel (c). The conclusion to be drawn from this exercise is that MHD-induced energetic ion redistribution or loss effects appear to be notable only at $t < 0.6$ s during EPM/TAE activity. The high frequency activity alone at $t > 0.6$ s appears to have no effect on the energetic ion redistribution or loss. However, this statement must be qualified by the fact that modest

redistribution can be masked by a flat core electron density profile. Confirmation of this conjecture is the topic of a NPA vertical scan discussed in the following section.

5.0 NPA Horizontal and Vertical Scanning Measurements of Energetic Ion Redistribution or Loss

In quiescent or MHD benign NSTX discharges, NPA measurements of the energetic beam ion distribution are consistent with classical behavior [49]. As discussed in Section 4.2, the appearance of strong, continuous MHD activity can have significant effects on energetic ($E \sim 10 - 100$ keV) ion populations in NSTX; namely, after H-mode onset, the NPA charge exchange spectrum usually exhibits a significant loss of energetic ions only for $E > E_b/2$ where E_b is the beam injection energy, though in some cases the loss was observed to extend down to $E_b/3$.

A horizontal NPA scan was performed for the discharge parameters shown in Fig. 28 for SN115789. This discharge was similar in most respects to SN117449 shown in Figs. 10 and 25. Neutral beams were injected using sources A and B at 90 keV with total power $P_{NB} = 4$ MW (panel (a)). H-mode onset occurred shortly after $t \sim 0.2$ s attended by strong, continuous MHD activity (panels (c) and (d)), rollover of the neutron yield (panel (b)) and depletion of the NPA energetic ion spectrum down to $E_b/3$ (panel (e)).

NPA horizontal scan spectra are shown in Fig. 29 at $t = 180$ ms prior to spectrum depletion (top panel) and at $t = 500$ ms during depletion (bottom panel). For NPA tangency radii below $R_{tan} \sim 70$ cm, it can be seen that the $t = 500$ ms spectrum exhibits depletion (encircled region) extending down to $E_b/3$ relative to the $t = 180$ ms spectrum. A quantitative measure of the depletion was obtained by comparing the magnitude of the NPA fluxes at $E = 60$ keV for each tenable tangency radius as shown in Fig. 30. The data for the scan shown in Fig. 29 (black points) have been augmented by other horizontal scans (red points). The blue curve maps the NPA tangency radius to the major radius corresponding to spatial localization of the NPA measurements. As shown by the grey shaded area, the maximum NPA flux depletion is $\sim 70\%$ and occurs at $R_{tan} \sim 50 \pm 20$ cm corresponding to $R_{maj} \sim 75 \pm 10$ cm. From the upper left panel in Fig. 4a, the region of

maximum energetic ion depletion is associated primarily with passing ions. Herein a quandary arises: namely, the maximum depletion region is modestly inboard of the NSTX vessel major radius of $R_{\text{depletion}} = 85$ cm and significantly inboard of the Shafranov-shifted plasma radius of $R_{\text{Shafranov}} \sim 110$ cm. A plausible explanation can be proffered based on the topology of energetic ion passing orbits. NB deposition peaks around the Shafranov-shifted plasma radius, this being the region of peak electron density. However, because of the large ion orbits ($\Delta R \sim 30$ cm) the NPA signal is localized to the intersection of the inboard leg of the orbit with the primary beam neutral population that corresponds to $(R_{\text{Shafranov}} - \Delta R) \sim 80$ cm $\sim R_{\text{depletion}}$. From the discussion appearing in Section 7.0, for $R_{\text{tan}} \sim 50 \pm 20$ cm it would appear that the region of intersection of the NPA sightline with the NB is in the energetic ion loss region. If this were the case, the flux depletion shown in Fig. 30 should reach 100%. However, it was pointed out in Section 2.0 that while the NPA flux is significantly localized to the NB intersection there is still a contribution to the NPA signal of order 30% that originates outside this region due to charge exchange on ‘background’ neutrals originating, for instance, from wall sources. For this reason, one would not expect the measured depletion to reach 100%.

More direct (i.e. with minimal variation in pitch angle compared with a horizontal scan) information on MHD-induced radial redistribution of energetic ions should be possible using the NPA vertical scanning capability as shown by the TRANSP simulation of a vertical scan shown in Fig. 31. The top panel shows vertical energetic ion profile is core-peaked during the MHD-quiescent phase (i.e. without anomalous fast ion diffusion). During the MHD-active phase (i.e. with anomalous fast ion diffusion), the bottom panel shows a depletion of the ion distribution (encircled) in the core region above $\sim E/2$ and displacement of these ions outward to the region $r/a \sim 0.2 - 0.4$. The energetic ion flux radial profile thus becomes hollow in the core region and develops an outboard shoulder.

A NPA vertical scan was performed (under conditions similar to SN117449: see Fig 10 and 25) as shown by the discharge characteristics in Fig. 32. Preliminary results are shown in Fig. 33 where the vertical minor radius axis is the distance along a vertical line centered at the intersection of the NPA sightline with the NB footprint (see Figs. 3 and 4a).

The measurements in the top panel corresponding to a MHD-quiescent period show a monotonically decreasing energetic ion distribution from the core outwards. By contrast, during strong MHD activity the energetic ion distribution in the core region is depleted and these core ions are redistributed radially outwards to form a shoulder on the measured distribution as evident in the bottom panel.

Fig. 34 shows a vertical scan taken during NBI into a gas filled torus with toroidal magnetic fields only in the range $B_T = 3.5 - 4.5$ kG and with Source A only at $E_b = 90$ keV that were run for the purpose of MSE calibration. The abrupt drop in flux occurs at $R_{\text{Minor}} \sim 25$ cm when the NPA sightline passes beyond the footprint of the beam primary neutrals. The NPA spatial resolution is ~ 2.5 cm. This agrees reasonably with the footprint expected from the geometry of the NB ion source that has a height of 40 cm centered on the NSTX mid-plane and provides an independent calibration of the vertical scan radius. The NPA-measured NBI particle fractions derived from the data in Fig. 34 are $E_b/3:E_b/2:E_b = 0.42:0.42:0.16$ which compares favorably with the calibrated NBI values of $E_b/3:E_b/2:E_b = 0.44:0.39:0.17$ for 100keV extraction energy. Further data validation as well as TRANSP analysis is deferred to a future report.

6.0 Contravening NSTX Discharges with Null Depletion of the NPA Efflux in the Presence of Robust MHD Activity

In some NSTX discharges, the measured NPA efflux does not exhibit any depletion in spite of the presence of robust MHD activity. In Table I, SN117449 with strong depletion of the NPA signal as shown in Fig. 10 and discussed in Section 4.2 is compared with SN117126 that shows depletion. Comparison of the global discharge parameters for the two cases shows the absence of any significant differences.

Selected discharge characteristics for SN117126 are presented in Fig. 35. As the NBI power (panel (a)) approached $P_{\text{NB}} = 6$ MW at $t \sim 0.2$ s, H-mode onset occurred simultaneously with growth of strong TAE activity at $f < 100$ kHz (panels (c) and (d)) followed around $t \sim 0.7$ s by a transition to low frequency, kink-type MHD similar to SN117449. Like SN117449, the TRANSP-calculated neutron rate exceeded the

measurement by $\sim 25\%$ after transition to the kink-type MHD (panel (b)). Unlike SN117449, however, the measured NPA spectrum showed virtually no depletion (panel (e)). (The brief divot at $t \sim 0.7$ s is due to an outer gap excursion.) Such “no-depletion” shots are atypical but have been observed over several years of NSTX operation. In all cases, adjoining discharges showed the typical depletion characteristics thus eliminating the cause as being due to some aberration in the operation of the NPA diagnostic.

Further comparison of the two discharges is given in Fig. 36. Referring to the top panel, the initial peak observed in both the measured (black) and TRANSP-simulated (red) NPA signals is caused by ramp up of NB injection from $t = 0.08 - 0.20$ s. The outer gap width (blue) increased from $\Delta_{\text{gap}} = 9$ cm to $\Delta_{\text{gap}} = 16$ cm from $t = 0.20 - 0.28$ s causing the subsequent abrupt rise in the measured NPA signal. However, the TRANSP simulation uncharacteristically did not reflect this feature, unlike the case for SN117299 shown in Fig. 8. For the remainder of the discharge, the measured NPA signal remained relatively flat

TABLE I

Comparison of Discharges With and Without NPA Efflux Depletion

Parameter	SN117449	SN117126
Energetic Ion Loss	Yes	No
I_p (MA)	0.9	0.9
B_T (kG)	4.5	4.5
P_b (MW)	6	6
E_p (keV)	A,B@90:C@80	A,B,C@90
n_e ($\times 10^{13}$ cm $^{-3}$) - peak	4	6
Z_{eff}	1.5	3.0
V_ϕ collapse	@ $t = 0.6$ s	@ $t = 0.6$ s
S_n ($\times 10^{14}$ s $^{-1}$) - measured	2.0	2.2
S_n ($\times 10^{14}$ s $^{-1}$) - TRANSP	2.5	2.8
Δ_{gap} (cm)	14 ± 2	15
H-mode dropout	@ $t = 0.6$ s	@ $t = 0.7$ s
MHD mode location	Core	Core
Similarity Interval (s)	$t = 0.25 - 0.6$	$t = 0.25 - 0.6$
TRANSP Run	117449M22	117126A01

Additional no S_{npa} depletion cases: 116049A02, 116278M01, 117138M01, 117424M01, 122684M01

exhibiting absence of the depletion that is typically seen while the simulated signal showed the normally expected depletion behavior. Also, unlike SN117449 presented in Fig. 19 the spectrum showed no MHD-induced energetic ion depletion.

In the interval $t = 0.60 - 0.75$ s, the outer gap decreased from $\Delta_{\text{gap}} = 16$ cm to $\Delta_{\text{gap}} = 11$ cm driving a strong divot in the NPA signal amplitude. From the bottom panel, the above NPA signal divot occurred for $E > E_b/2$ but not lower energies. However, the simulated signal showed no response contrary to the behavior seen for SN117299 in Fig. 8. This reason for this is that the minimum gap in SN117126 was $\Delta_{\text{gap}} = 11$ cm compared with $\Delta_{\text{gap}} = 5$ cm. As a result, the TRANSP-calculated prompt ion loss at the gap excursion for SN117126 was very small: namely $P_{\text{loss}} \sim 0.2$ MW compared with $P_{\text{loss}} \sim 3.3$ MW for SN117299. Since there was minimal prompt-loss-driven depletion of the energetic ion population, the TRANSP-simulated NPA efflux showed little change. Unfortunately, this leaves the strong divot observed in the measured efflux without explanation.

The absolute NPA signal level at $E > E_b/2$ for SN117126 was $S_{\text{npa}}(t) \sim 2-3 \times 10^5$ cps which was the same for SN117449 at $t \sim 0.2$ s prior to the onset of depletion. The NPA signal is not saturated since this count rate is well below credible signals up to 5×10^5 cps that have been observed for other discharges. This confirms that the NPA operating conditions were stable and thus not the cause of the different behavior between the two shots.

As of this writing, the differences between the neutron and NPA behaviors in the two shots cannot be explained. Based on the global discharge characteristics, they should be very similar. Of course, the question can be raised as to whether or not a ‘hidden parameter’ has been overlooked. This aside, the measured and TRANSP-simulated NPA time evolutions are in remarkable disagreement. The example given in this section is an extreme one but by no means isolated as indicated by the additional ‘no depletion’ cases noted in the footer of Table I. Furthermore, this ‘additional’ list is not exhaustive but representative of such behavior being observed over an extended period of NSTX operation.

7.0 ORBIT Code Analysis

The energetic ion signal for charge exchange neutral particle diagnostics consists of a complex line-integrated measurement along a manifold through a multi-dimensional space consisting of physical coordinates, energy and pitch angle. For ‘passive’ measurements the source of neutrals for charge exchange reactions is a gas mantle surrounding the plasma whose density attenuates strongly with distance into the plasma. For effectiveness, neutral beam and other sources of auxiliary heating are configured so that the energetic ion distribution peaks in the plasma core region in order for the particles to be confined. The energy resolution and the trajectory of the NPA sightline through the plasma define other dimensionalities such as pitch angle. As a result, for passive NPA measurements the manifold through this multi-dimensional space is very broad. On the other hand, for ‘active’ NPA diagnostics using either heating neutral beams or a dedicated diagnostic NB, this manifold becomes significantly narrower. In the case of NSTX, the line-integrated NPA measurement actually becomes strongly localized in both space and pitch angle to a region defined by the intersection of the diagnostic sightline with the footprint of the beam neutrals as discussed earlier in Fig. 4a. Even so, the ‘thickness’ of this reduced manifold varies with the trajectory of the NPA sightline through the plasma. For example, it can be seen from the upper left panel in Fig. 4a that for a horizontal tangency radius, R_{tan} , near zero the spread in pitch angle is negligible. With increasing R_{tan} the width in pitch angle (i.e. the separation between the solid and dashed lines of a given color) grows but then decreases again for sufficiently large R_{tan} where the NPA sightline becomes increasingly tangential to flux surfaces.

ORBIT[50,51] code modeling can provide valuable insight into several characteristics of the NPA measurements of energetic ion distributions in NSTX. The ORBIT code, which can handle highly non-circular geometries as well as non-axisymmetric magnetic perturbations, follows beam ion guiding center orbits and calculates the effect that MHD modes have on the energetic ion distribution. Fig. 37 gives selected confined guiding center passing particle orbits (solid lines) for $E = 65$ keV deuterium ions calculated with the ORBIT code using a magnetic equilibrium derived at $t =$

700 ms from SN117449, a case representative of all discharges discussed in this report. The orbits correspond to values of R_{maj} and v_{\parallel}/v derived from Fig. 4a for representative NPA tangency radii used in the horizontal scan results shown in Fig. 29 and Fig. 30. The dashed line shows the lost particle orbit just inside of the confinement boundary for passing particles. Note that the presented ORBIT calculations do not include finite Larmor radius effects, which may change the confinement region. The electric field due to toroidal plasma rotation was included in the calculation, but had a negligible effect on the passing particle orbits. Overlaid in blue is a scaled facsimile of the beam neutral footprint shown in Fig. 38 (to be discussed momentarily) that is positioned at a major radius corresponding to the intersection of the NPA sightline with the NB for a horizontal tangency radius of $R_{\text{tan}} = 70$ cm. During a horizontal scan such as shown in Fig. 29, this NB footprint would move in major radius from the plasma periphery region (when the NPA $R_{\text{tan}}=125$ cm) to minimum (when the NPA $R_{\text{tan}}=0$ cm) that corresponds closely to the NB tangency radius.

The orbit plot confirms the explanation given in Sec. 5.0 regarding interpretation of the peak in the NPA flux depletion shown in Fig. 30. Recall that at first glance it appeared odd that the measured peak depletion should occur at a major radius of $R_{\text{maj}} \sim 75 \pm 10$ cm, well inside the Shafranov-shifted magnetic axis at $R_{\text{maj}} \sim 110$ cm. As is clearly demonstrated in Fig. 37, this occurs because the source of the measured flux is localized by the NB footprint to the inner leg of the passing orbits: i.e. well inboard of the Shafranov-shifted magnetic axis. The outward radial diffusion of energetic ions that is driven by core-localized MHD activity ‘drags’ the displaced ion orbits away from the NB footprint thus leading to depletion of the NPA flux. It is also worth noting that for a range of NPA R_{tan} the energetic neutral efflux must ‘tunnel’ through the bulk of the electron density profile whose peak is located at the Shafranov-shifted magnetic axis. This makes straightforward attenuation of the efflux a very significant contributor to the observed depletion of the NPA signal, a contribution that must be accounted for by TRANSP simulations.

Figure 38 shows the beam neutral footprint for Source A in a poloidal plane passing through the NB tangency radius of $R_{\text{NB}} = 69.4$ cm that was calculated using a stand-alone neutral beam calibration code [52]. The full NSTX NB geometry is used to compute the footprint that includes the full, one-half and one-third energy primary beam neutrals. Beam

halo neutrals, however, are not included. The halo neutrals enlarge the overall neutral footprint in all directions by a significant amount, perhaps 25%, albeit with a density of order one-half that of the primary neutrals. Thus the vertical half-height of the NB footprint extends to ~ 40 cm which is consistent with the energetic ion profiles shown in Fig. 33 and Fig. 34 that were obtained by NPA vertical scanning.

Figure 39 is a contour plot of the neutral beam distribution function at $E = 65$ keV as a function of major radius and pitch, $v_{||}/v$ taken at the low field side in the midplane outside of the magnetic axis. The contours correspond to equally spaced values of the beam ion distribution function. The red circles correspond to the three confined orbits shown in Fig. 37. Since the variation of $v_{||}/v$ is modest on an orbit trajectory of passing ions, it is clear (in conjunction with Fig. 37) that the NPA measures passing particles only for the sightline tangency radii used in the ORBIT analysis. It is also noteworthy that the measured passing ions are expected to interact with TAE modes much stronger than the trapped ions.

8.0 Discussion

In NSTX discharges since at least 2002 to the present, it is commonplace in discharges with robust MHD activity for the TRANSP-calculated neutron rates to exceed the neutron measurements [27]. In L-mode discharges, the calculated excess is modest with $(S_{n,TRANSP} - S_{n,Measured}) / S_{n,Measured} \sim 10 \pm 5\%$. This is within the 25% uncertainty in the calibration of the fission chamber detector. However, in H-mode discharges the excess can be large with $(S_{n,TRANSP} - S_{n,Measured}) / S_{n,Measured} \sim 50 \pm 20\%$. The cause of this excess has not been convincingly identified (e.g. unknown errors in the measured input quantities to TRANSP or in the code itself) and in this work the excess is attributed to MHD-induced energetic ion redistribution or loss. A similar situation has been reported for JET [53] where $(S_{n,TRANSP} - S_{n,Measured}) / S_{n,Measured} \sim 60 \pm 20\%$ for all types of discharges including H-mode, hybrid scenarios, high β_N and plasmas with ITBs likewise without causal identification. Similar discrepancies have been observed on DIII-D [13] using TRANSP. On the other hand, good agreement between the measured neutron emission rate and calculated values for high β_p H-mode plasmas in JT-60U using the TOPICS code has been

reported [54]. Likewise on MAST, the LOCUST 3D Monte Carlo full Larmor orbit code (in which, by the way, the halo neutrals are treated correctly) yields good agreement between not only calculated and measured neutron rates [22] but also simulated and measured NPA efflux [23].

TRANSP is a 1-1/2 D axisymmetric Monte Carlo code that uses a ‘modified-Larmor-orbit’ treatment as opposed to a ‘full-Larmor-orbit’ calculation. In one mode, the ion Larmor orbit is periodically updated based on the magnetic field at the guiding center of the particle. In a second mode, the periodic update uses the magnetic field at the physical location of the particle itself (which requires increased CPU time). Both modes yield the same calculated neutron rate within the Monte Carlo statistics (e.g. 120668M01 – guiding center and 120668M02 – particle center).

Application of the AFID model in TRANSP to create an acceptable match between the measured and calculated neutron rates as well as the NPA effluxes involves selection of multiple parameters: namely, the space, time and energy dependence of the magnitude of the anomalous fast ion diffusion to be applied. In most cases, multiple combinations of these parameters can achieve similar results: i.e. no unique AFID model exists. Nevertheless, certain forms of the AFID model frequently provide better signal matching than others. For example, spatial dependence that are flat in minor radius or are weighted to $0.5 < r/a < 1.0$ seldom work well. The best results are usually obtained with a core-weighted dependence where the diffusion in the region $0 < r/a < 0.2$ is several time larger than that in the region $0.2 < r/a < 0.4$. The region $0 < r/a < 0.2$ alone is least ineffective and requires order of magnitude larger diffusion values than needed when combined with the region $0.2 < r/a < 0.4$. Thus an extended but core-weighted AFID spatial model works best as illustrated in Fig. 27c. Fortunately, this is consistent with the fact that: 1) the NB fast ion deposition is core-weighted, 2) many of the MHD modes of interest are core-weighted as supported both by theory as well as by spatial measurements of mode amplitude using, for example, USXR and reflectometry, and 3) the NPA measurements are core-weighted to the intersection of the diagnostic sightline with the NB axis. Specification of the energy dependence is likewise not unique. For example, the extended energy dependence shown in the bottom panel of Fig. 20 generally produces an acceptable

match between the measured and calculated energy distributions of the fast ions. However, a model having relatively narrow 'square-waves' centered around the full and half energy NB components often works as well. This is not surprising since reduction of the NB source energy components removes them from contributing to the energetic ion slowing down distribution. In short, while its specification is not unique the AFID model in TRANSP works best when constrained by available information on the MHD mode characteristics.

The sensitivity of the AFID modeling in TRANSP to variations in the edge neutral parameters discussed in Section 3.3 is not examined in this report. In an independent work [23], the parameters that might affect the radial profile of the background neutral density in the TRANSP code (edge temperature and density, neutral influx velocity, recycling ration, etc) were varied within realistic upper and lower limits for discharge conditions on the MAST experiment. The TRANSP-simulated NPA energy spectra for MAST were very insensitive to the variation in all parameters except for the edge neutral density and it is reasonable to expect the same result for NSTX. On MAST, the edge neutral density is experimentally measured using a linear D_α camera. Such measurements have not been available on NSTX to date though capability is expected in the near future using a 2-D CCD camera with a D_β filter to image the outboard edge of the plasma which combined with Abel inversion and a collisional-radiative model using MPTS-measured electron density and temperature will yield an absolute neutral density radial profile [55]. Therefore, it was deemed appropriate to await NSTX edge neutral measurement capability in order to define a realistic range of variation for examining the sensitivity of AFID modeling to this parameter.

Simulation of the NPA signal using TRANSP is compromised by inadequate treatment of the beam halo neutrals. When a primary beam neutral is deposited via charge exchange on a thermal ion, the thermal ion in turn becomes a neutral known as a halo neutral. As the term implies, halo neutrals remain relatively localized around the footprint of the beam primary neutrals. However, in the TRANSP code these halo neutrals are volume averaged both poloidally and toroidally. Since the densities of the primary and halo neutrals can be comparable, this situation can significantly affect the TRANSP

calculation of the NPA charge exchange production that is localized to the intersection of the NPA sightline with the NB primary and halo footprint.

In many NSTX discharges, the electron density evolves strongly during the first half of the discharge and then flattops or evolves slowly thereafter. During the ‘flattop’ period, the halo neutral effect can be removed by appropriate normalization of the measured and TRANSP-calculated quantities as was done previously in [11,12]. The dominant MHD activity during this period is typically kink-type modes. In this report, however, interest is focused on continuous EPM/TAE Alfvénic Eigenmodes that tend to be dominant during the first half of discharges when the electron density (and presumably the halo neutral density) are evolving significantly with time. Therefore, using the TRANSP simulation of the NPA efflux to correct the measured efflux leaving a residual signal that can be ascribed to MHD-induced redistribution effects is a questionable process. As long as the effect of the computational treatment of the halo neutrals in TRANSP remains in doubt, closure of the primary goal of this study cannot be made.

If this compromised treatment of halo neutrals affects only the amplitude of the charge exchange flux, the analysis of MHD-induced redistribution or loss effects presented in this report would not be significantly affected since the calculated and measured fluxes could be normalized. However, the primary and halo neutrals are expected to have different spatial and temporal characteristics: for example, the primary neutral population decreases with penetration distance into the plasma whereas the halo population increases and these processes vary in time with the evolution of the electron density. In an attempt to resolve this dilemma, the effect of halo neutrals on the NPA signals is being investigated using the LOCUST code developed by R. Akers at MAST. The 3D Monte Carlo LOCUST code properly preserves the halo neutral density around the footprint of the beam primary neutrals.

9.0 Summary

In summary, MHD activity such as bursting or continuous Alfvén eigenmodes or internal kink-type modes can reduce the measured neutron rate and NPA efflux as well as

induce NBICD profile redistribution. During data mining, care must be taken to identify 'faux' diagnostic signatures due, for example, to outer gap excursions and abrupt plasma profiles changes that misleadingly mimic MHD-induced effects. In particular, abrupt changes in n_e , Z_{eff} and v_ϕ are often concurrent with internal reconnection events that simultaneously trigger substantial variation in the nature of the MHD activity. Horizontal and vertical NPA scans were obtained that demonstrate MHD-induced redistribution of the NB energetic ion population. TRANSP analysis using anomalous fast in diffusion can model these MHD-induced energetic ion redistribution effects to yield agreement between the calculated and measured quantities provided steady-state plasma conditions exist. Inexplicable contravening discharges exist wherein significant depletion of the NPA measurements is absent in spite of the presence of multiple types of robust MHD activity, raising the specter that perhaps some "hidden" parameter has been overlooked. Closure on continuous EPM/TAE-induced redistribution or loss of energetic ions, the primary goal of this work, that arises primarily in non-steady-state plasma conditions awaits either an upgrade of the treatment of halo neutrals in TRANSP or an independent demonstration that the halo neutral issue is irrelevant.

Appendix

For completeness in this work, a brief overview is given of the classical characteristic slowing down and 90° pitch angle scattering times based on Coulomb collision theory [A1]. For the present purposes, a deuterium beam ion with mass A_b , charge Z_b , and full energy E_{b0} is considered. As introduced by Stix [A2], the time for such an energetic ion to thermalize is given by

$$\tau_{th} = \frac{\tau_{se}}{3} \ln \left[1 + (E_{b0} / E_{crit})^{3/2} \right] \quad (1)$$

where, τ_{se} , the slowing-down time on electrons first defined by Spitzer [A3] is

$$\tau_{se} = 6.27 \times 10^{14} \frac{A_b T_e^{3/2}}{Z_b^2 n_e \ln \Lambda_e}. \quad (2)$$

E_{crit} , the critical energy at which ions and electrons receive a equal energy transfer from the beam ions, is given by

$$E_{crit} = 14.8 A_b T_e \left(\frac{[Z_i]}{A_i} \right)^{2/3} \quad (3)$$

where the average charge to mass ratio of the bulk ions (denoted by the subscript 'i') is

$$\frac{[Z_i]}{A_i} = \frac{\sum_i n_i (Z_i^2 / A_i) \ln \Lambda_i}{n_e \ln \Lambda_e}. \quad (4)$$

The time for 90° pitch angle scattering [A4,A5], τ_{scat} , for full energy deuterium ions can be expressed as

$$\tau_{scat} = 1.11 \times 10^{13} \frac{A_b^{1/2} E_{bo}^{3/2}}{Z_b^2 Z_{eff} n_e \ln \Lambda} \quad (5)$$

where

$$Z_{eff} = \frac{1}{n_e \ln \Lambda} \sum_j n_j Z_j^2 \ln \Lambda_j \quad (6)$$

and the subscript 'j' indexes the bulk and impurity ion species. Units in the above expressions are time(s), energy(eV), mass(AMU), T_e (eV) and n_e (m^{-3}).

Competition between ion energy diffusion and electron drag can give rise to a slope [A6 and references therein] of the ion energy distribution above the neutral beam injection energy of the form $f(E) \sim \exp(-E/T_{eff})$, where T_{eff} given by

$$T_{eff} = \frac{T_i + (E/E_{crit})^{3/2} T_e}{1 + (E/E_{crit})^{3/2} \pm \tau_{se} 9.58 \times 10^{11} \frac{Z_b}{A_b} \frac{|\vec{E}^*|}{v_b} (E/E_{crit})^{3/2}} \quad (7)$$

is an effective temperature that is a weighted average of the ion and electron temperatures. The last term in the denominator that accounts for the effect of the toroidal electric field, $|\vec{E}^*|$, is $O \sim 10^{-2}$ compared with unity in NSTX and can be neglected. Thus for $E_{crit} \sim 15$ KeV, $E = 80$ keV and $T_i \sim 2T_e \sim 1$ keV typical of neutral beam heated discharges, $T_{eff} \sim T_i/2 \sim 0.5$ keV. Hence, the slope of the neutral beam distribution above the injection energy is small and, in fact, below the NPA energy resolution mentioned earlier.

The neutron yield, S_n , is given by

$$S_n \propto n_d N_f \propto n_d P_{NB} \tau_{se} \propto \frac{n_d}{n_e} P_{NB} f(T_e) \quad (8)$$

where the energetic ion distribution function, $f(T_e)$, can be a function of multiple additional parameters depending beam injection and plasma discharge conditions.

Acknowledgements

This work was supported by U.S. DOE Contract DE-AC02-76CH03073 and Grant DE-FG02-99ER54523 (JHU).

References

- [1] M. Ono, *et al.*, “Overview of the Initial NSTX Experimental Results,” Nucl. Fusion **41** (2001) 1435
- [2] Y.-K. M. Peng and D. J. Strickler, Nucl. Fusion **26** (1986) 769
- [3] J. E. Menard, *et al.*, “ β -Limiting MHD Instabilities in Improved-performance NSTX Spherical Torus Plasmas,” Nucl. Fusion **43** (2003) 330
- [4] J. E. Menard, *et al.*, “Overview of Recent Physics Results from the National Spherical Torus Experiment (NSTX),” 21st IAEA Fusion Energy Conference, 16 – 21 October, Chengdu, China, CD-ROM OV/2-4. Also Princeton Plasma Physics Laboratory Report, PPPL-4211 (2007). (Submitted to Nucl. Fusion)
- [5] D. A. Gates, *et al.*, “Progress Towards Steady State on NSTX,” Nucl. Fusion **46** (2006) S22 - S28
- [6] S. M. Kaye, *et al.*, “Progress Towards High Performance Plasmas in the National Spherical Torus Experiment (NSTX).” Nucl. Fusion **45** (2005) S168 – S180
- [7] C. Z. Cheng and M. S. Chance, Phys. Fluids **29**, (1986) 2471
- [8] E. D. Fredrickson, N. N. Gorelenkov, D. Darrow, *et al.*, “Wave Driven Fast Ion Loss in the National Spherical Torus Experiment,” Phys. of Plasmas **10** (2003) 2852
- [9] H. L. Berk, B. N. Breizman, J. Candy, *et al.*, “Spontaneous Hole-clump Pair Creation,” Phys. Plasmas **6**, (1996) 3102
- [10] E. D. Fredrickson, *et al.*, “Scaling of Kinetic Instability Induced Fast Ion Losses in NSTX,” 20th IAEA Fusion Energy Conference, Vilamoura, Portugal, 1-6 November 2004 (IAEA, Vienna) CD-ROM EX/5-3. Also Princeton Plasma Physics Laboratory Report, PPPL-4084 (2005).
- [11] S. S. Medley, *et al.*, “MHD-Induced Energetic Ion Loss during H-mode Discharge in the National Spherical Torus Experiment,” Nucl. Fusion **44**, (2004) 1158
- [12] J. E. Menard, *et al.*, “Observation of Instability-Induced Current Redistribution in a Spherical Torus Plasma,” Phys. Rev. Lett. **97**, (2006) 095022
- [13] W. W. Heidbrink, N. N. Gorelenkov, M. Murakami, “Beam-Driven Energetic Particle Modes in Advanced Tokamak Plasmas,” Nucl. Fusion **42**, (2002) 972

- [14] K. L. Wong, *et al.*, “Internal Transport Barrier Driven by Redistribution of Energetic Ions,” *Nucl. Fusion* **45**, (2005) 30
- [15] D. S. Darrow, *et al.*, “Fast Ion Loss Diagnostic Plans for the National Spherical Torus Experiment,” *Rev. Sci. Instrum.* **72**, (2001)784
- [16] D. S. Darrow, *et al.*, “Measurements of Prompt and MHD-Induced Fast Ion Loss from National Spherical Torus Experiment Plasmas,” IAEA-CN-94/EX/P2-01, Proc. 19th Princeton Plasma Physics Laboratory Report, PPPL-3754 (2002)
- [17] K. G. McClements, *et al.*, “Physics of Energetic Particle-Driven Instabilities in the START Spherical Tokamak,” *Plasma Phys. Control. Fusion* **41** (1999) 661
- [18] E. D. Fredrickson, L. Chen and R. B. White, “Bounce Precession Fishbones in the National Spherical Torus Experiment,” *Nucl. Fusion* **43** (2003) 1258
- [19] N. N. Gorelenkov, *et al.*, “Beam Ion Driven Instabilities in the National Spherical Torus Experiment,” *Phys. Plasmas* **11**, (2004) 2586
- [20] E. D. Fredrickson, *et al.*, “Fast Ion Loss in a ‘Sea-or-TAE’), *Nucl. Fusion* **47**, (2006) S926 – S93
- [21] R. J. Akers, *et al.*, “Neutral Beam Heating in the START Spherical Tokamak,” *Nucl. Fusion* **42** (2002) 122
- [22] R. J. Akers, *et al.*, “Transport and Confinement in the Mega Ampere Spherical Tokamak (MAST) Plasma,” *Plasma Phys. Control. Fusion* **45** (2003) A175
- [23] M. R. Tournianski, *et al.*, “Anisotropic Fast Neutral Spectra in the MAST Spherical Tokamak,” *Plasma Phys. Control. Fusion* **47** (2005) 671
- [24] R. J. Goldston, D. C. McCune, H. H. Towner, *et al.*, “ New Techniques for Calculating Heat and Particle Source Rates due to Neutral Beam Injection in Axisymmetric Tokamaks,” *J. Comput. Phys.* **43** (1981) 61
- [25] J. Onega, M. Evrard, D. McCune, “Numerical Transport Codes,” *Transactions of Fusion Technology* **33** (1998) 181
- [26] F. M. Levinton, *et al.*, “Transport with Reversed Shear in the National Spherical Torus Experiment,” (Submitted to *Phys. Plasmas*)
- [27] S. S. Medley, D. S. Darrow and A. L. Roquemore, “Reconciliation of Measured and TRANSP-Calculated Neutron Emission Rates in the National Spherical Torus

Experiment: Circa 2002-2005,” Princeton Plasma Physics Laboratory Report, PPPL-4080 (2005)

- [28] S. S. Medley and A. L. Roquemore, “Neutral Particle Analyzer Diagnostic on in the National Spherical Torus Experiment,” *Rev. Sci. Instrum.* **75**, (2004) 3625
- [29] S. S. Medley and A. L. Roquemore, “Construction and Operation of Parallel Electric and Magnetic Field Spectrometers for Mass/Energy Resolved Multi-Ion Charge Exchange Diagnostics on the Tokamak Fusion Test Reactor,” *Rev. Sci. Instrum.* **69**, (1998) 2651
- [30] S. S. Medley, *et al.*, “Initial Neutral Particle Analyzer Measurements of Ion Temperature in the National Spherical Torus Experiment,” *Rev. Sci. Instrum.* **74**, (2003) 1896
- [31] S. S. Medley, R. E. Bell, E. D. Fredrickson, and A. L. Roquemore, “Energetic Ion Behavior in the National Spherical Torus Experiment,” *Proc. 30th EPS Conference on Controlled Fusion and Plasma Physics, St Petersburg, Russia, 7 - 11 July 2003, Europhysics Conference Abstracts Vol. 27A, P-4.96. Also Princeton Plasma Physics Laboratory Report, PPPL-3827 (2003)*
- [32] S. S. Medley, *et al.*, “Investigation of Collective Fast Ion Instability-induced Redistribution or Loss in the National Spherical Torus Experiment,” 21st IAEA Fusion Energy Conference, 16 – 21 October, Chengdu, China, CD-ROM EX/P6-13
- [33] S. S. Medley, D. S. Darrow, D. Liu and A. L. Roquemore, “Prompt Loss of Energetic Ion during Early Neutral Beam Injection in the National Spherical Torus Experiment,” Princeton Plasma Physics Laboratory Report, PPPL-4060 (2005)
- [34] B. P. LeBlanc, R. E. Bell, D. W. Johnson, *et al.*, “Operation of the NSTX Thomson Scattering System,” *Rev. Sci. Instrum.* **74** (2003) 1659
- [35] R. E. Bell, *et al.*, “Kinetic Profiles in NSTX Plasmas,” Princeton Plasma Physics Laboratory Report, PPPL-3591 (2001)
- [36] D. W. Johnson, *et al.*, “Diagnostic Development for ST Plasmas on NSTX,” *Plasma Phys. Control. Fusion* **45** (2003) 1975
- [37] S. Bernabei, *et al.*, “The Combined Effect of EPMS and TAEs on Energetic Ion Confinement and Sawtooth Stabilization,” *Nucl. Fusion* **41**, (2001) 513

- [38] E. M. Carolipio, *et al.*, “Simulations of Beam Ion Transport during Tearing Modes in the DIII-D Tokamak,” *Nucl. Fusion* **42**, (2002) 853
- [39] H. H. Duong, *et al.*, “Loss of Energetic Ions during TAE Instabilities,” *Nucl. Fusion* **33**, (1993) 749
- [40] M. P. Gryaznevich and S. E. Sharapov, “Beta-Dependence of Energetic Particle-Driven Instabilities in Spherical Tokamaks,” *Plasma Phys. Control. Fusion* **46**, (2004) S15 – S29
- [41] S. Briguglio, *et al.*, “Nonlinear Saturation of Shear Alfvén Modes and Self-consistent Energetic Ion Transport in Burning Plasmas with Advanced Tokamak Equilibria,” *Phys. Lett. A* **302**, (2002) 308
- [42] K. Shinohara, *et al.*, “Recent Progress of Alfvén Eigenmode Experiments using N-NB in JT-60U Tokamak,” *Plasma Phys. Control. Fusion* **42**, (2002) 942
- [43] K. Shinohara, *et al.*, “Energetic Particle Physics in JT-60U and JFT-2M,” *Plasma Phys. Control. Fusion* **46**, (2004) S31 – S45
- [44] F. Zonca, *et al.*, “Transition from Weak to Strong Energetic Ion Transport in Burning Plasmas,” *Nucl. Fusion* **45**, (2005) 477
- [45] J. E. Menard, *et al.*, “Internal Kink Mode Dynamics in High- β NSTX Plasmas,” *Nucl. Fusion* **45**, (2005) 539
- [46] E. D. Fredrickson, *et al.*, “Collective Fast Ion Instability-Induced Losses in National Spherical Torus Experiment,” Princeton Plasma Physics Laboratory Report, PPPL-4183 (2006)
- [47] N. A. Crocker, W. A. Peebles and S. Kubota, “Three-Wave Interactions between Fast-Ion Modes in the National Spherical Torus Experiment,” *Phys. Rev. Lett.* **97**, (2006) 045002
- [48] W. W. Heidbrink and G. J. Sadler, *Nucl. Fusion* **34**, (1994) 535
- [49] W. W. Heidbrink, *et al.*, “The Confinement of Dilute Populations of Beam Ions in the National Spherical Torus Experiment,” *Nucl. Fusion* **43**, (2003) 883
- [50] R. B. White and M. S. Chance, “Hamiltonian Guiding Center Drift Orbit Calculation for Plasmas of Arbitrary Cross Section,” *Phys. Fluids* **27**, (1984) 2455
- [51] R. B. White, “Canonical Hamiltonian Guiding Center Variables,” *Phys. Fluids B* **2**,

(1990) 845

[52] R. E. Bell, "Carbon Ion Plume Emission Produced by Charge Exchange with Neutral Beams on NSTX," Princeton Plasma Physics Laboratory Report, PPPL-4167 (2006)

[53] I. Voitsekhovitch, "Discrepancy in the Neutron Yield Simulated with TRANSP and Measurements," Private communication.

[54] T. Nishitani, *et al.*, "Attainment of High Fusion Reactivity under High Bootstrap Fraction in JT-60U," Nucl. Fusion **34**, (1994) 1069

[55] P. W. Ross, Princeton Plasma Physics Laboratory. Private communication.

[A1] D. V. Sivukhin, Reviews of Plasma Physics, Vol. **4**, Consultants Bureau, New York (1966) 93

[A2] T. H. Stix, Plasma Phys. **14** (1972) 367

[A3] L. Spitzer, Jr., Physics of Fully Ionized Gases, Interscience, New York (1962)

[A4] W. W. Heidbrink, "Accurate Measurements of the Pitch-Angle Scattering of Beam Ions," Phys. Plasmas **9** (2002) 28

[A5] D. L. Jassby, "Neutral-Beam-Driven Tokamak Fusion Reactors," Nucl. Fusion **17** (1977) 309

[A6] C. L. Fiore, S. S. Medley, G. W. Hammett, R. Kaita, A. L. Roquemore, and S. D. Scott, "Ion Temperature from Tangential Charge Exchange Neutral Analysis on the Tokamak Fusion Test Reactor," Nucl. Fusion **38** (1988) 1315

Figure Captions

Figure 1. A diagram showing the operating boundaries of NSTX, ITER, CTF and ARIES-ST in the dimensionless fast particle parameters.

Figure 2. Mirnov spectrogram of a neutral beam heated shot on NSTX showing the wide variety of fast particle modes.

Figure 3. The Neutral Particle Analyzer (NPA) on NSTX views across the three neutral beam injection sources and can be scanned horizontally (top) over a wide range of sightline tangency radii, R_{tan} , as well as vertically (bottom) on a shot-to-shot basis. R_{tan} is the perpendicular distance between the machine center and the NPA sightline.

Figure 4a. Pitch angle (left panel) and spatial (upper right panel) localization of the NPA flux arises from the intersection of the diagnostic sightline with the NB sources. Localization is strongest near the NB full energy, but remains substantial over the entire slowing down distribution. The maximum elevation minor radius accessible for vertical scanning depends on the choice of horizontal tangency radius (bottom panel).

Figure 4b. Localization of the NPA signal using NB notches.

Figure 5. Shown is an example of a display for correlating sFLIP ion loss images (left panels) with discharge waveforms and the Mirnov spectrogram and evolution of the NPA energetic ion distribution (right panels). In AVI mode, the dashed cursor advances with the sFLIP images.

Figure 6. Shown is an illustration of the USXR viewing arrays (top) and measurements that can be utilized for spatial localization of MHD activity.

Figure 7. A programmed reduction in the outer gap from $\Delta_{\text{gap}} \sim 12$ cm to $\Delta_{\text{gap}} \sim 5$ cm at $t \sim$

0.2 s causes a transient drop in the neutron yield (panel b) and a sustained reduction of the NPA energetic ion flux at $E_b > E/2$ (panels c and d).

Figure 8. TRANSP simulation (117299A04) of the NPA flux also shows an abrupt decrease with the programmed reduction in the outer gap from $\Delta_{\text{gap}} \sim 12$ cm to $\Delta_{\text{gap}} \sim 5$ cm at $t \sim 0.2$ s, consistent with measurements.

Figure 9. MHD activity for SN117299: (a) mode amplitude for $f = 0-100$ kHz (black curve) and $f = 200-2000$ kHz (red curve) and Mirnov spectrograms for (b) $f = 200-2000$ kHz and (c) $f = 0-100$ kHz with the outer gap excursion overlaid (red curve).

Figure 10. Selected plasma waveforms and Mirnov spectrogram for discharge 117449.

Figure 11. MPTS contour plots show that for SN117449 a reconnection event at $t \sim 0.6$ s (see Fig. 9) leads to a collapse in the core electron density (top panel) and an increase in the core electron temperature (bottom panel).

Figure 12. CHERS contour plots show that for SN117449 a reconnection event at $t \sim 0.6$ s (see Fig. 9) leads to a collapse in the core toroidal rotation velocity (top panel) and an increase in the core Z_{eff} (bottom panel).

Figure 13. TRANSP calculations of the neutron yield evolution (top panel) are sensitive to the value of the edge neutral density, $n_o(a)$, assumed in the run setup. The calculated neutron yield decreases in the range $n_o(a) = 4.5 \times 10^{10} - 4.5 \times 10^{13} \text{ cm}^{-3}$ but asymptotes at lower and higher values (bottom panel).

Figure 14a. TRANSP simulations of the NPA flux, S_{npa} , are also sensitive to the assumed value of the edge neutral density, $n_o(a)$, early in the discharge when the electron density is relatively low and ramping up. No effect is observed at higher electron density because the edge neutrals are screened from the plasma core region where the S_{npa} charge

exchange source is localized.

Figure 14b. Typical profiles of the neutral density components used in TRANSP analysis (panel (a)) and fast ion power loss due to charge exchange for two values of the edge neutral density (panel(b)).

Figure 15. Shown is an illustration of the categories of MHD-induced redistribution or loss of energetic ions.

Figure 16. Shown is an illustration of the neutron loss (top panel) due to bursting EPM activity (center panel) and the associated spikes in the NPA energetic ion spectrum (bottom panel) that occur primarily at lower energies.

Figure 17. Shown is an illustration of the neutron loss (center panel) due to overlapping multiple MHD modes (top panel) and associated spikes in the NPA energetic ion spectrum (bottom panel).

Figure 18a. Shown is an illustration of the neutron loss (upper panel) due to sawtooth activity (center panel) and associated spikes in the NPA energetic ion spectrum that occur at all energies.

Figure 18b. Shown is the correlation of the spike in the NPA flux with the neutron crash during a sawtooth.

Figure19. Illustration of the NPA energetic ion spectrum for SN117449 showing depletion of the measured flux that occurs primarily above $E_p/2$.

Figure 20. Illustration of the anomalous fast ion diffusion parameters used in TRANSP for SN117449.

Figure 21. USXR measurement of MHD activity for SN117449 supports the core-localized modeling of anomalous fast ion diffusion shown in Fig. 20.

Figure 22. Shown are results of TRANSP simulation using anomalous fast ion diffusion for SN117449. Black lines are measurements and red/blue lines are TRANSP simulations with/without anomalous fast ion diffusion. The time of interest is $t = 0.6 - 1.0$ s.

Figure 23. Matching of the measured energetic ion distribution with TRANSP AFID model.

Figure 24. Matching MSE-reconstructed and calculated current profiles using AFID in TRANSP for NBICD redistribution.

Figure 25. Mirnov spectrograms for SN117449 covering the high ($f = 200-2000$ kHz) and low frequency ($f = 0-100$ kHz) ranges.

Figure 26. Selected plasma waveforms and Mirnov spectrogram for SN120001.

Figure 27. Shown is a TRANSP simulation of the neutron yield and NPA signal for SN120001.

Figure 28. Measured parameters for SN115789 used in the horizontal NPA scan.

Figure 29. Shown is a NPA horizontal scanning measurement of energetic ion redistribution.

Figure 30. Depletion of the measured NPA flux is shown as a function of horizontal tangency radius from H_Scan 21 (black points) augmented by other scan data (red points). The blue curve maps the NPA tangency radius to the major radius corresponding to spatial localization of the NPA measurements. The shaded area shows that maximum NPA flux depletion occurs at $R_{\text{tan}} \sim 50 \pm 20$ cm corresponding to $R_{\text{maj}} \sim 75 \pm 10$ cm. From the upper left panel in Fig. 4a, the energetic ion depletion is associated primarily with passing ions.

Figure 31. Comparison of TRANSP ion spectra with and without fast ion diffusion for a simulated NPA vertical scan (119768M22).

Figure 32. Discharge characteristics for the NPA vertical scan: SN122631.

Figure 33. NPA vertical scan during MHD-quiescent (top panel) and MHD-active (bottom panel) discharge periods.

Figure 34. NPA vertical scan during NBI into a gas-filled torus with toroidal fields only ($B_T = 3.5 - 5.5$ kG) that is a condition used for calibration of the MSE diagnostic.

Figure 35. Discharge characteristics for SN117126, a representative discharge with strong MHD activity but null energetic ion redistribution effects.

Figure 36. The top panel shows the normalized measured (black curve) and TRANSP-simulated (red curve) NPA signal evolution and the outer gap width for SN117126. The bottom panel shows the measured energetic ion distribution.

Figure 37. ORBIT modeling of the particle trajectories viewed by the NPA diagnostic during horizontal scanning measurements is shown.

Figure 38. Contour plot of the primary neutral footprint for an NSTX heating beam.

Figure 39. Contour plot of the beam ion distribution at $E = 65$ keV showing a sample (red circles) of the pitch angles ($v_{||}/v$) that are viewed by the NPA during horizontal scanning.

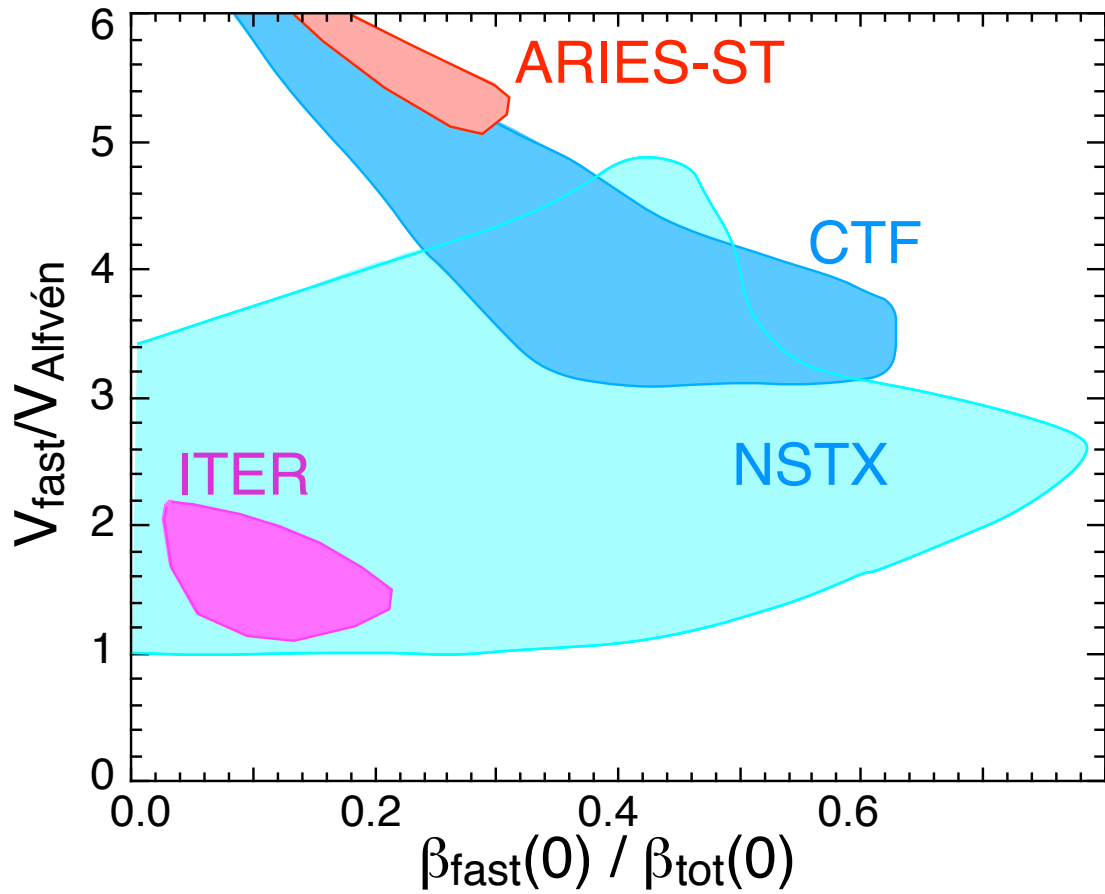


Fig. 1. Diagram showing the operating boundaries of NSTX, ITER, CTF and ARIES-ST in the dimensionless fast particle parameters.

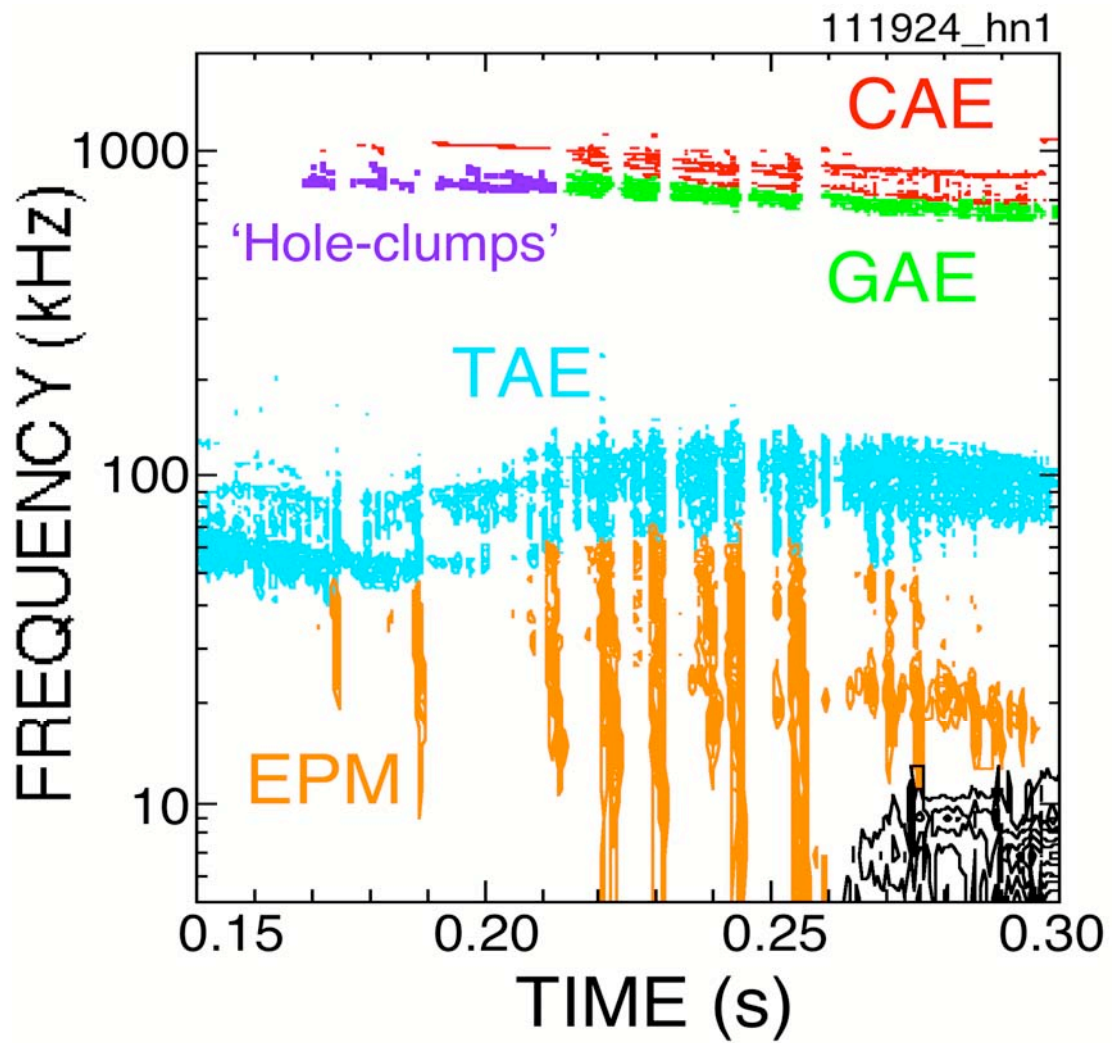
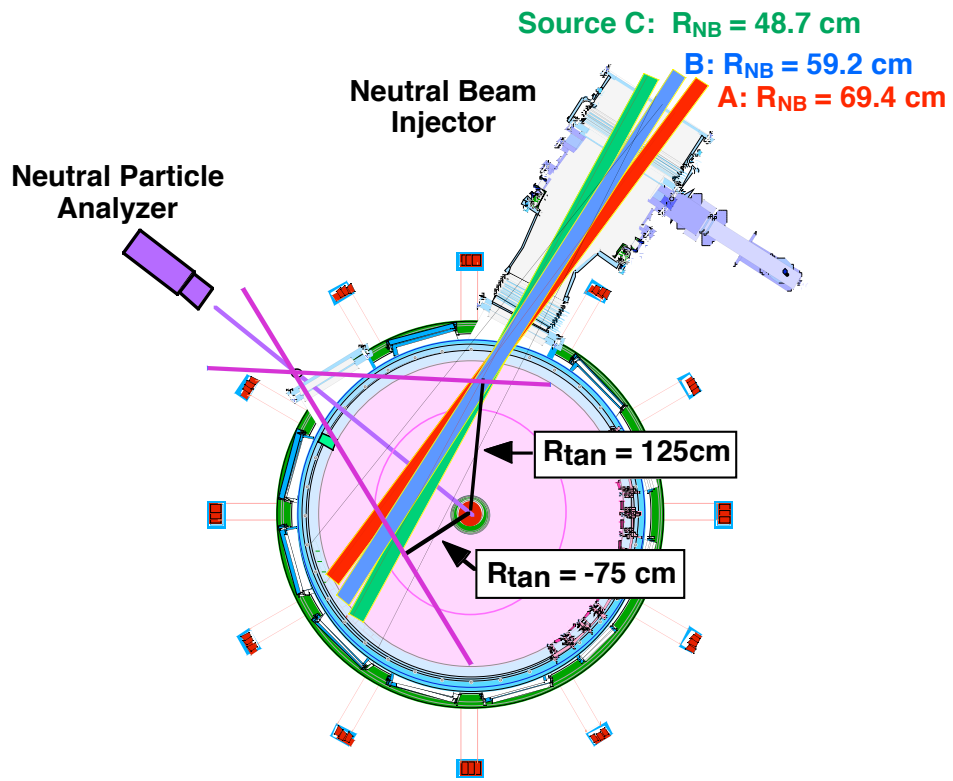


Fig. 2. Mirnov spectrogram of a neutral beam heated shot on NSTX showing the wide variety of fast particle modes.



SN111522, $t = 0.3$ s

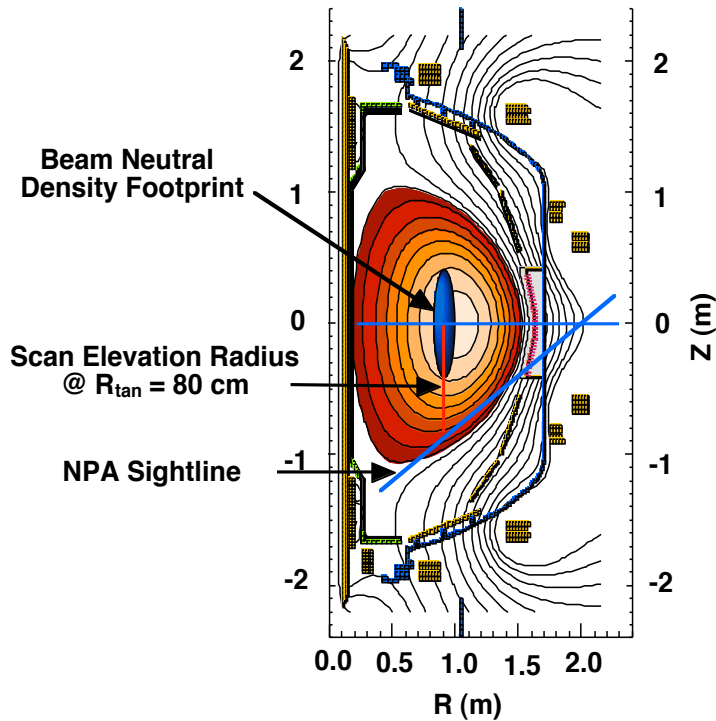


Fig. 3. The Neutral Particle Analyzer (NPA) on NSTX views across the three neutral beam injection sources and can be scanned horizontally (top) over a wide range of sightline tangency radii, R_{tan} , as well as vertically (bottom) on a shot-to-shot basis. R_{tan} is the perpendicular distance between the machine center and the NPA sightline.

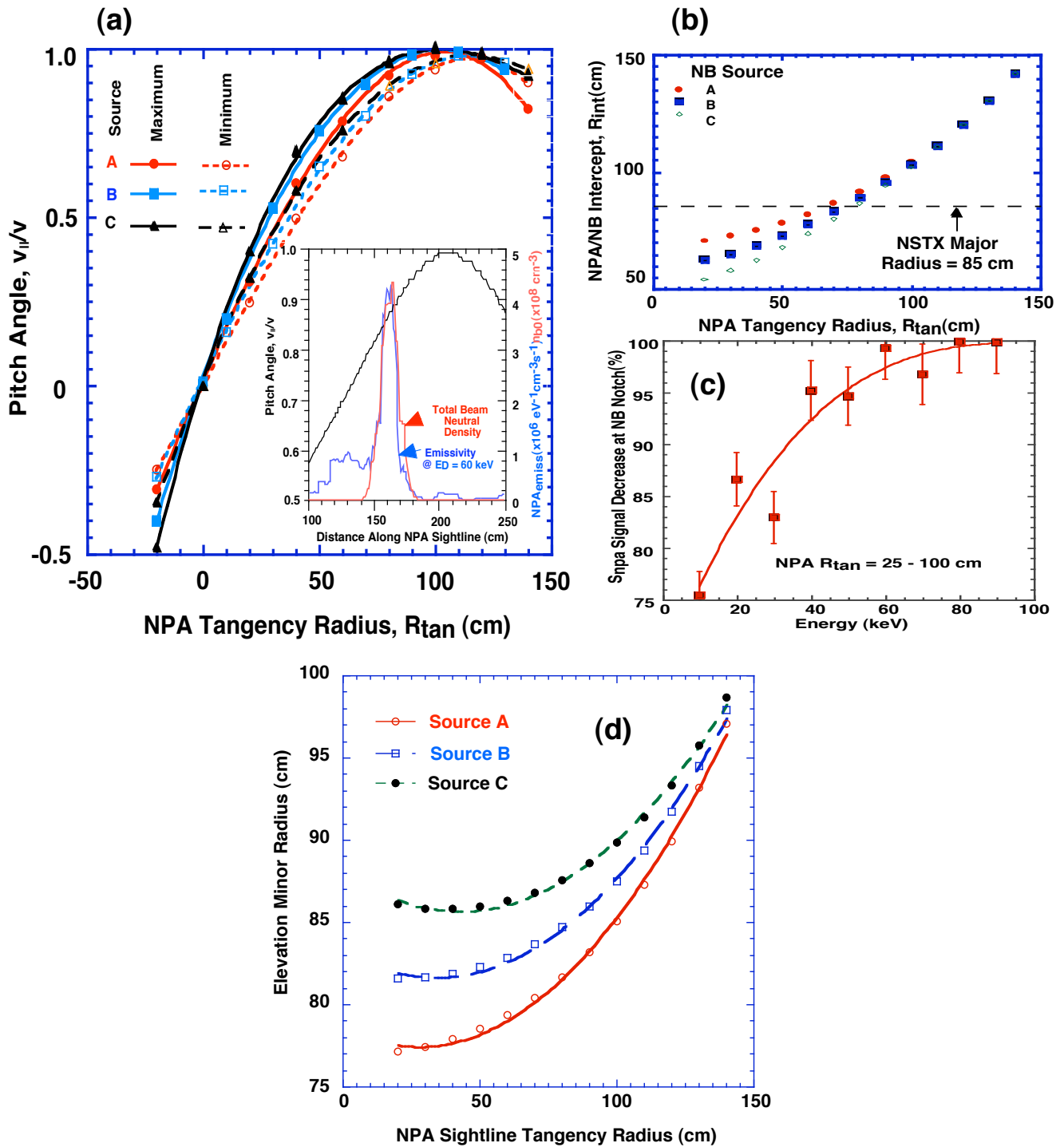


Fig. 4a. Pitch angle (left panel) and spatial (upper right panel) localization of the NPA flux arises from the intersection of the diagnostic sightline with the NB sources. Localization is strongest near the NB full energy, but remains substantial over the entire slowing down distribution. The maximum elevation minor radius accessible for vertical scanning depends on the choice of horizontal tangency radius (bottom panel).

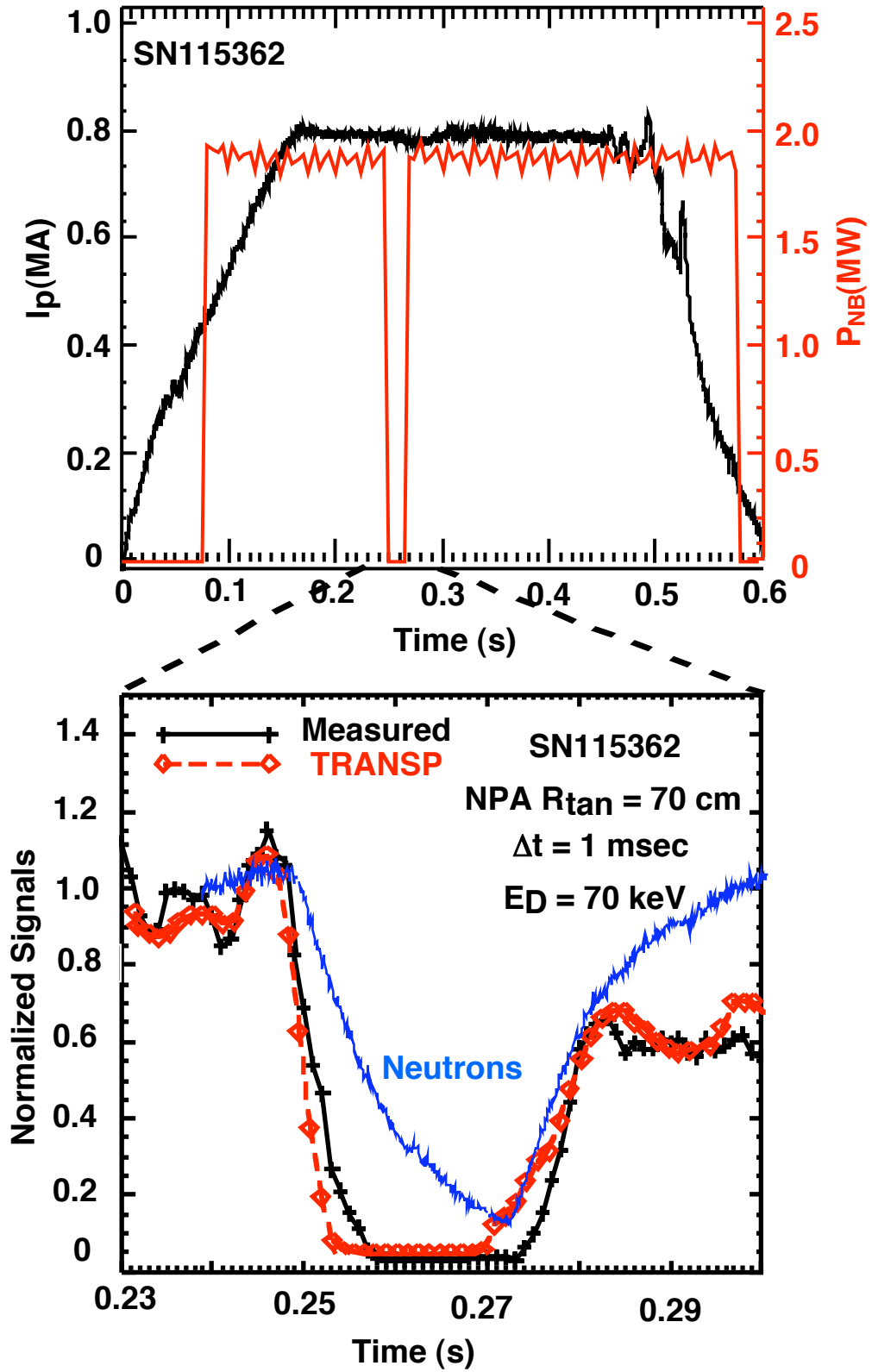


Fig. 4b. Localization of NPA signal using NB notches.

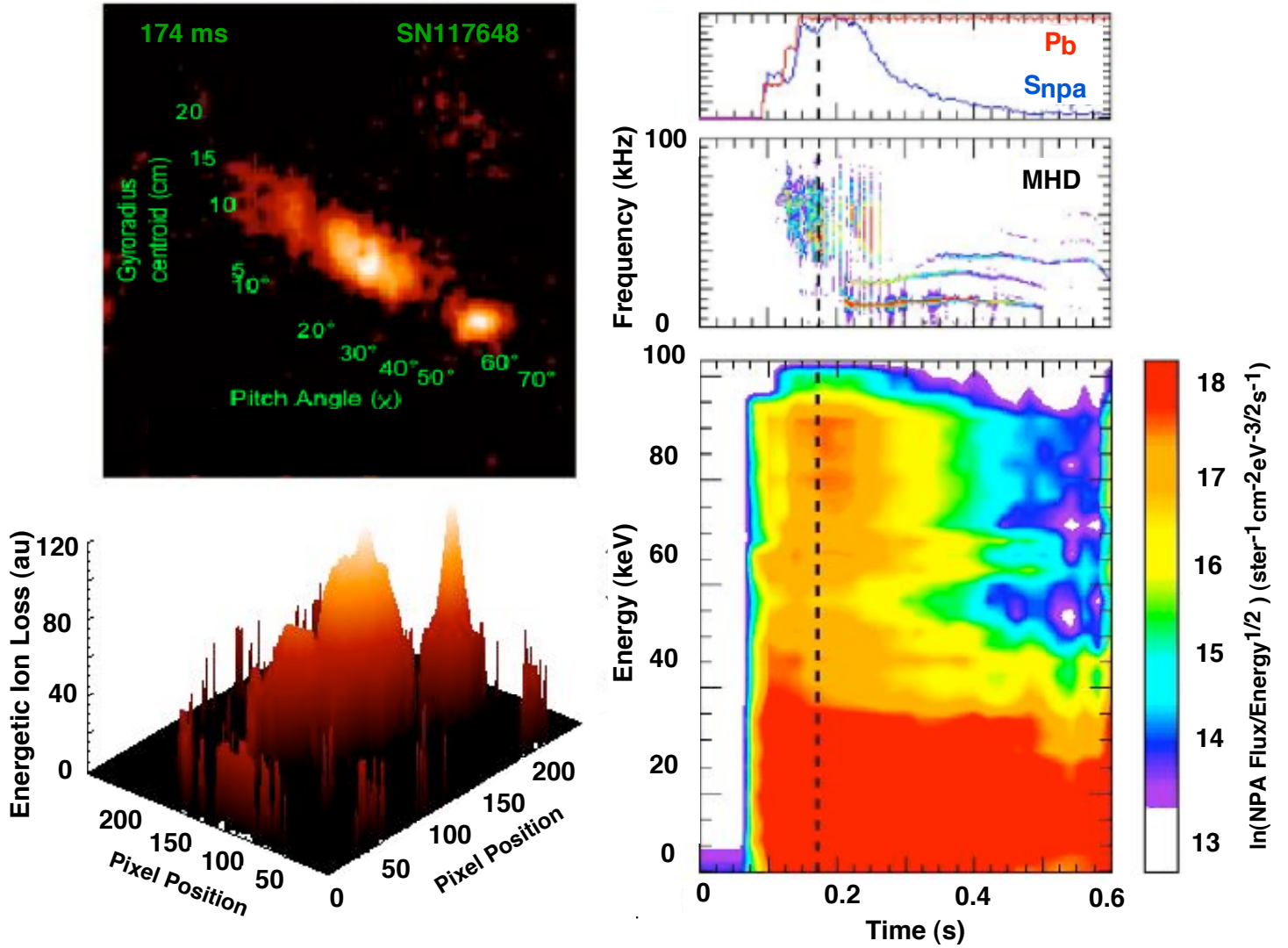


Fig. 5. Example of a display for correlating sFLIP ion loss images (left panels) with discharge waveforms and the Mirnov spectrogram (upper left panel) and evolution of the NPA energetic ion distribution (right panels). In AVI mode, the dashed cursor advances with the sFLIP images.

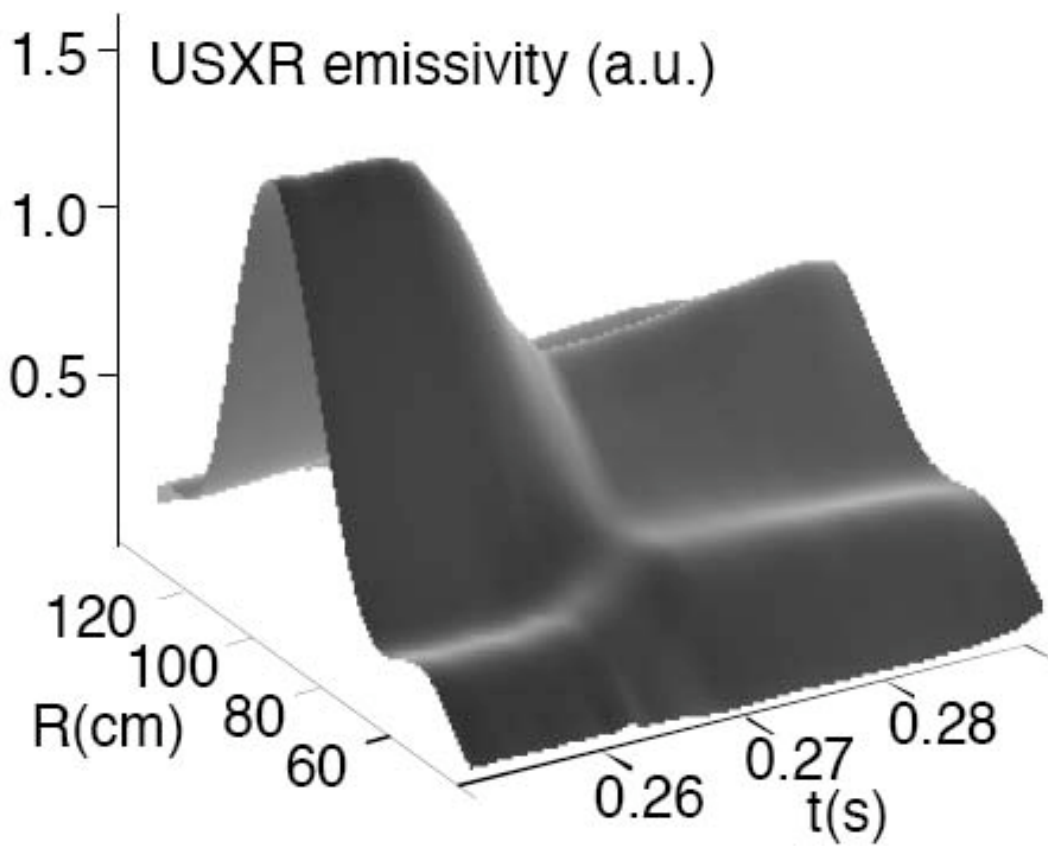
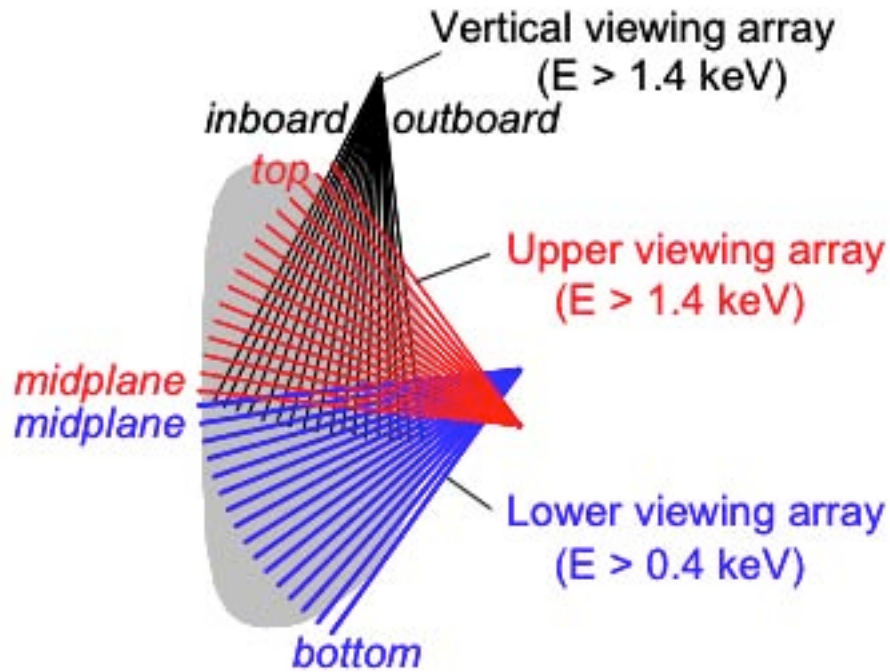


Fig. 6. Illustration of USXR viewing arrays (top) and measurements that can be utilized for spatial localization of MHD activity (bottom).

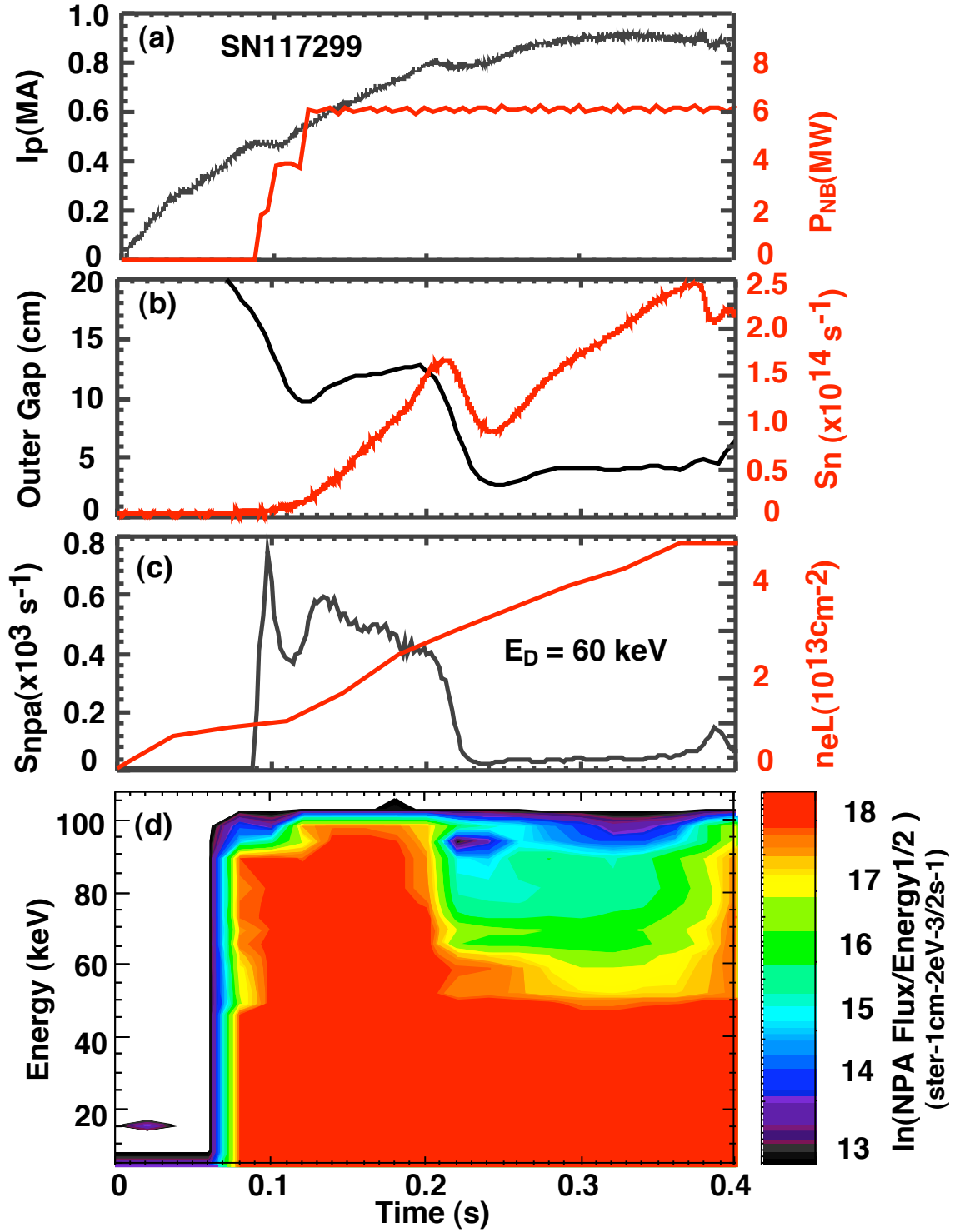


Fig. 7. A programmed reduction in the outer gap from $\Delta_{gap} \sim 12 \text{ cm}$ to $\Delta_{gap} \sim 5 \text{ cm}$ at $t \sim 0.2 \text{ s}$ causes a transient drop in the neutron yield (panel b) and a sustained reduction of the NPA energetic ion flux at $E_p > E/2$ (panels c and d).

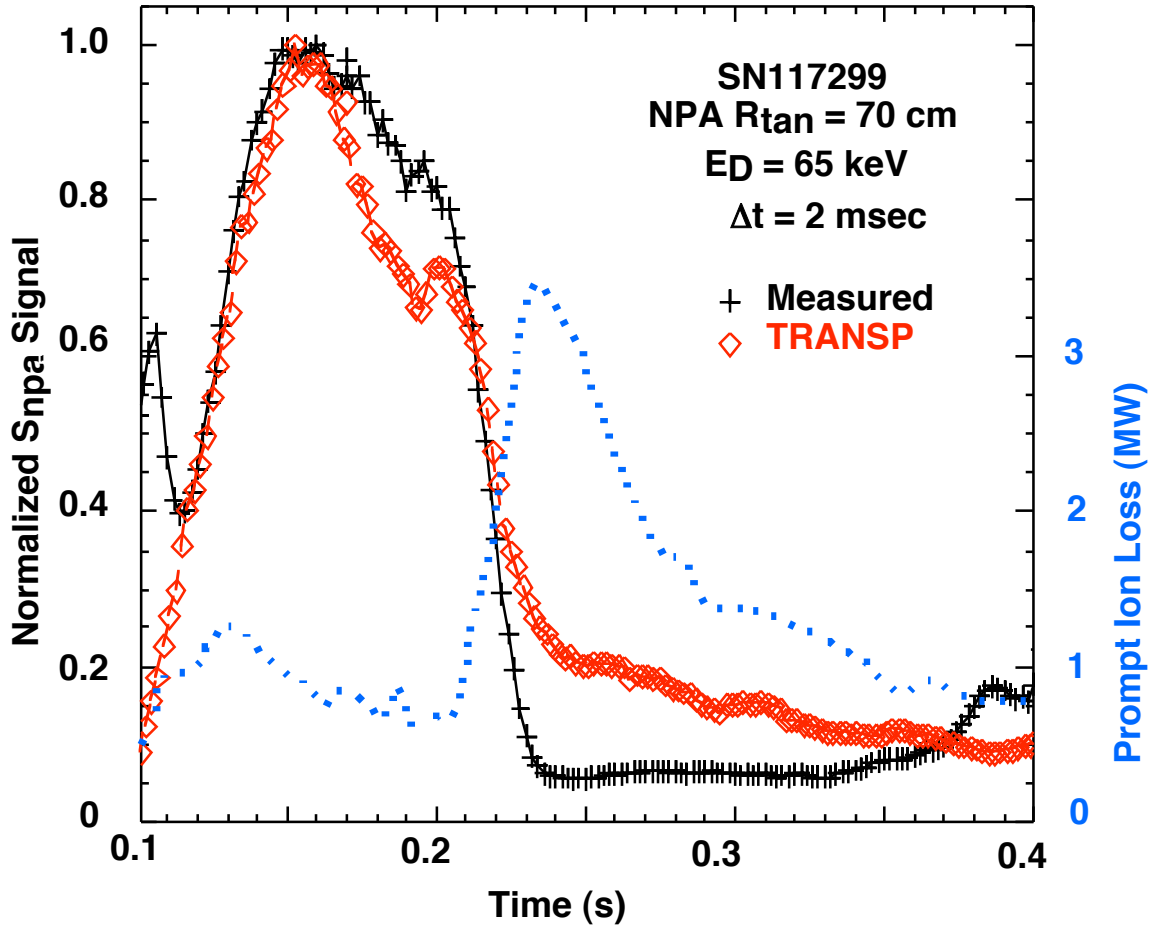


Fig. 8. TRANSP simulation of the NPA flux also shows an abrupt decrease with the programmed reduction in the outer gap from $\Delta_{gap} \sim 12$ cm to $\Delta_{gap} \sim 5$ cm at $t \sim 0.2$ s. consistent with measurements.

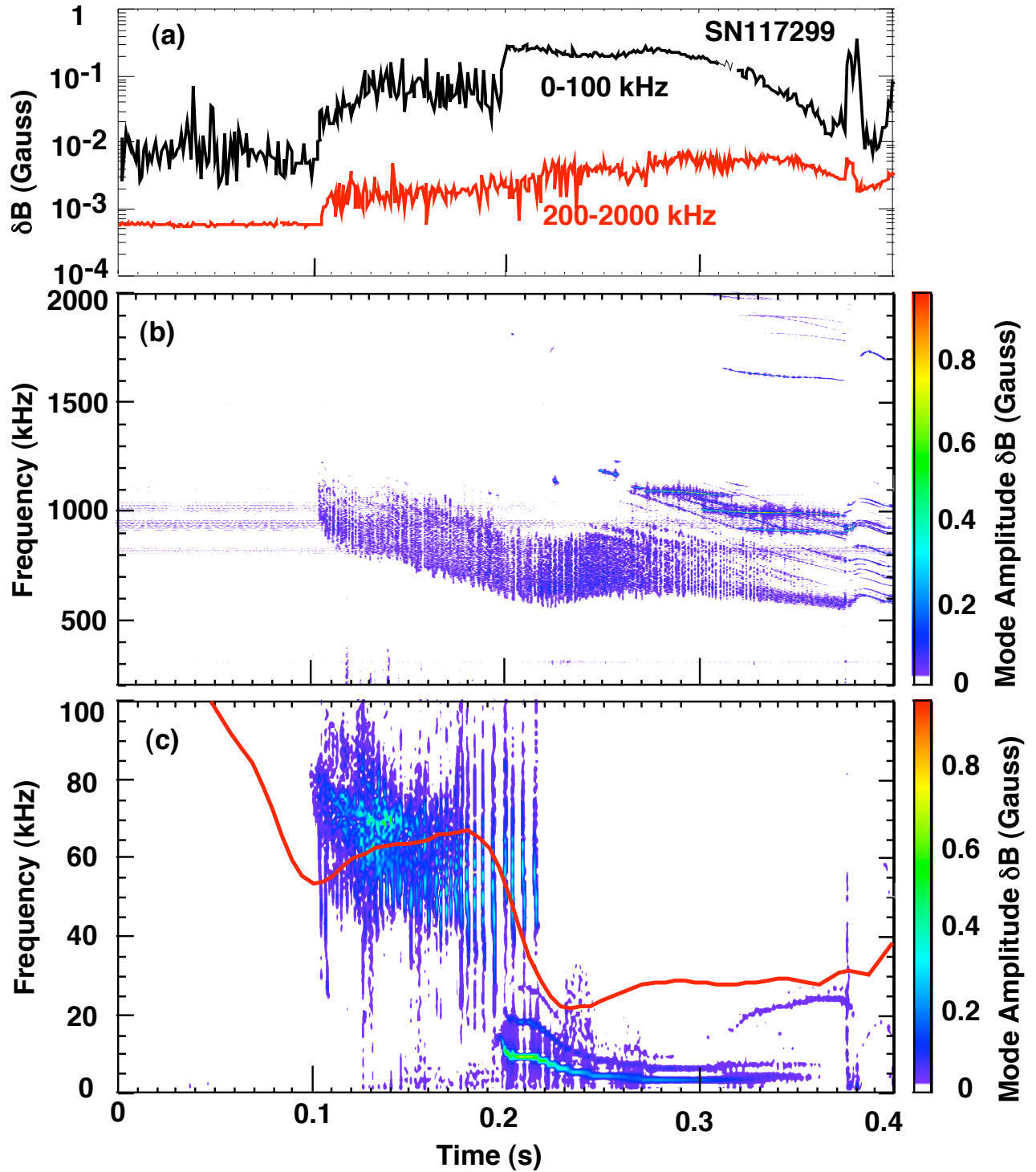


Fig. 9. MHD activity for SN117299: (a) mode amplitude for $f = 0-100$ kHz (black curve) and $f = 200-2000$ kHz (red curve) and Mirnov spectrograms for (b) $f = 200-2000$ kHz and (c) $f = 0-100$ kHz with the outer gap excursion overlaid (red curve).

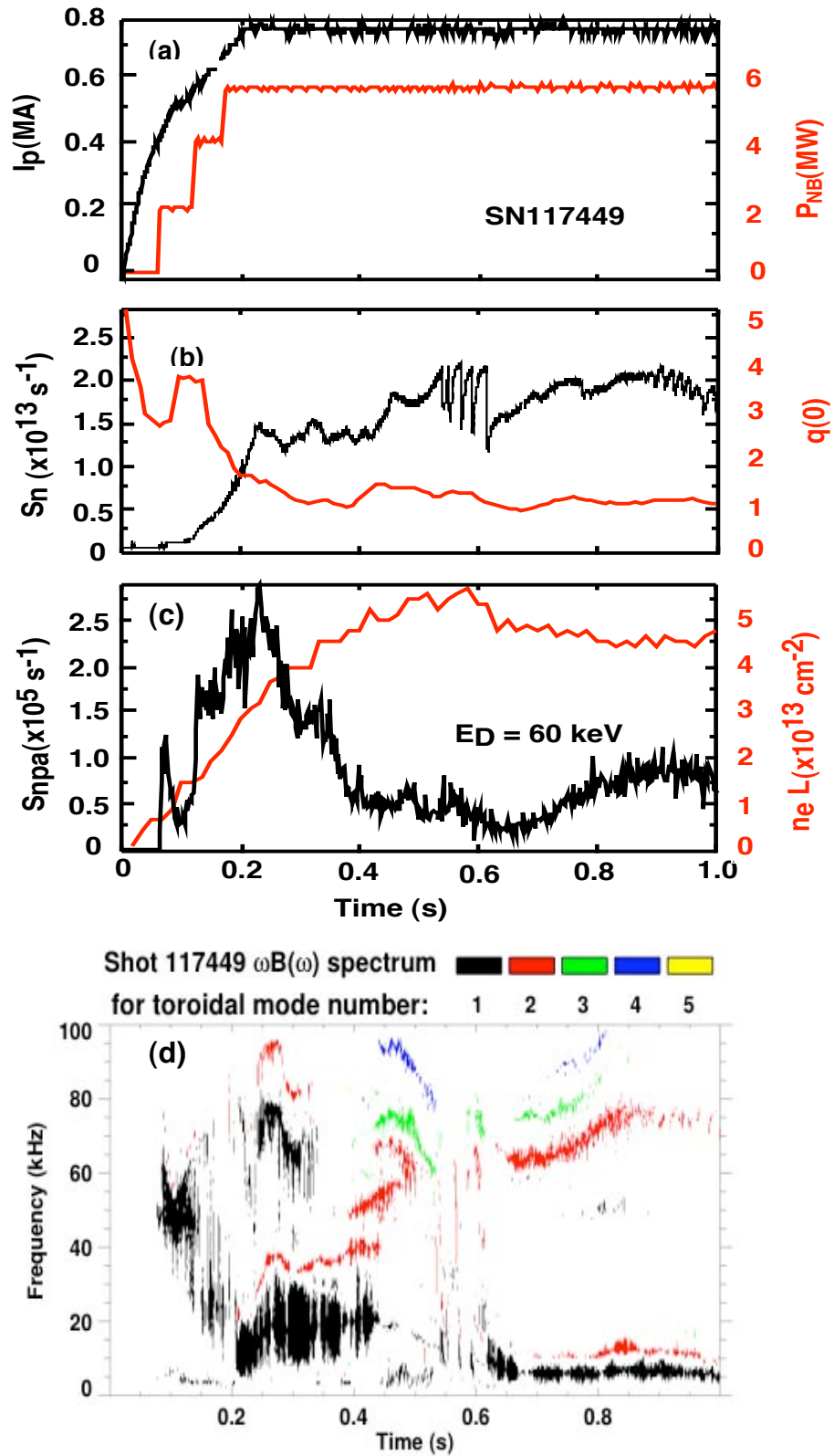


Fig. 10. Selected plasma waveforms and Mirnov spectrogram for discharge 117449.

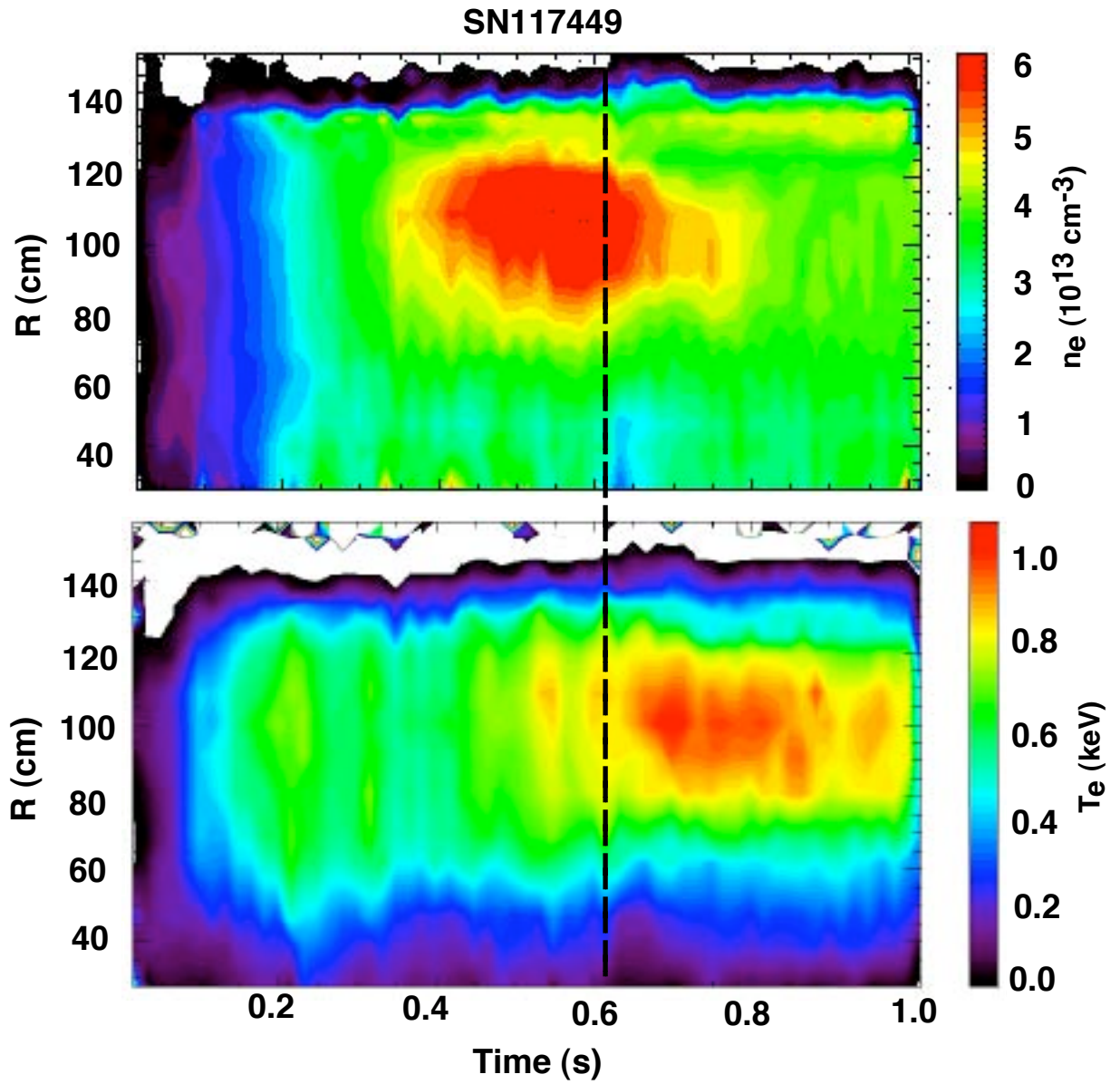


Fig. 11. MPTS contour plots show that for SN117449 a reconnection event at $t \sim 0.6$ s (see Fig. 9) leads to a collapse in the core electron density (top panel) and an increase in the core electron temperature (bottom panel).

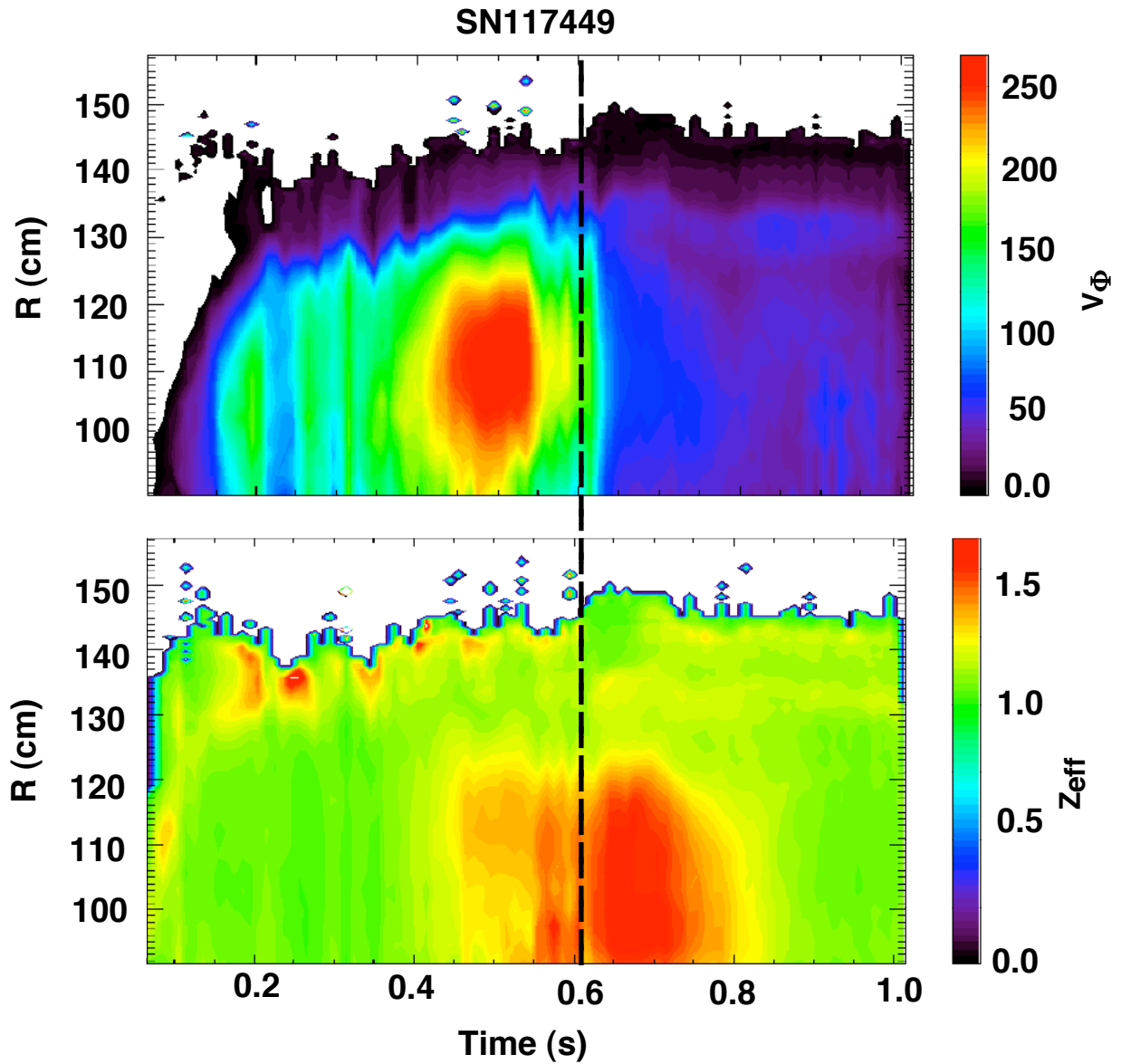


Fig. 12. *CHERS* contour plots show that for SN117449 a reconnection event at $t \sim 0.6$ s (see Fig. 9) leads to a collapse in the core toroidal rotation velocity (top panel) and an increase in the core Z_{eff} (bottom panel).

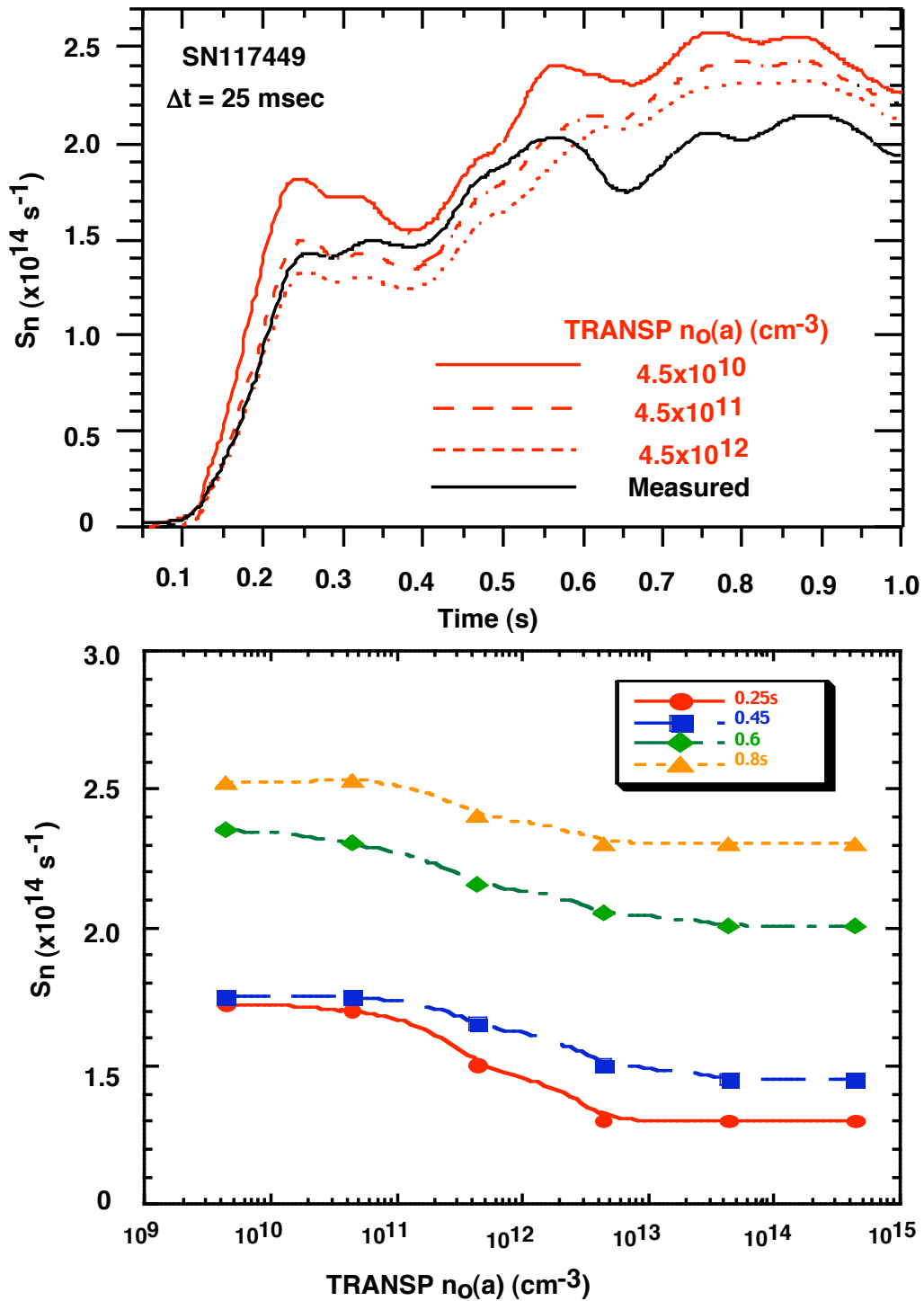


Fig. 13. TRANSP calculations of the neutron yield evolution (top panel) are sensitive to the value of the edge neutral density, $n_o(a)$, assumed in the run setup. The calculated neutron yield decreases in the range $n_o(a) = 4.5 \times 10^{10} - 4.5 \times 10^{13} \text{ cm}^{-3}$ but asymptotes at lower and higher values (bottom panel).

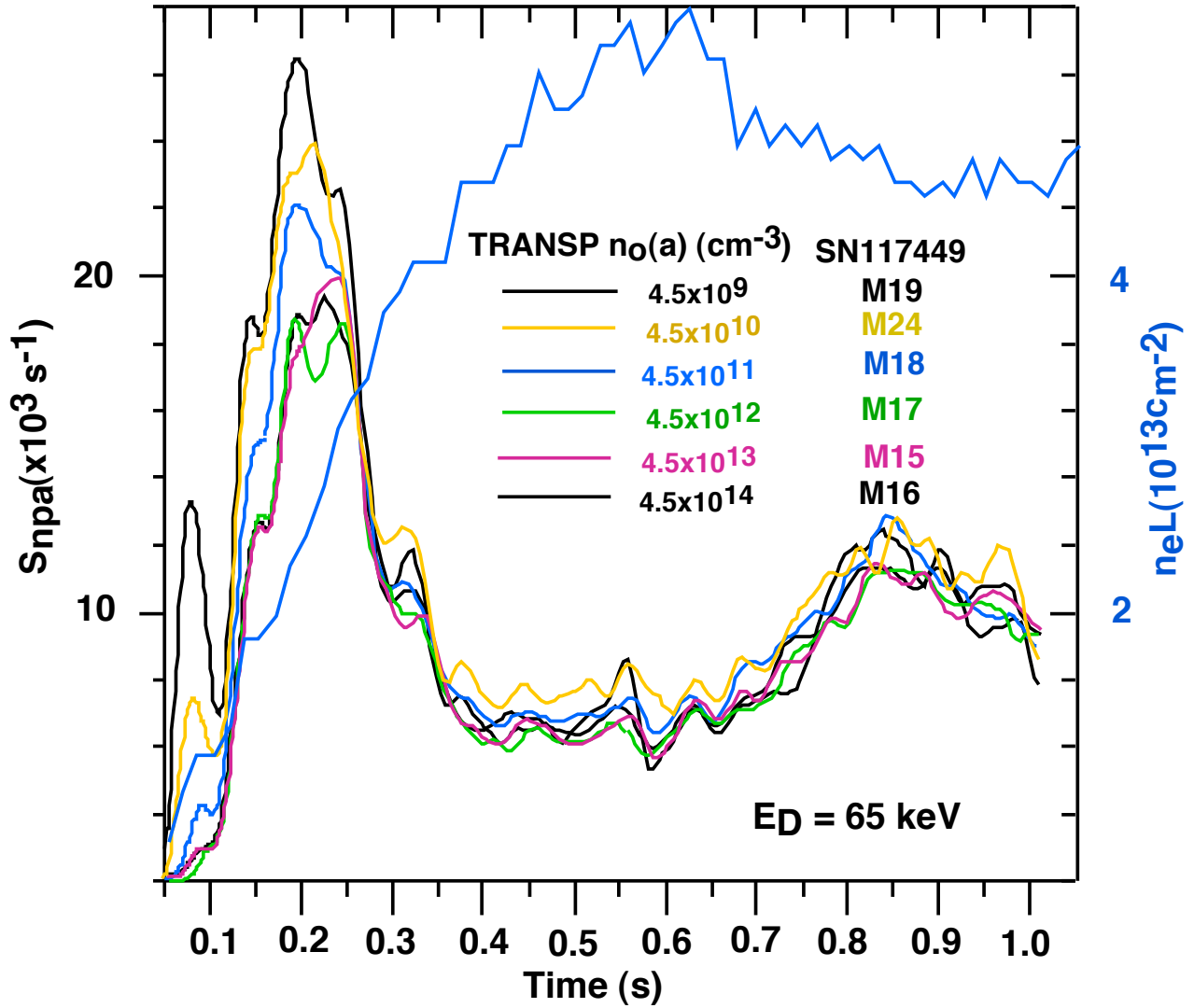


Fig. 14a. TRANSP simulations of the NPA flux, S_{npa} , are also sensitive to the assumed value of the edge neutral density, $n_o(a)$, early in the discharge when the electron density is relatively low and ramping up. No effect is observed at higher electron density because the edge neutrals are screened from the plasma core region where the S_{npa} charge exchange source is localized.

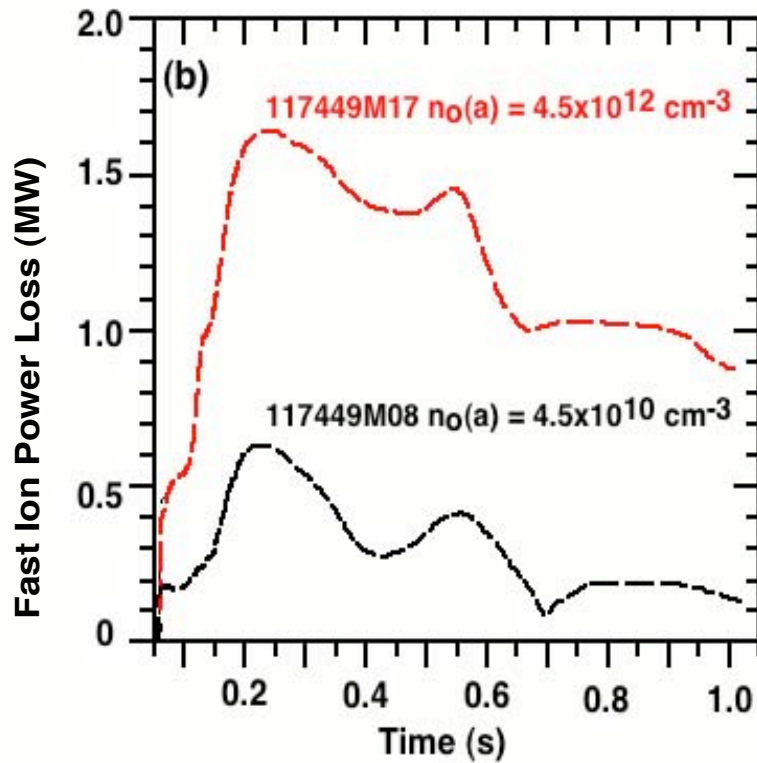
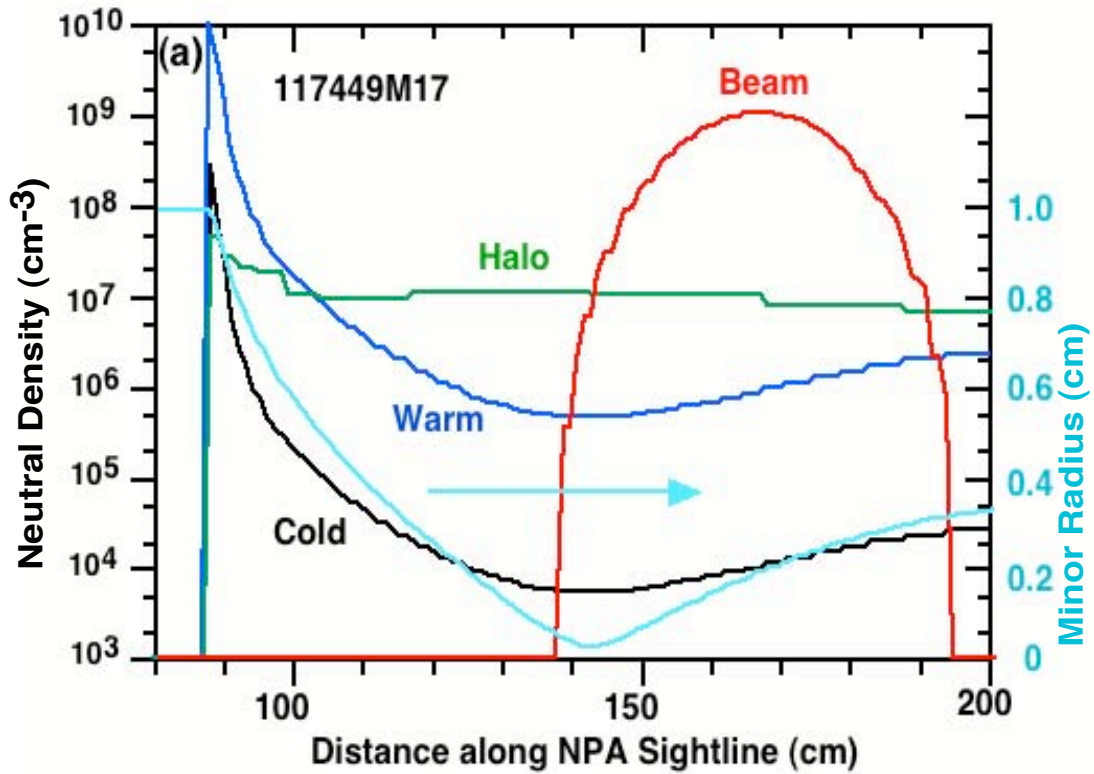


Fig. 14b. Typical profiles of the neutral density components used in TRANSP analysis (panel (a)) and fast ion power loss due to charge exchange for two values of the edge neutral density (panel(b)).

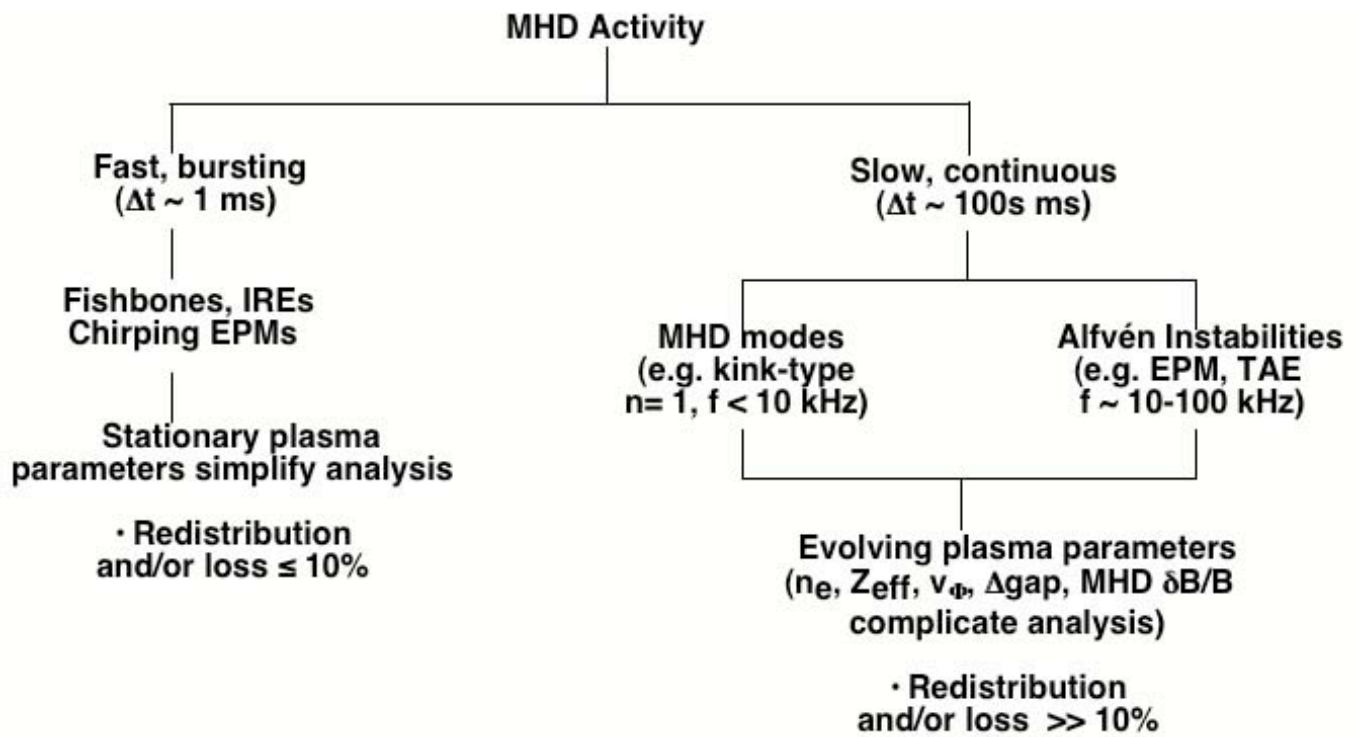


Fig. 15. Illustration of categories of MHD-induced redistribution or loss of energetic ions.

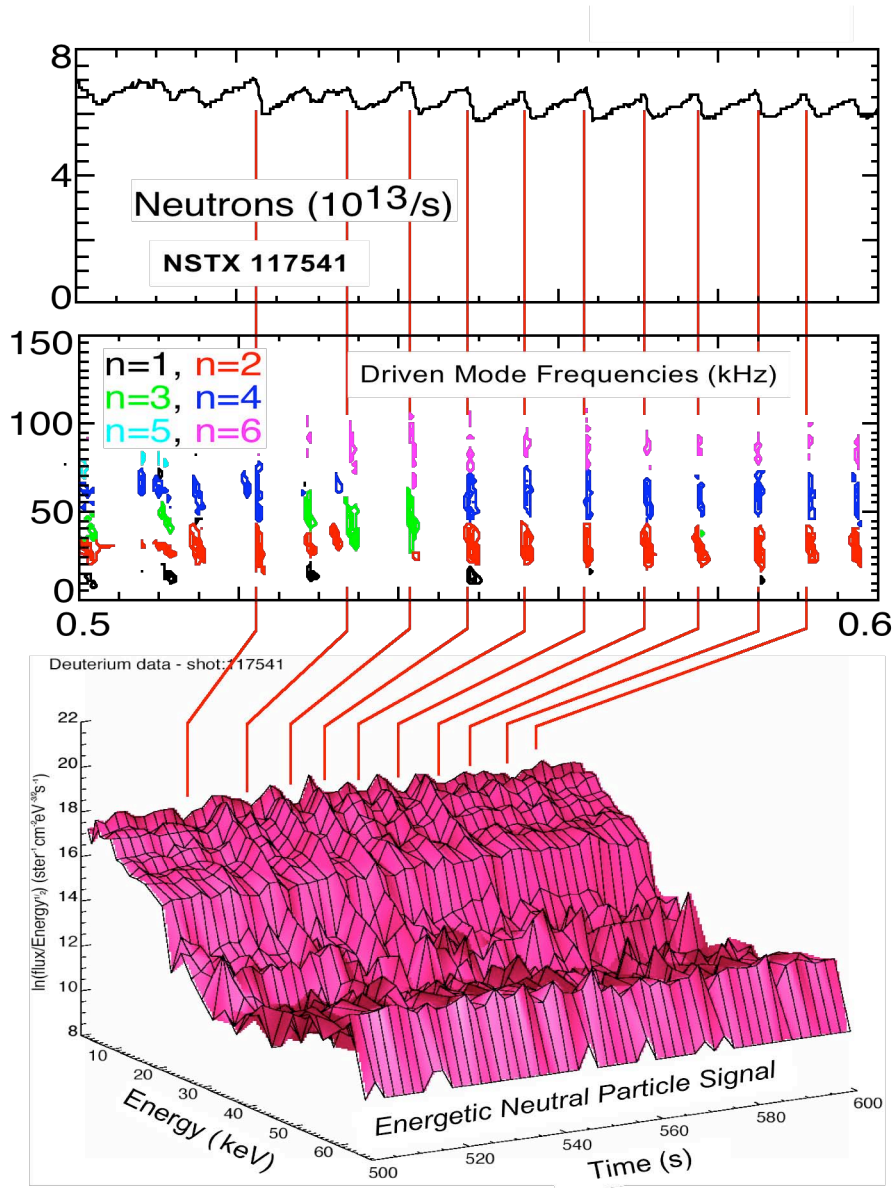


Fig. 16. Illustration of neutron loss (top panel) due to bursting EPM activity (center panel) and associated spikes in the NPA energetic ion spectrum (bottom panel) that occur primarily at lower energies.

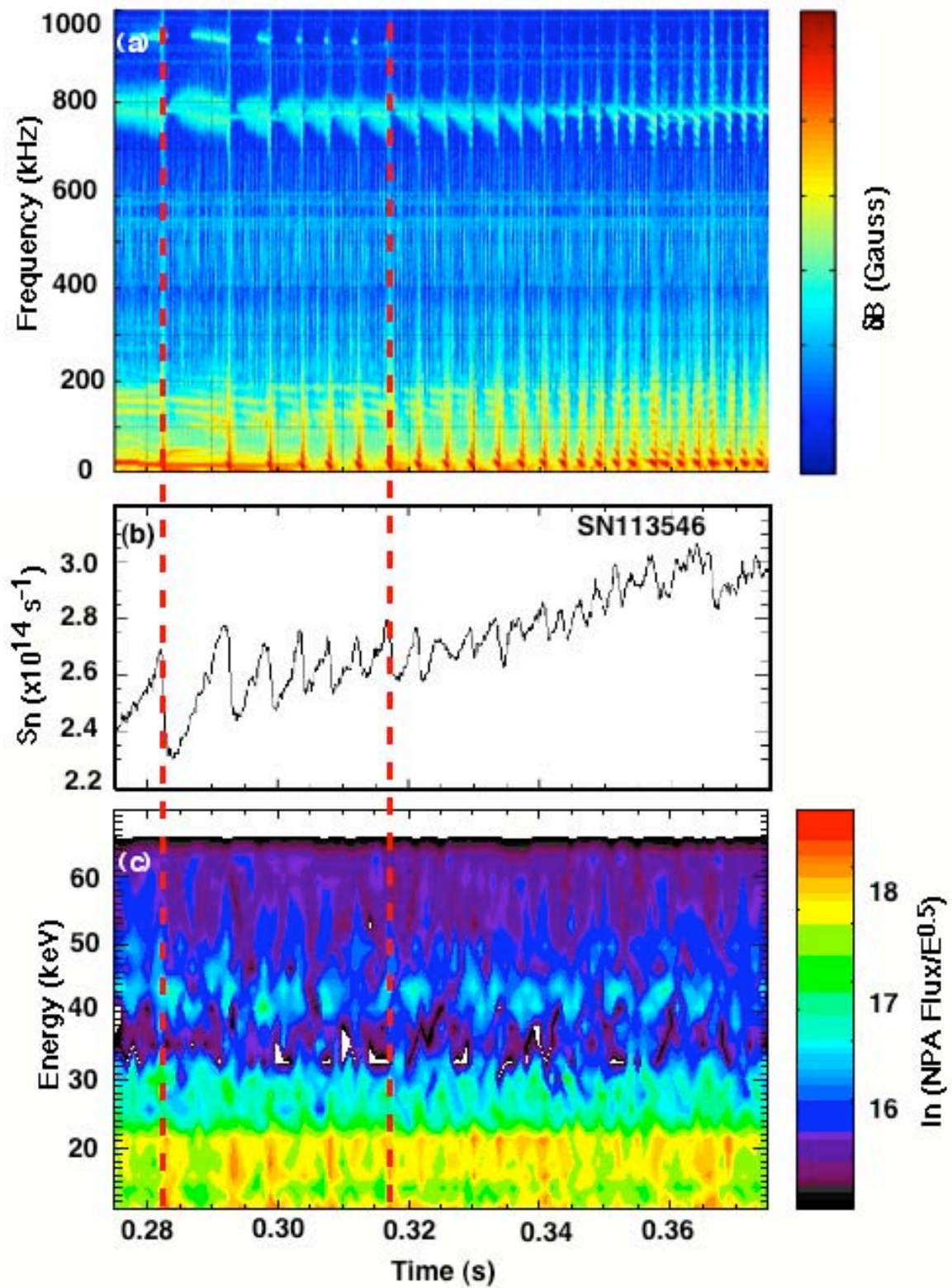


Fig. 17. Illustration of neutron loss (center panel) due to overlapping multiple MHD modes (top panel) and associated spikes in the NPA energetic ion spectrum (bottom panel).

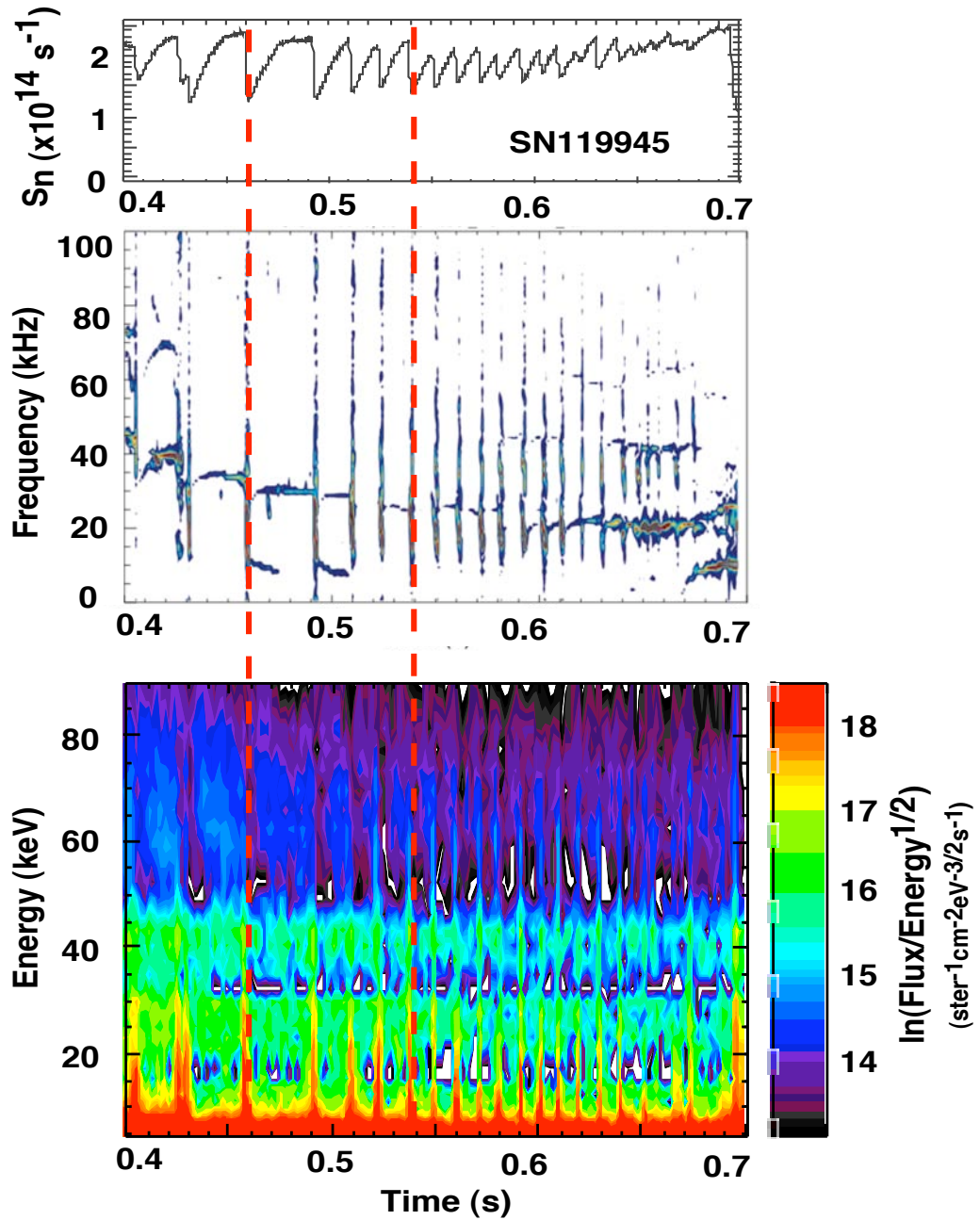


Fig. 18a. Illustration of neutron loss (upper panel) due to sawtooth activity (center panel) and associated spikes in the NPA energetic ion spectrum that occur at all energies.

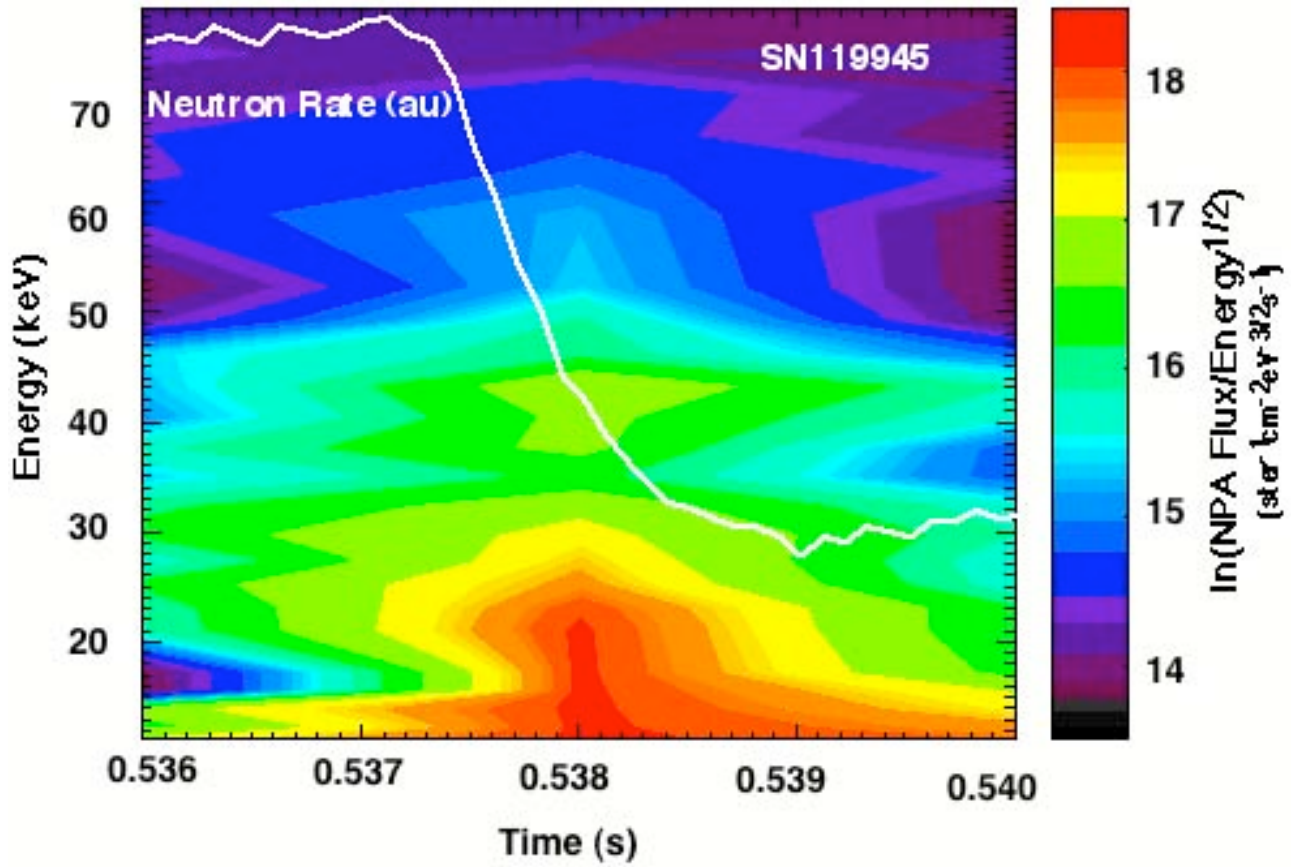


Fig. 18b. Correlation of the spike in the NPA flux with the neutron crash during a sawtooth.

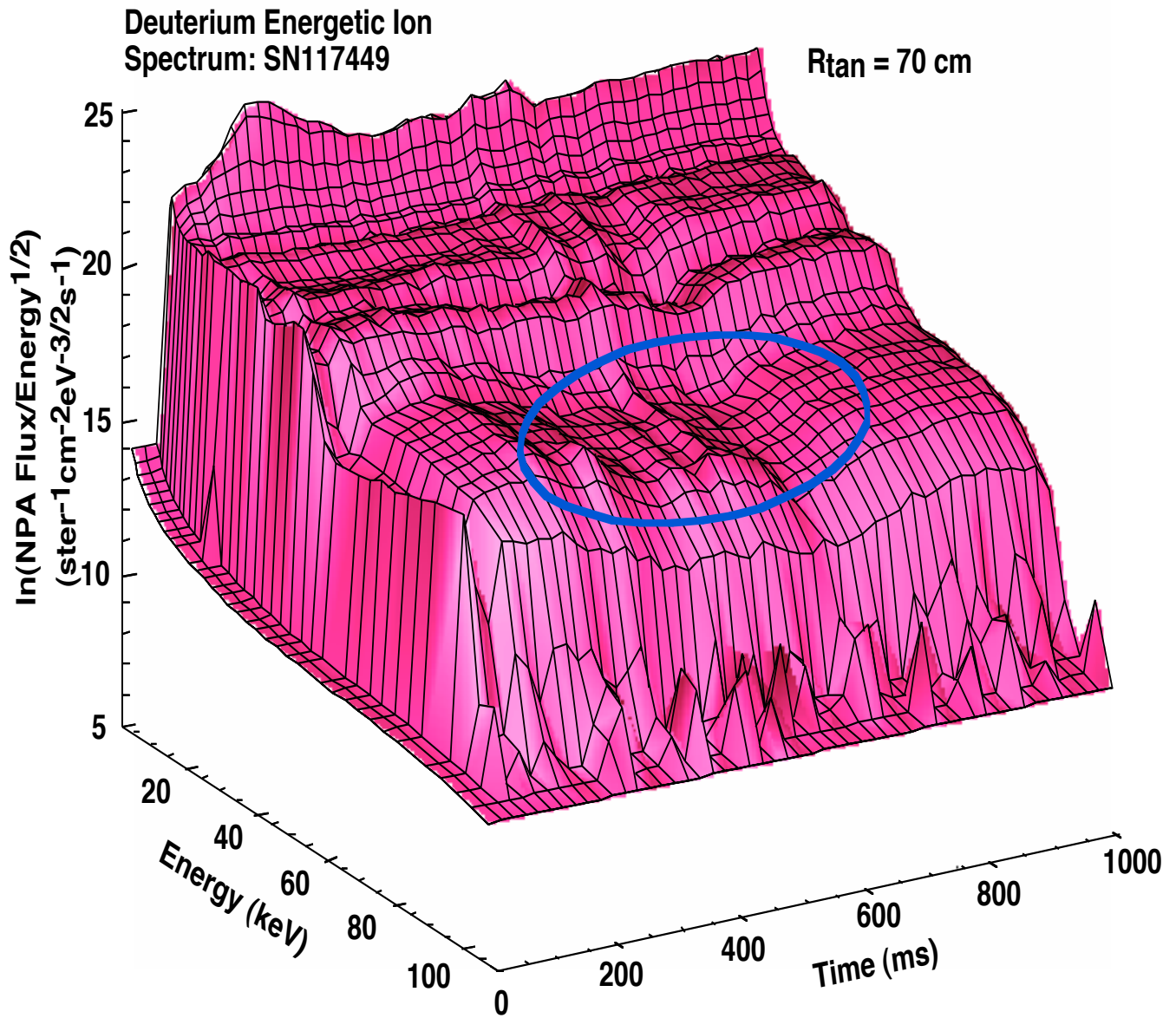


Fig.19. Illustration of the NPA energetic ion spectrum for SN117449 showing depletion of the measured flux primarily above $E_{\nu}/2$.

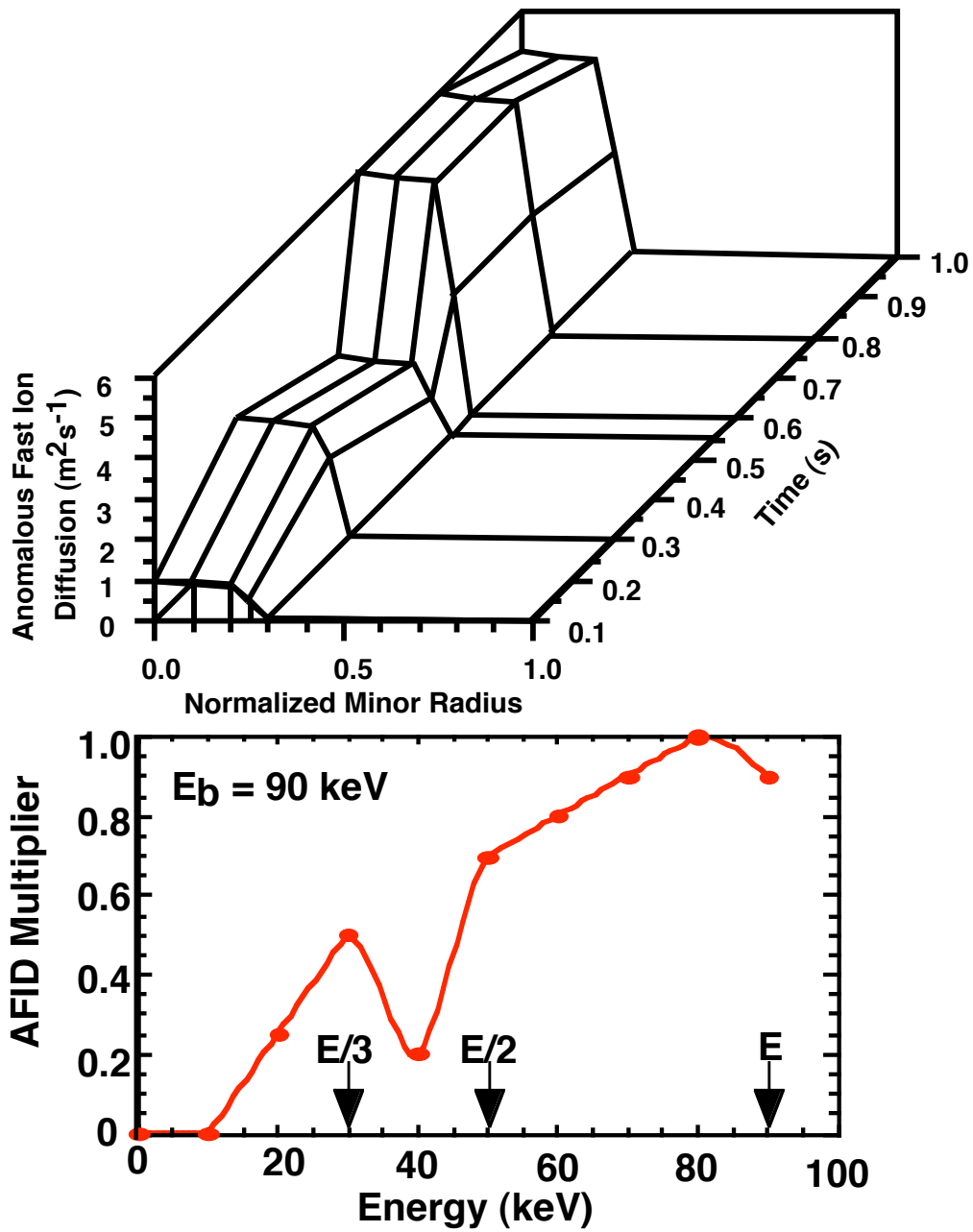


Fig. 20. Illustration of the TRANSP anomalous fast ion diffusion parameters utilized in TRANSP for SN117449.

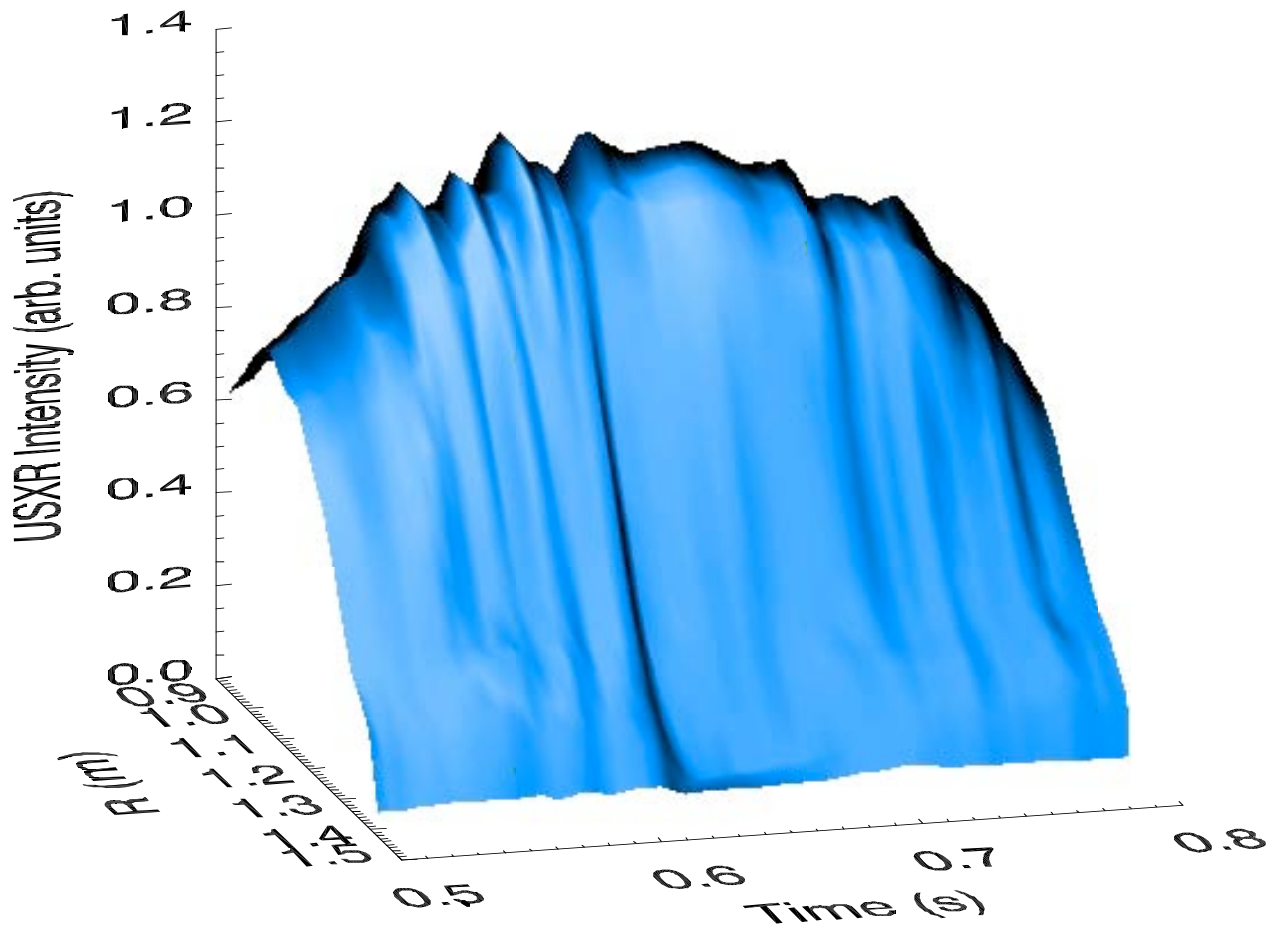


Fig. 21. USXR measurement of MHD activity for SN117449 supports the core-localized modeling of anomalous fast ion diffusion shown in Fig. 20.

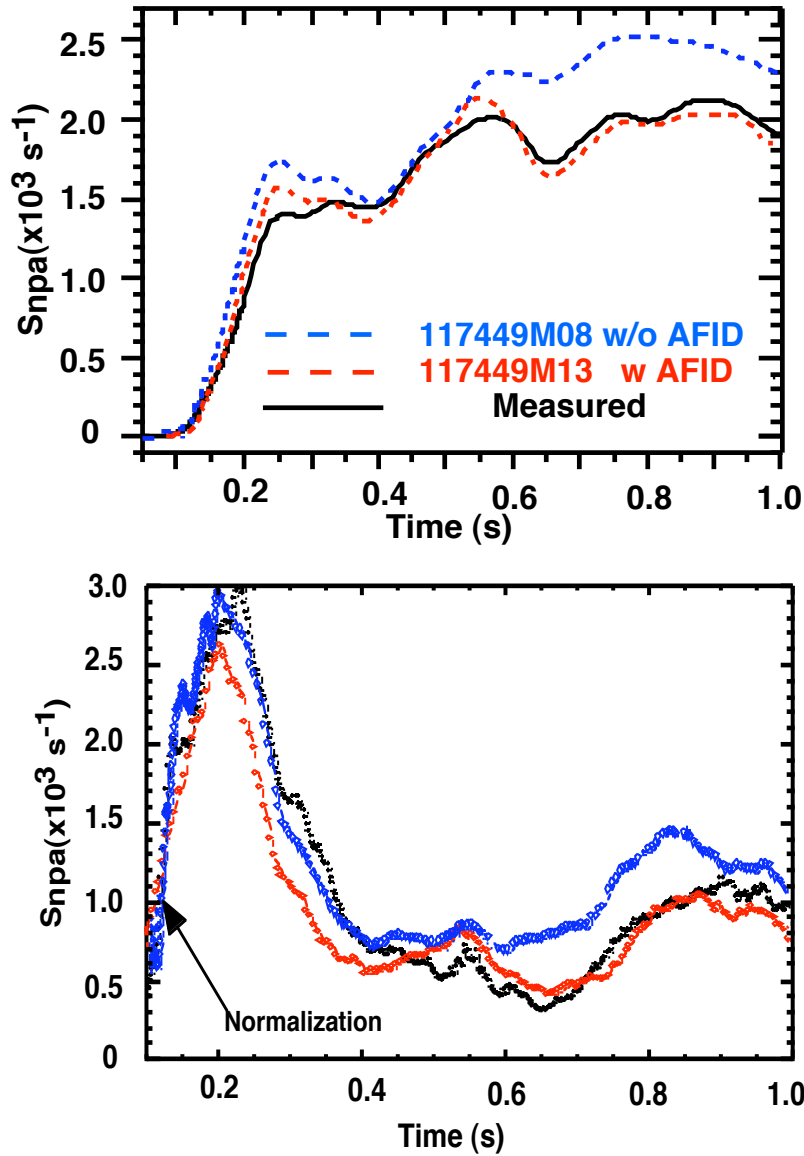


Fig. 22. Shown are results of TRANSP simulation using anomalous fast ion diffusion for discharge 117449. Black lines are measurements and red/blue lines are TRANSP simulations with/without anomalous fast ion diffusion. The time of interest is 0.6 – 1.0 s.

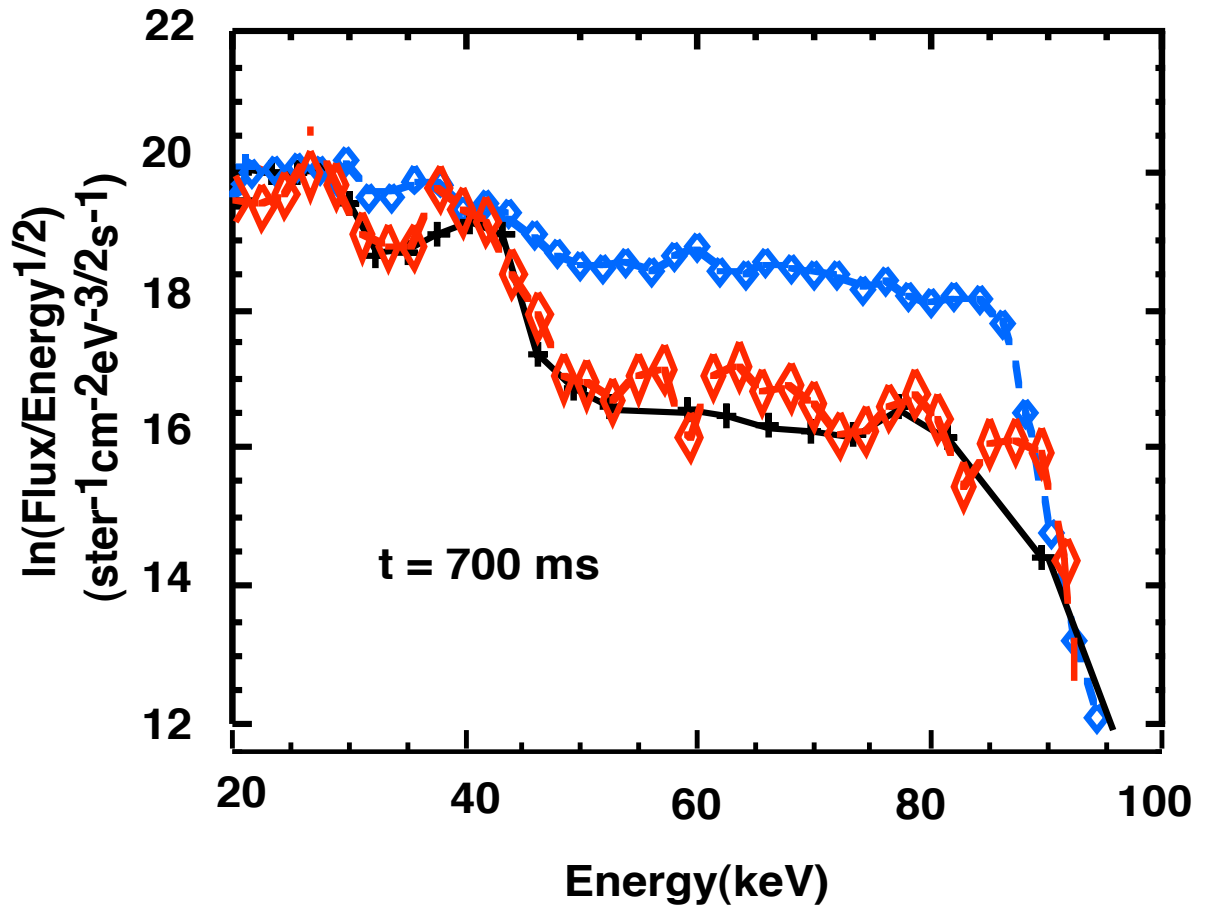


Fig. 23. Matching of the measured energetic ion distribution with TRANSP AFID model.

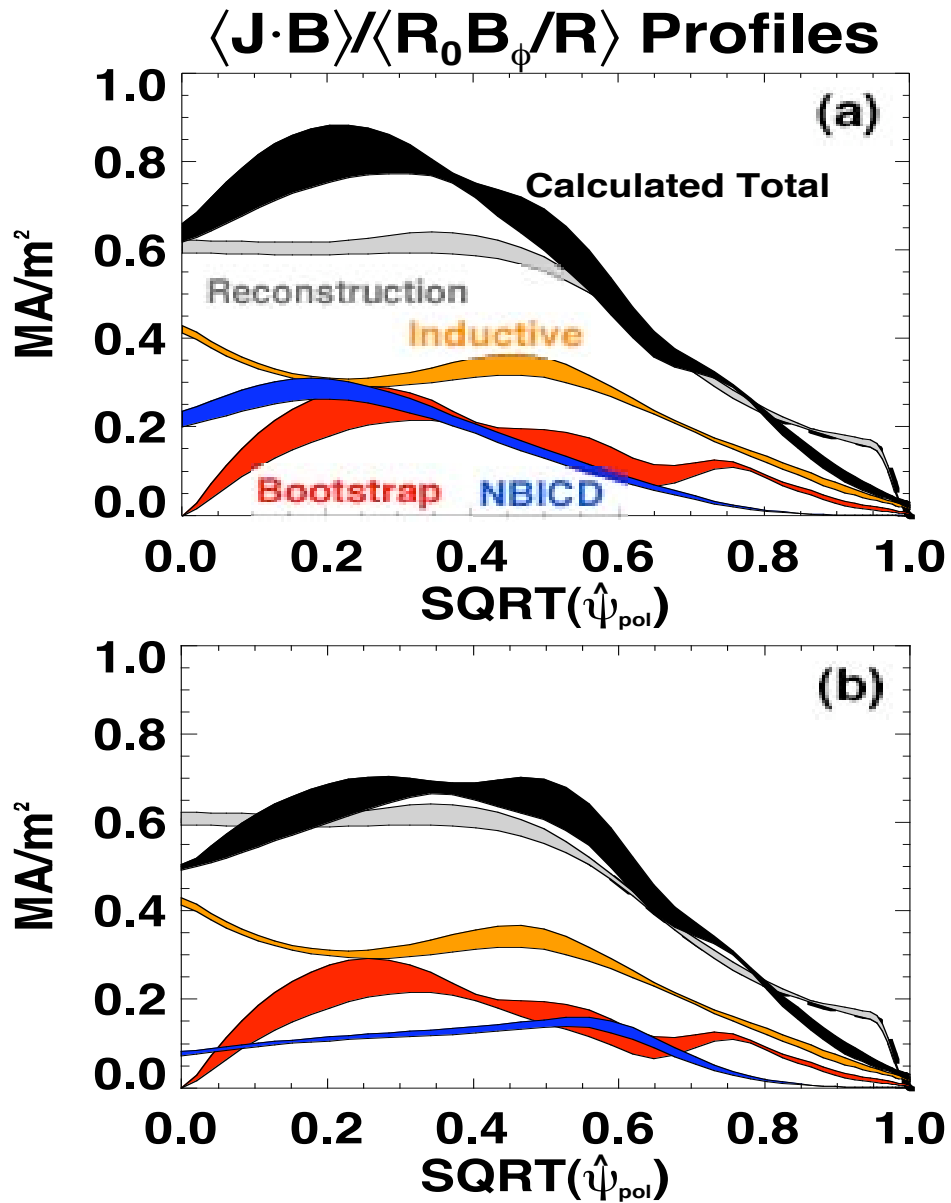


Fig. 24. Matching MSE-reconstructed and calculated current profiles using AFID in TRANSP for NBICD redistribution.

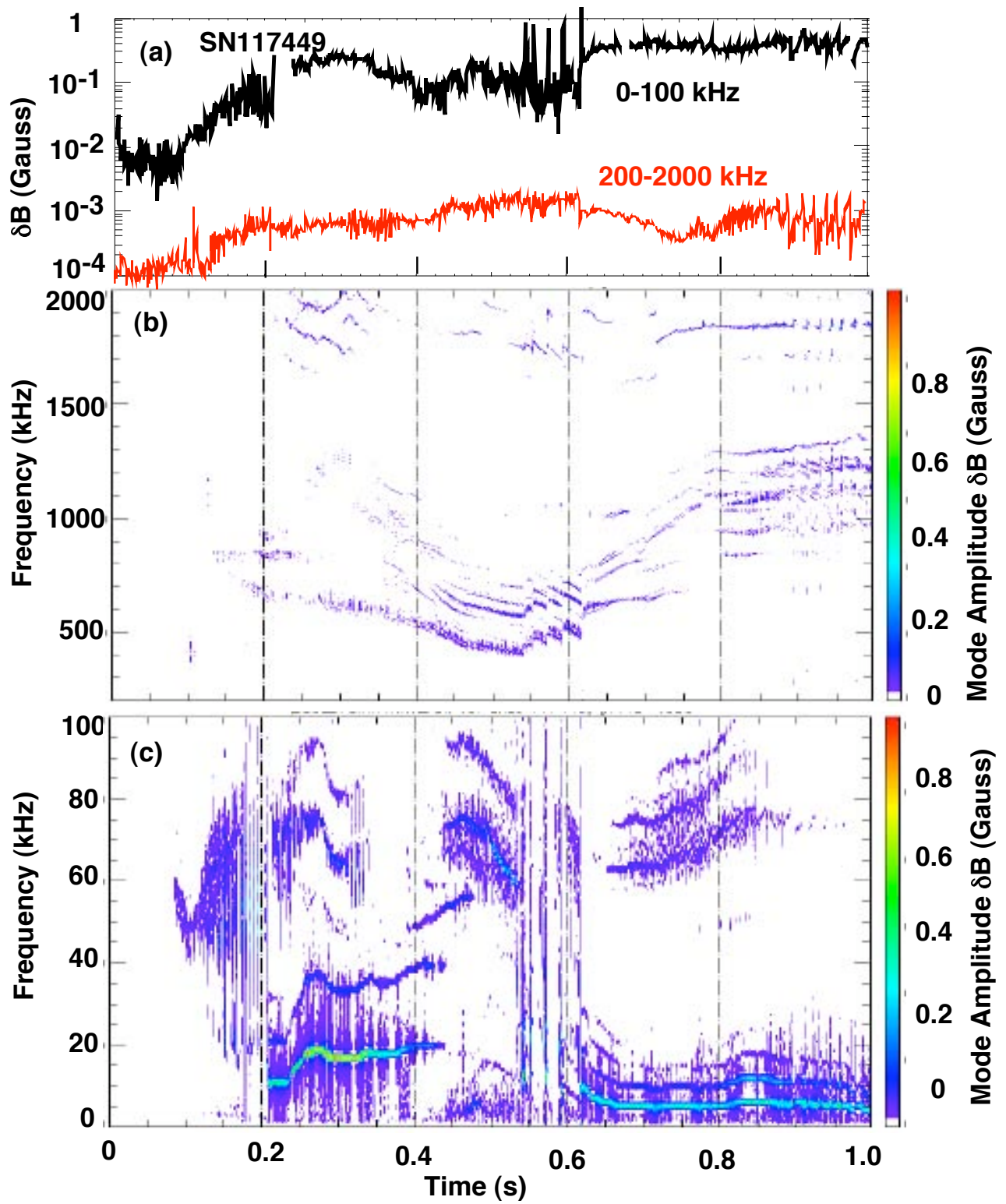


Fig. 25. Mirnov spectrograms for SN117449 covering the high ($f = 200\text{-}2000$ kHz) and low frequency ($f = 0\text{-}100$ kHz) ranges.

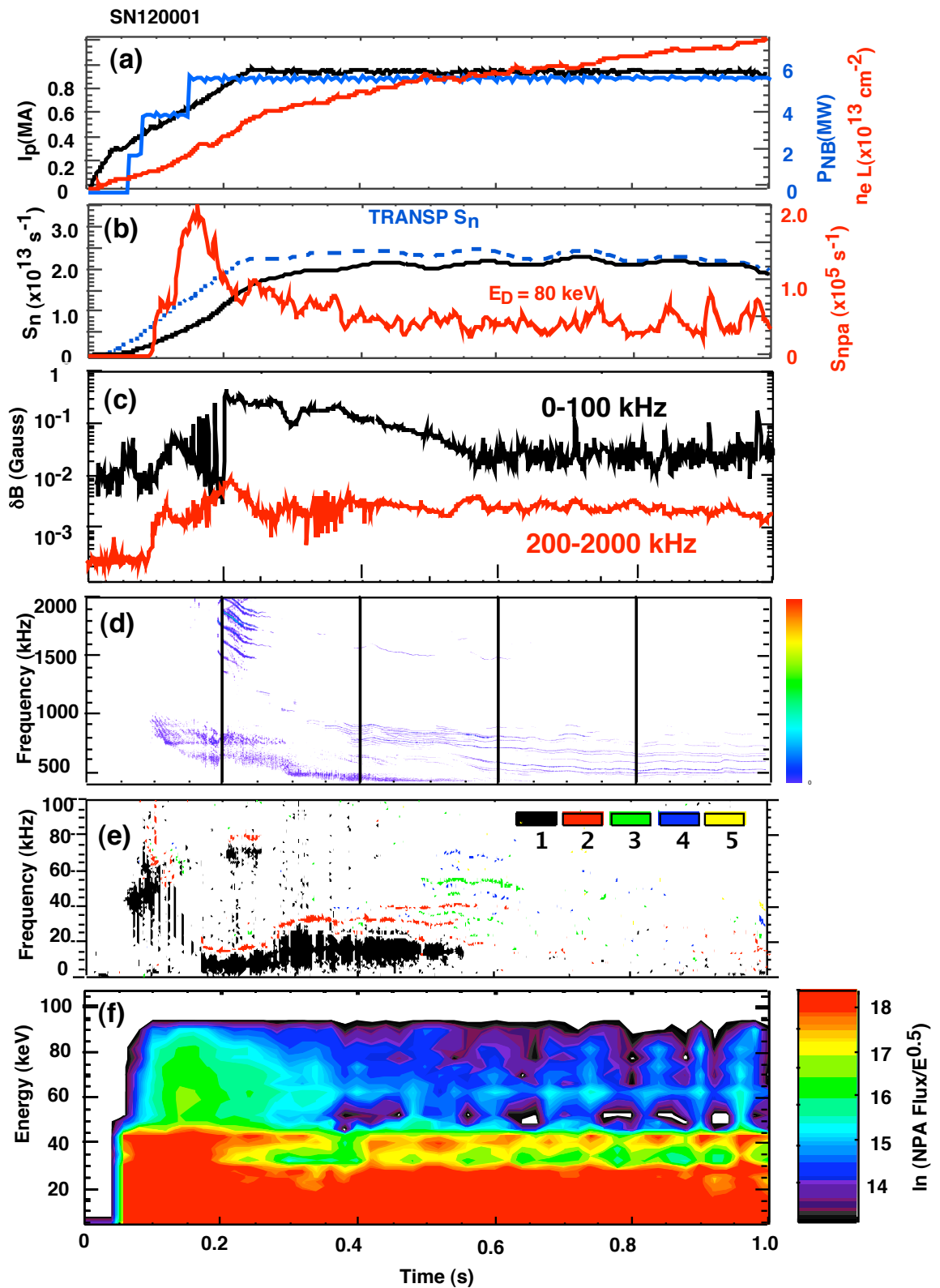


Fig. 26. Selected plasma waveforms and Mirnov spectrogram for SN120001.

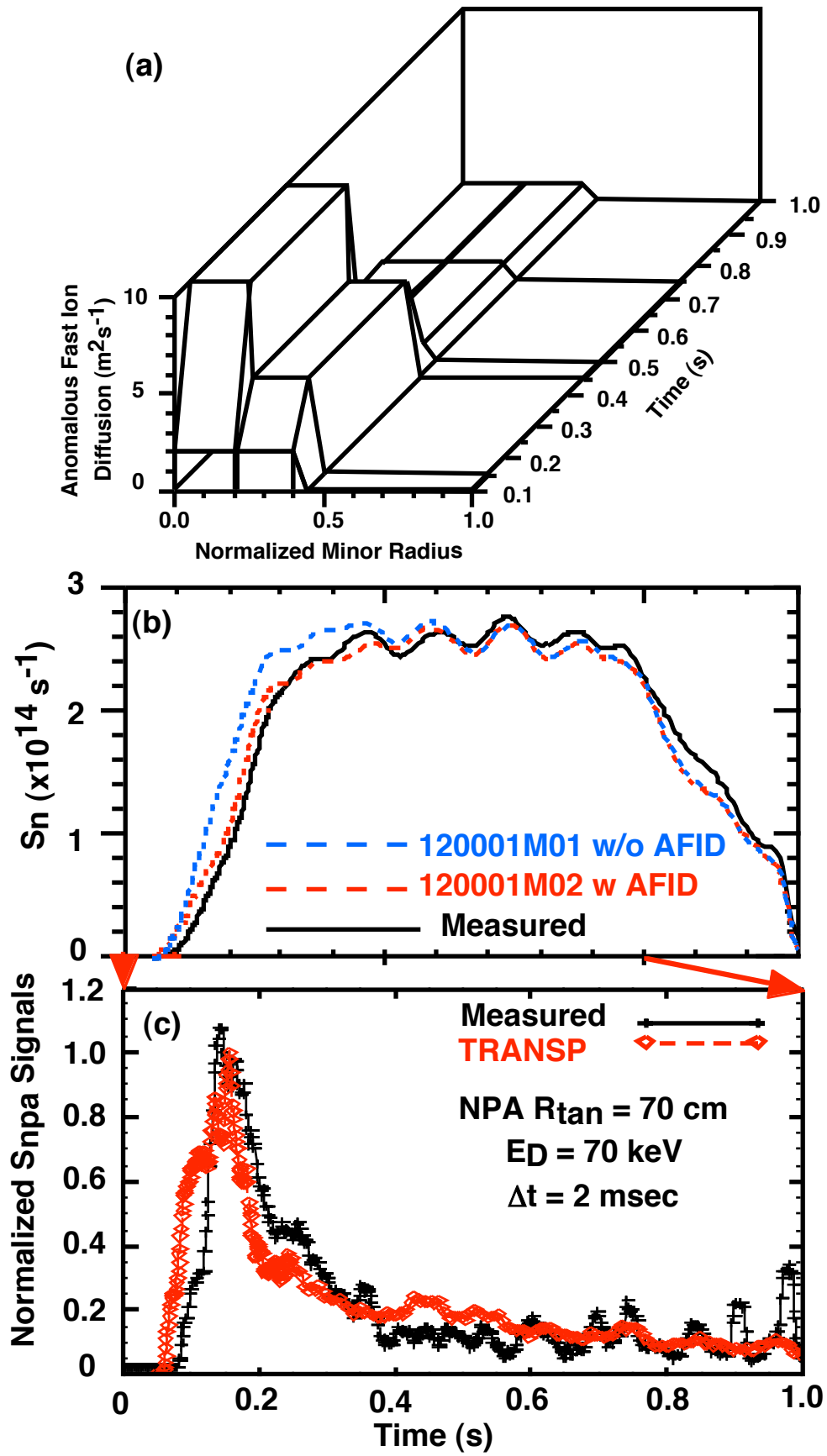


Fig. 27. TRANSP simulation of the neutron yield and NPA signal for SN120001.

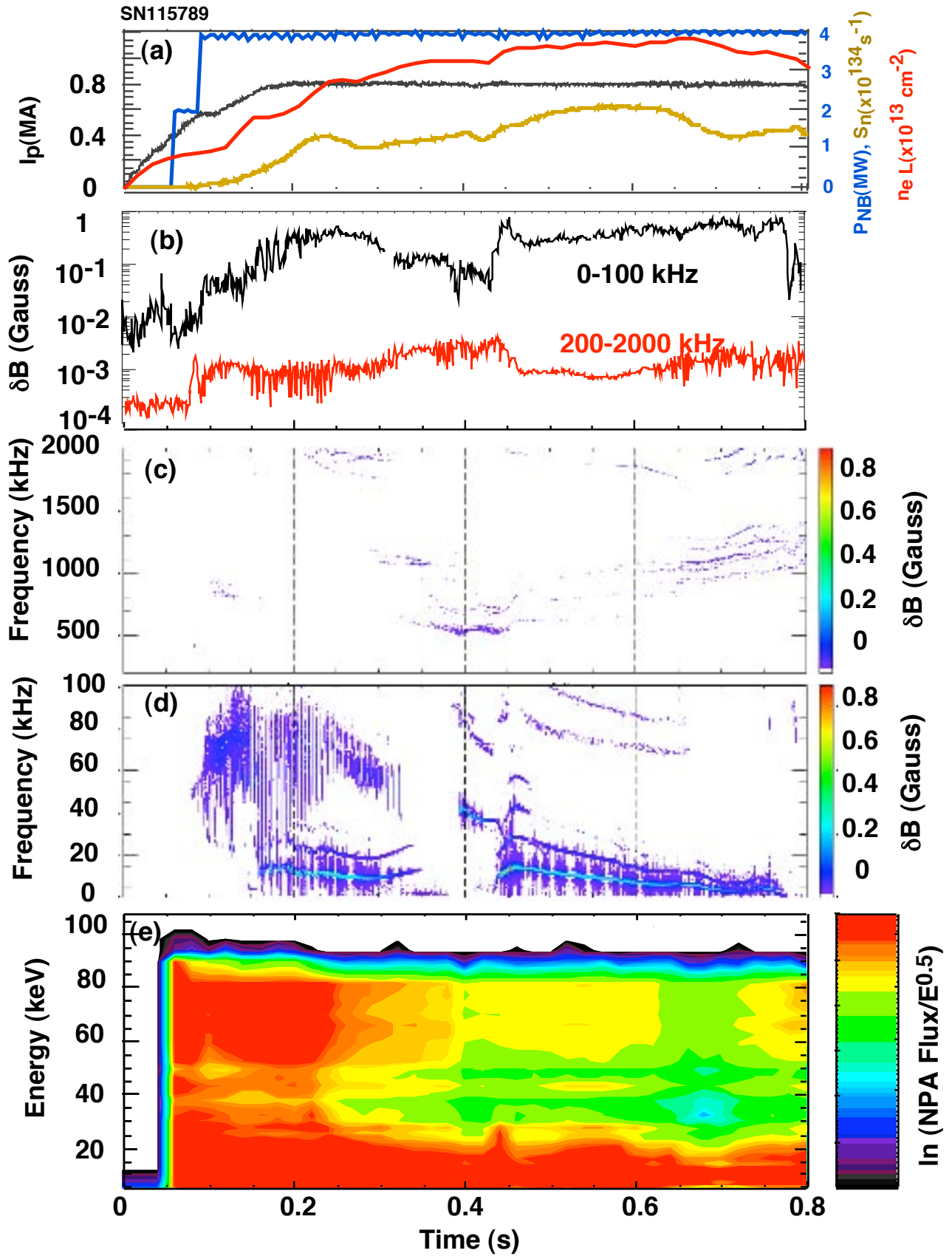


Fig. 28. Measured parameters for SN115789 used in the horizontal NPA scan.

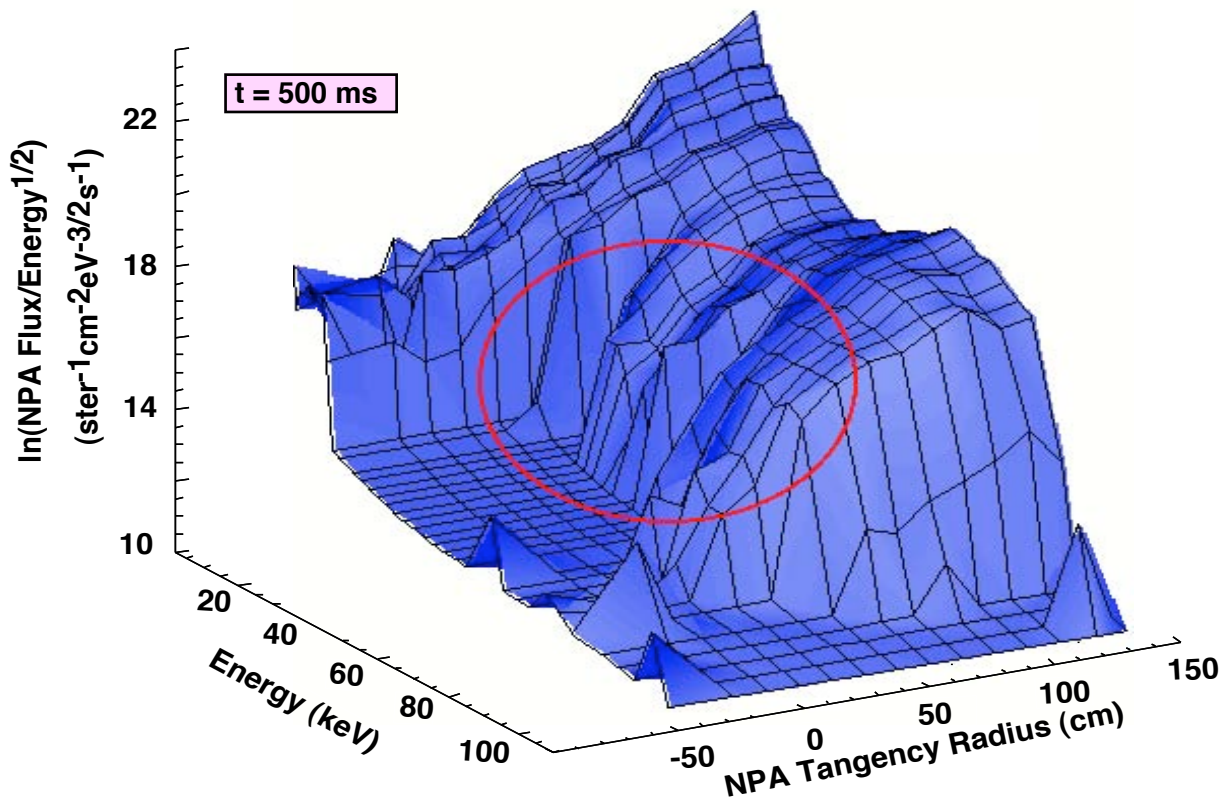
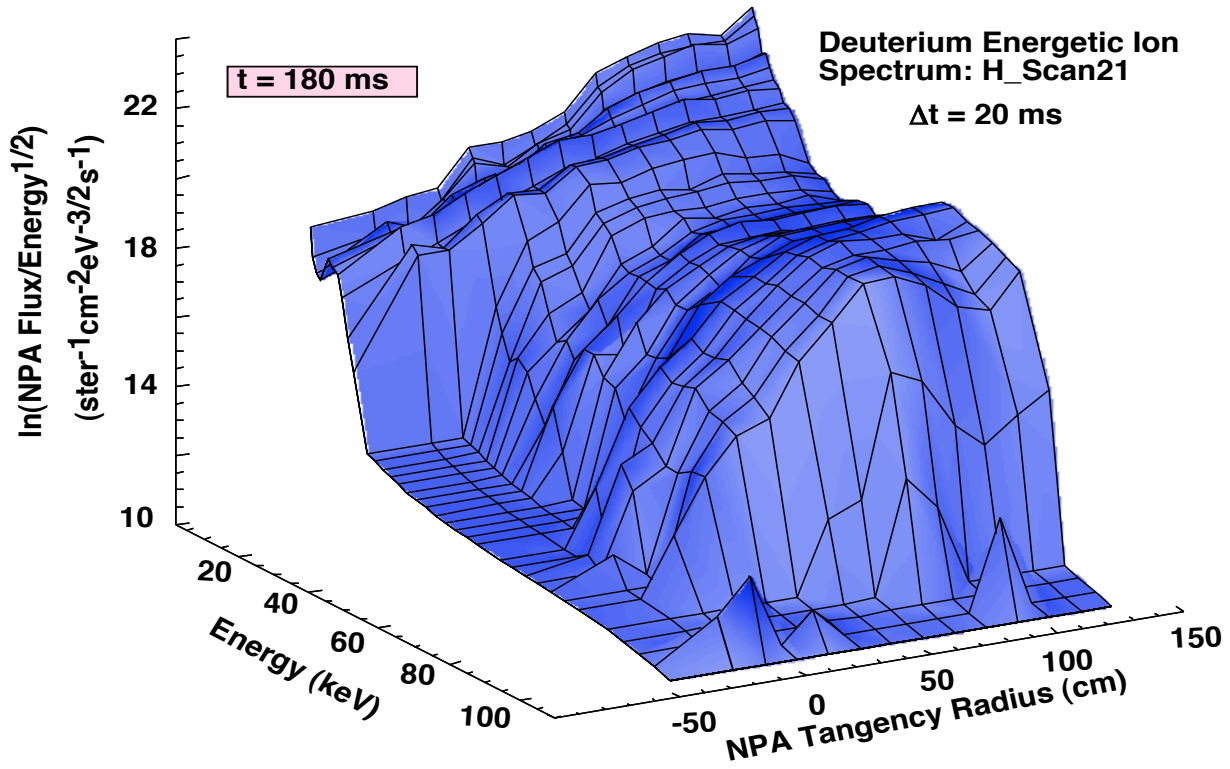


Fig. 29. NPA horizontal scanning measurement of energetic ion redistribution.

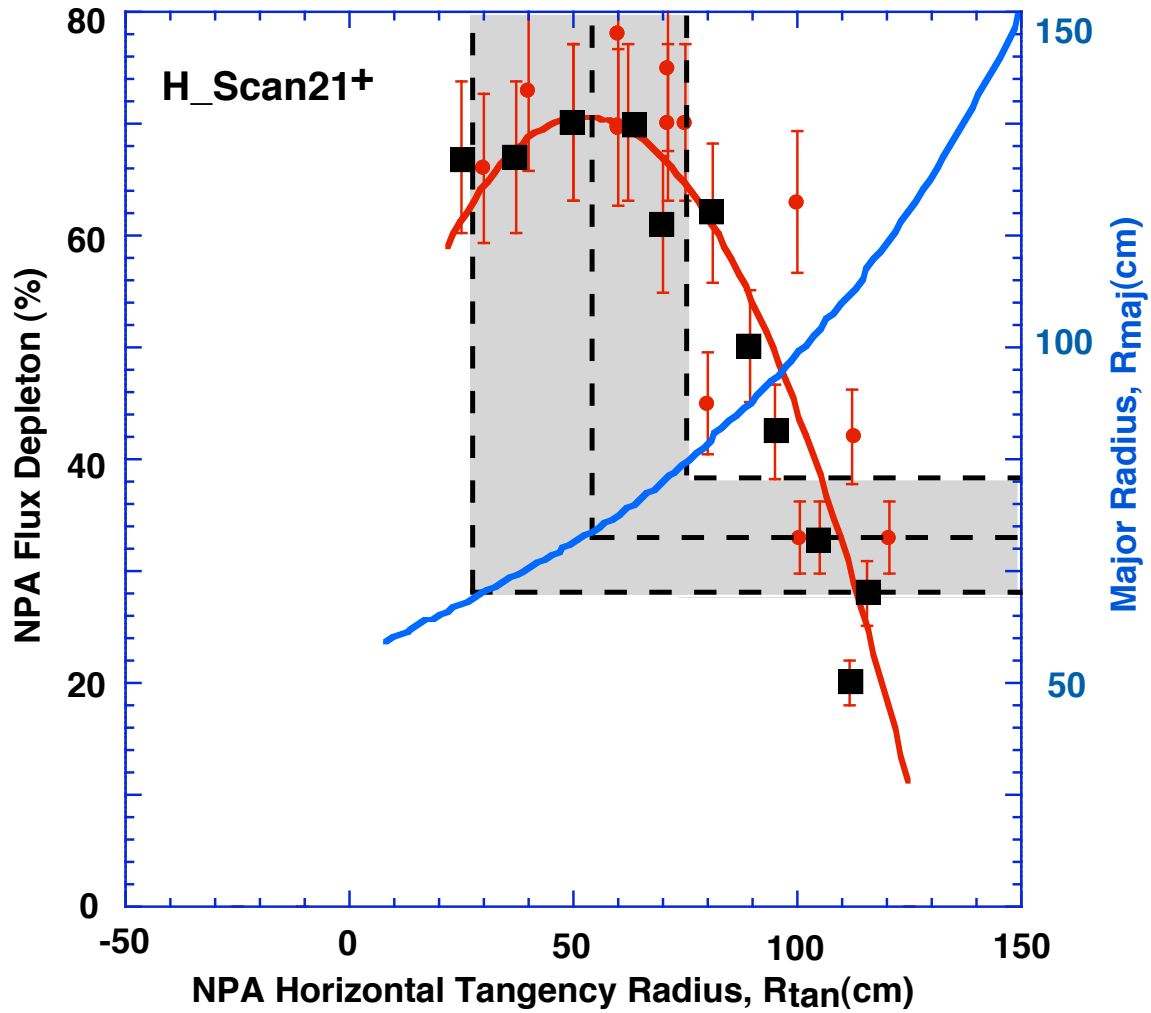
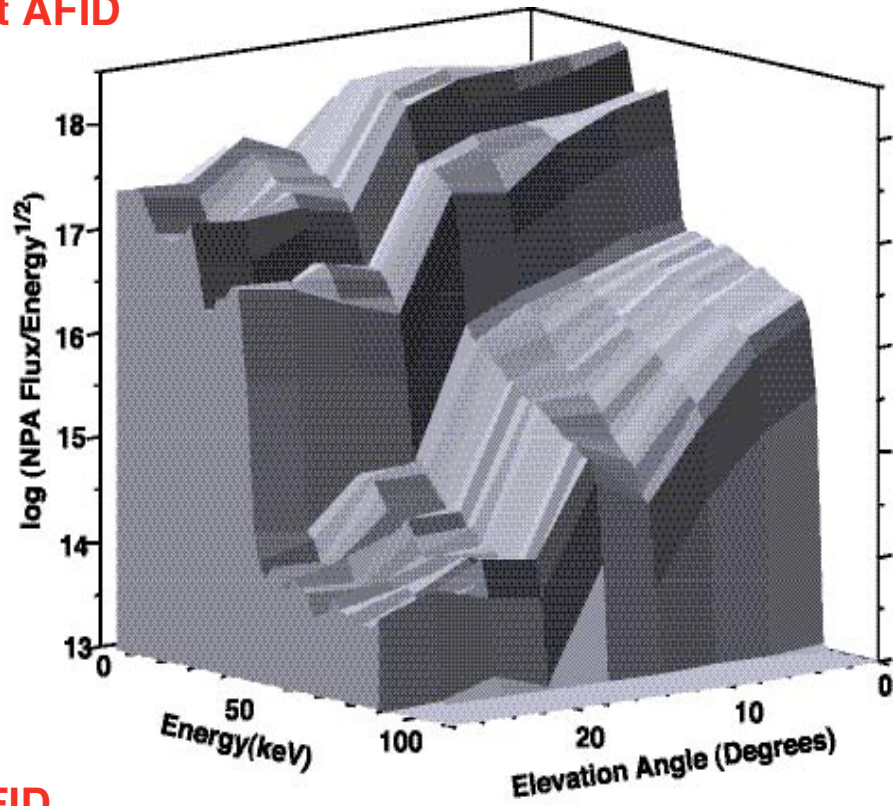


Fig. 30. Depletion of the measured NPA flux is shown as a function of horizontal tangency radius from H_Scan 21 (black points) augmented by other scan data (red points). The blue curve maps the NPA tangency radius to the major radius corresponding to spatial localization of the NPA measurements. The shaded area shows that maximum NPA flux depletion occurs at $R_{tan} \sim 50 \pm 20$ cm corresponding to $R_{maj} \sim 75 \pm 10$ cm. From the upper left panel in Fig. 4a, the energetic ion depletion is associated primarily with passing ions.

Without AFID



With AFID

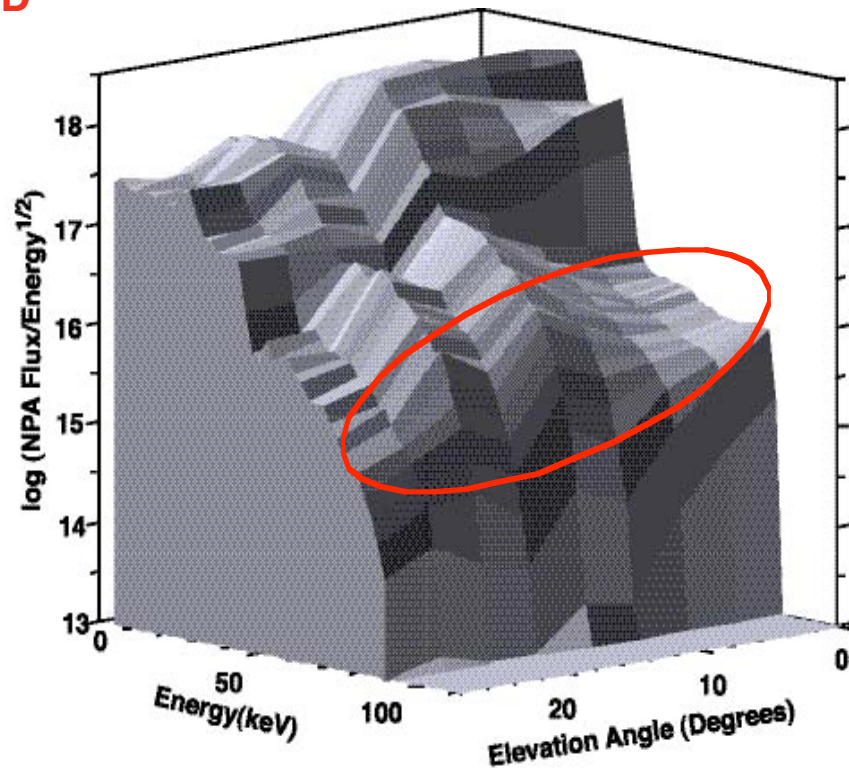


Fig. 31. Comparison of TRANSP ion spectra with and without fast ion diffusion for a simulated NPA vertical scan (118768M22).

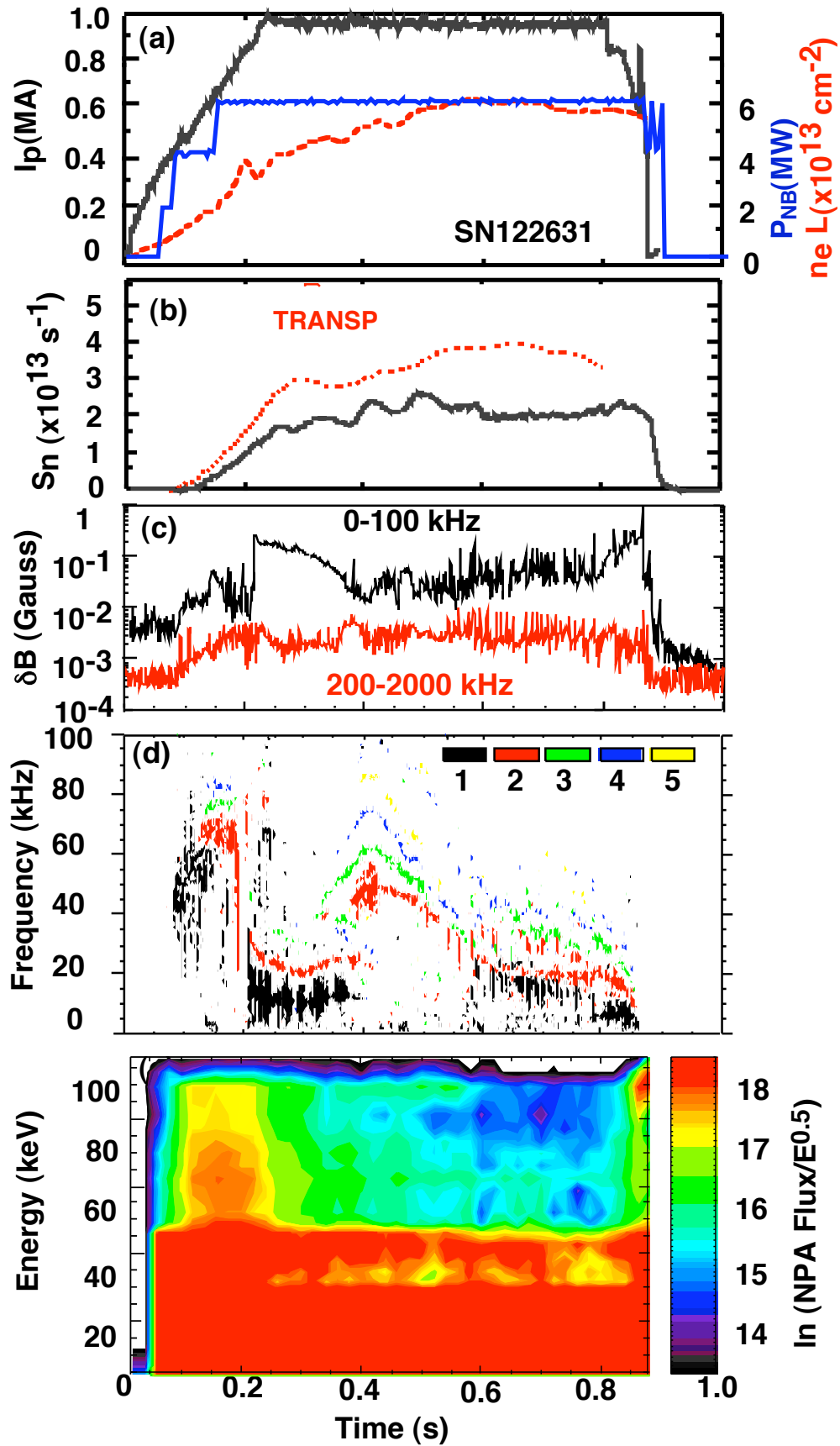


Fig. 32. Discharge characteristics for the NPA vertical scan.

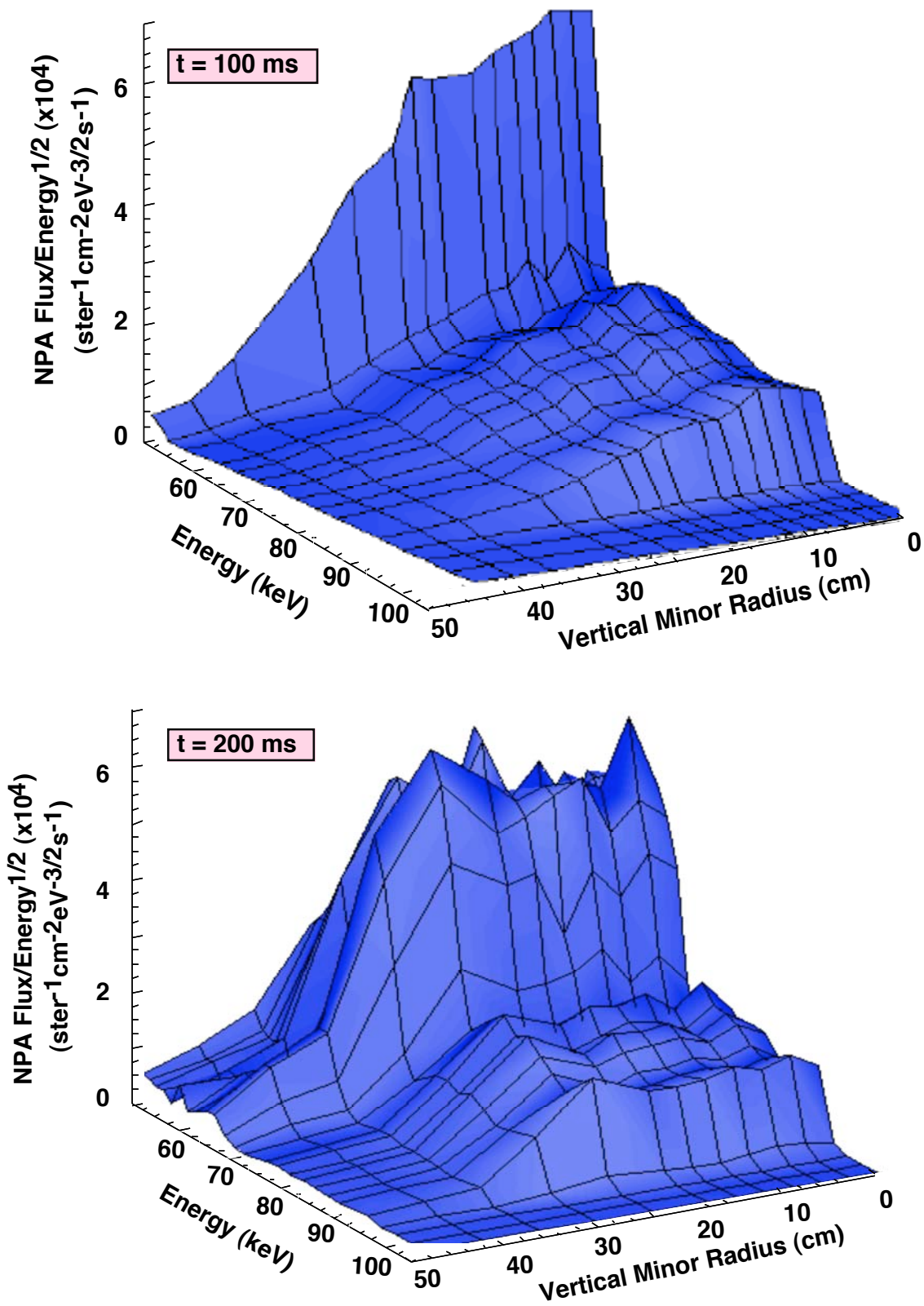


Fig. 33. NPA vertical scan during MHD-quiescent (top panel) and MHD-active (bottom panel) discharge periods.

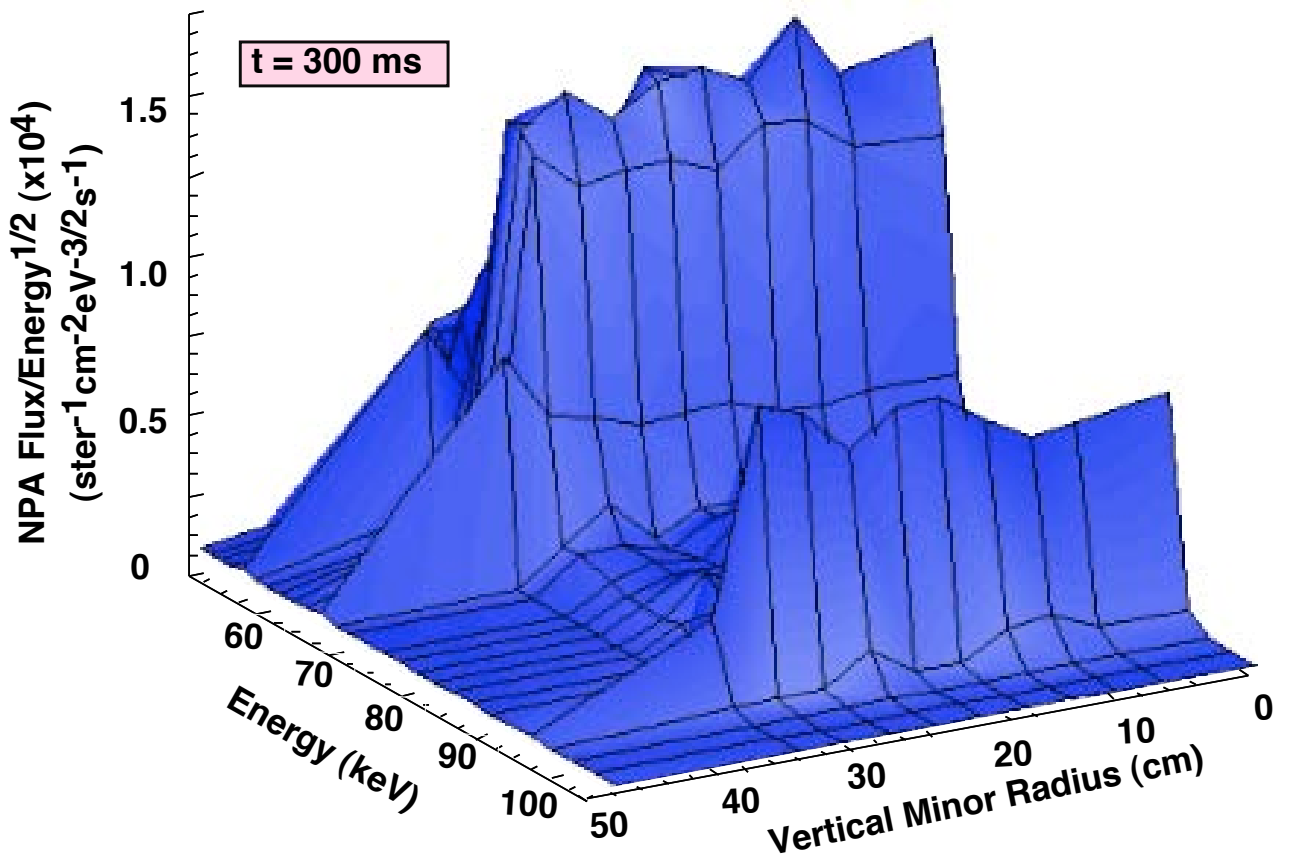


Fig. 34. NPA vertical scan during NBI into a gas-filled torus with toroidal fields only ($B_T = 3.5 - 5.5$ kG), a condition used for calibration of the MSE diagnostic

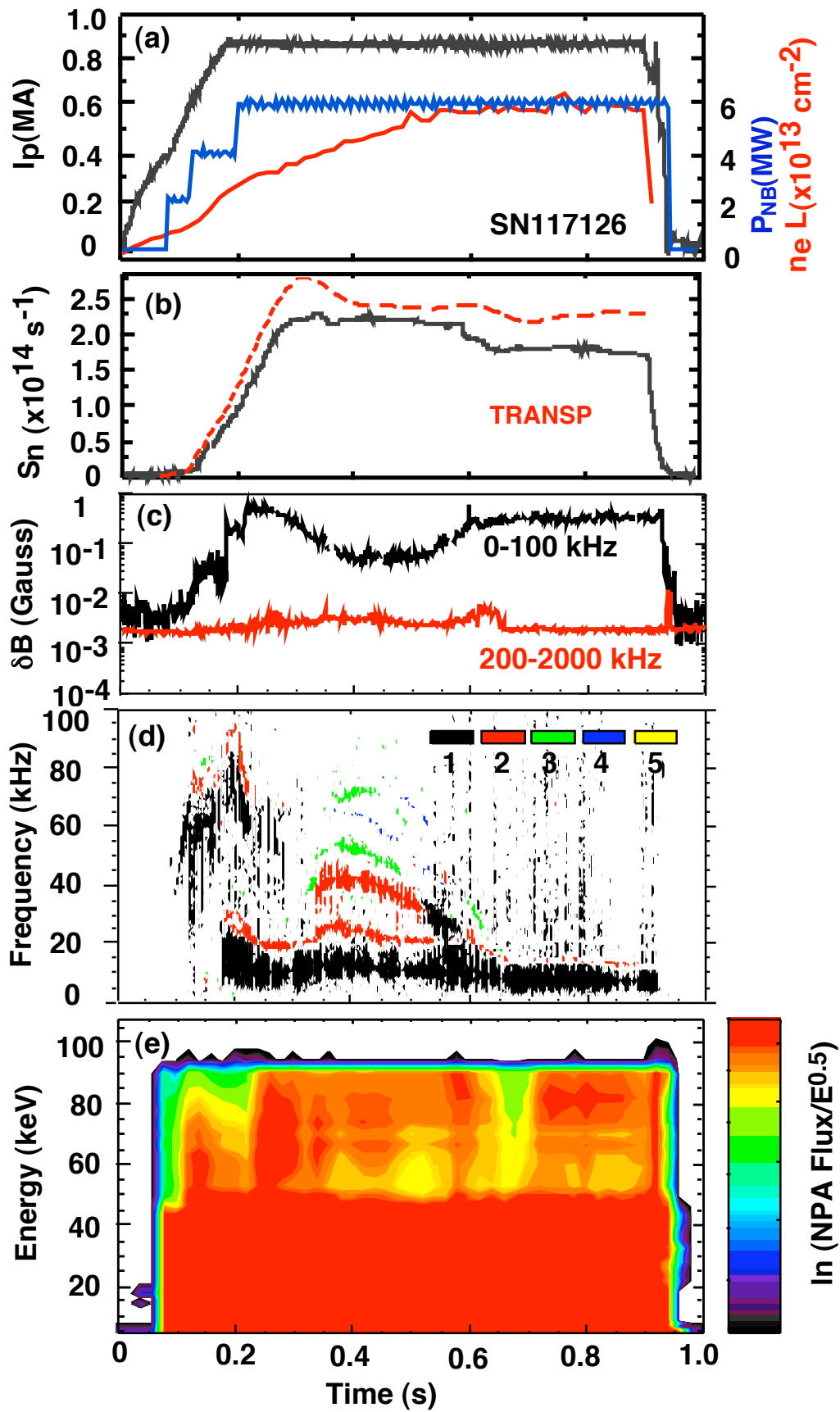


Fig. 35. Discharge characteristics for SN117126.

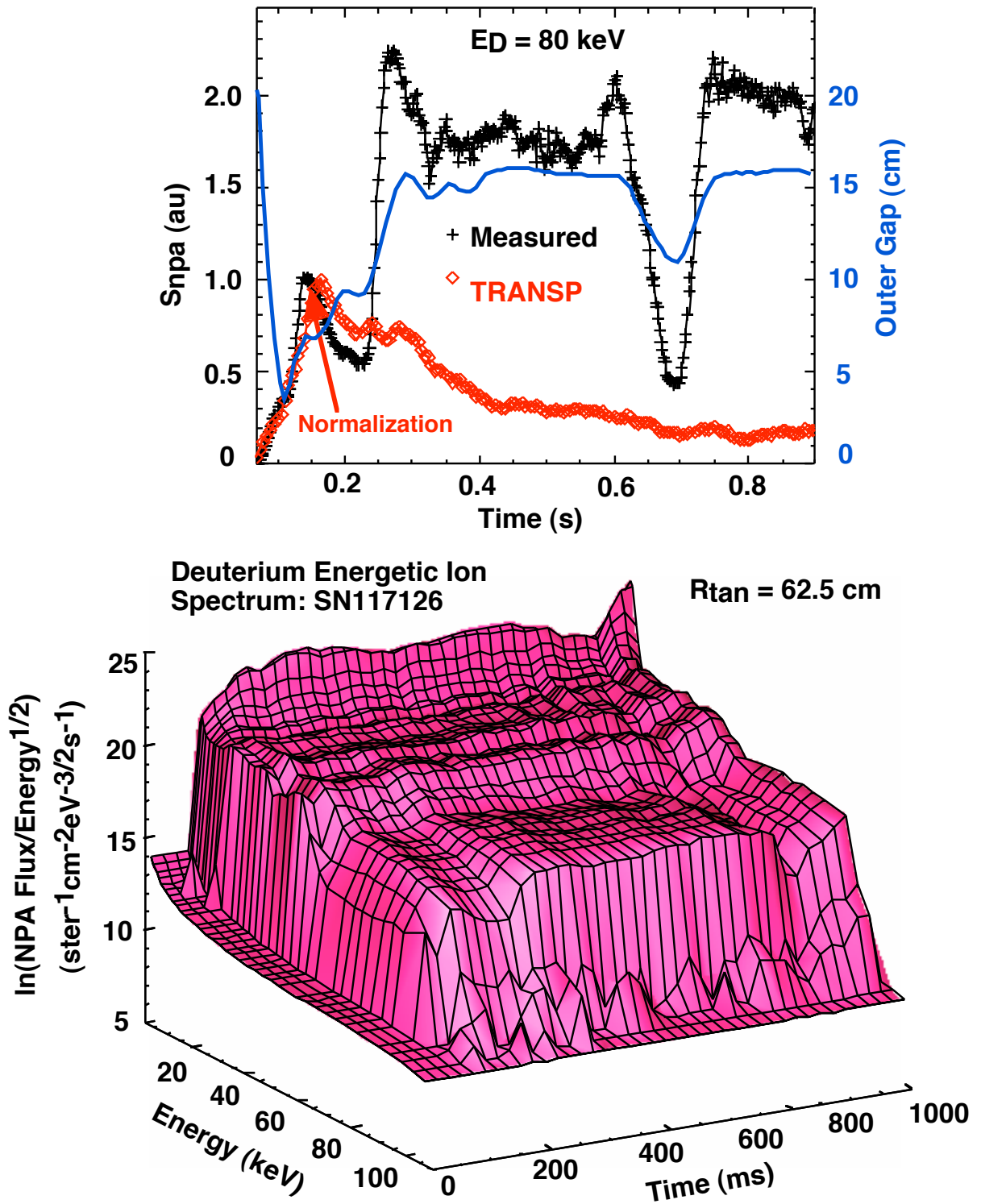


Fig. 36. The top panel shows the normalized measured (black curve) and TRANSP-simulated (red curve) NPA signal evolution and the outer gap width for SN117126. The bottom panel shows the measured energetic ion distribution.

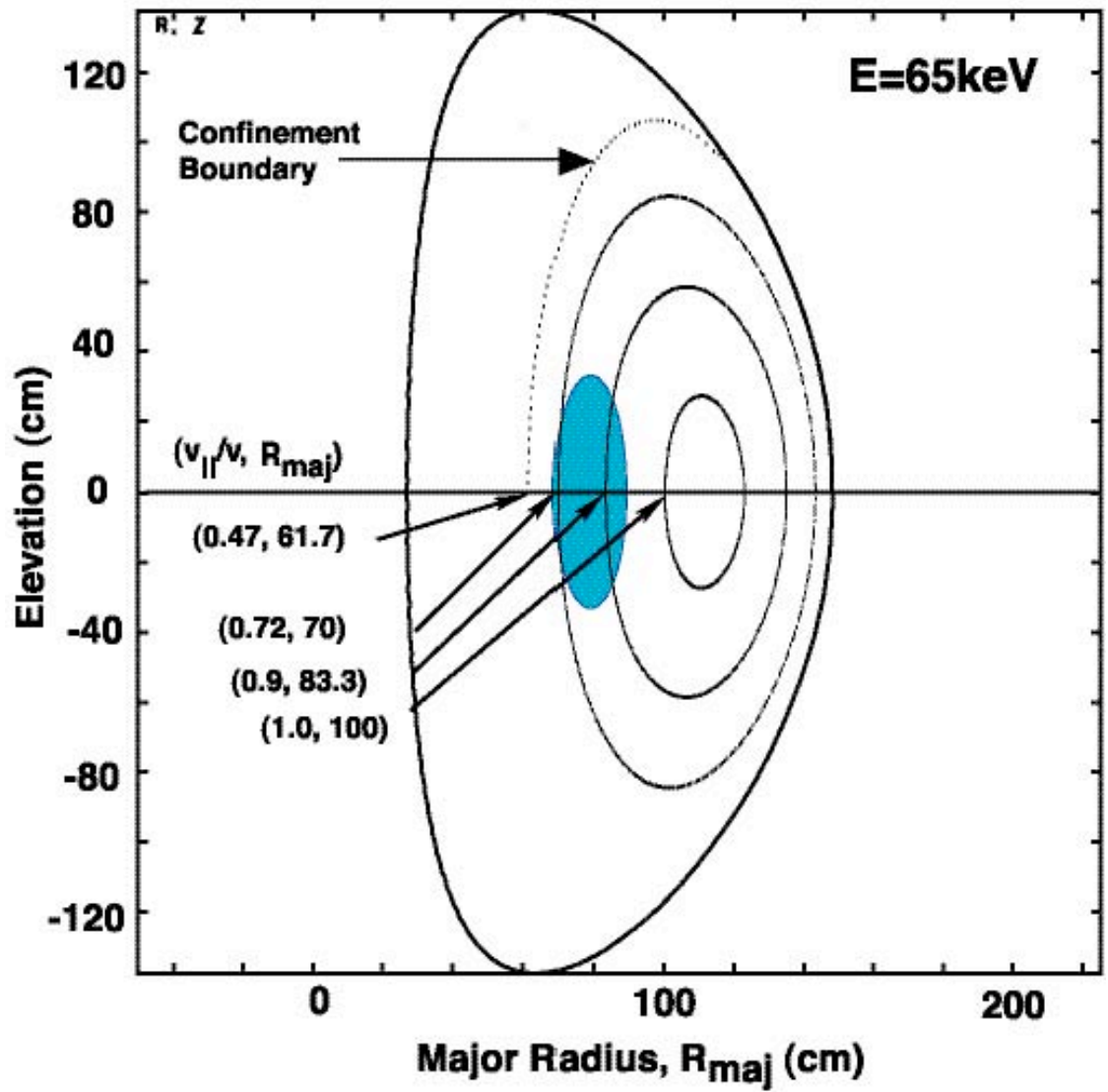


Fig. 37. ORBIT modeling of particle trajectories that are viewed by the NPA diagnostic during horizontal scanning measurements.

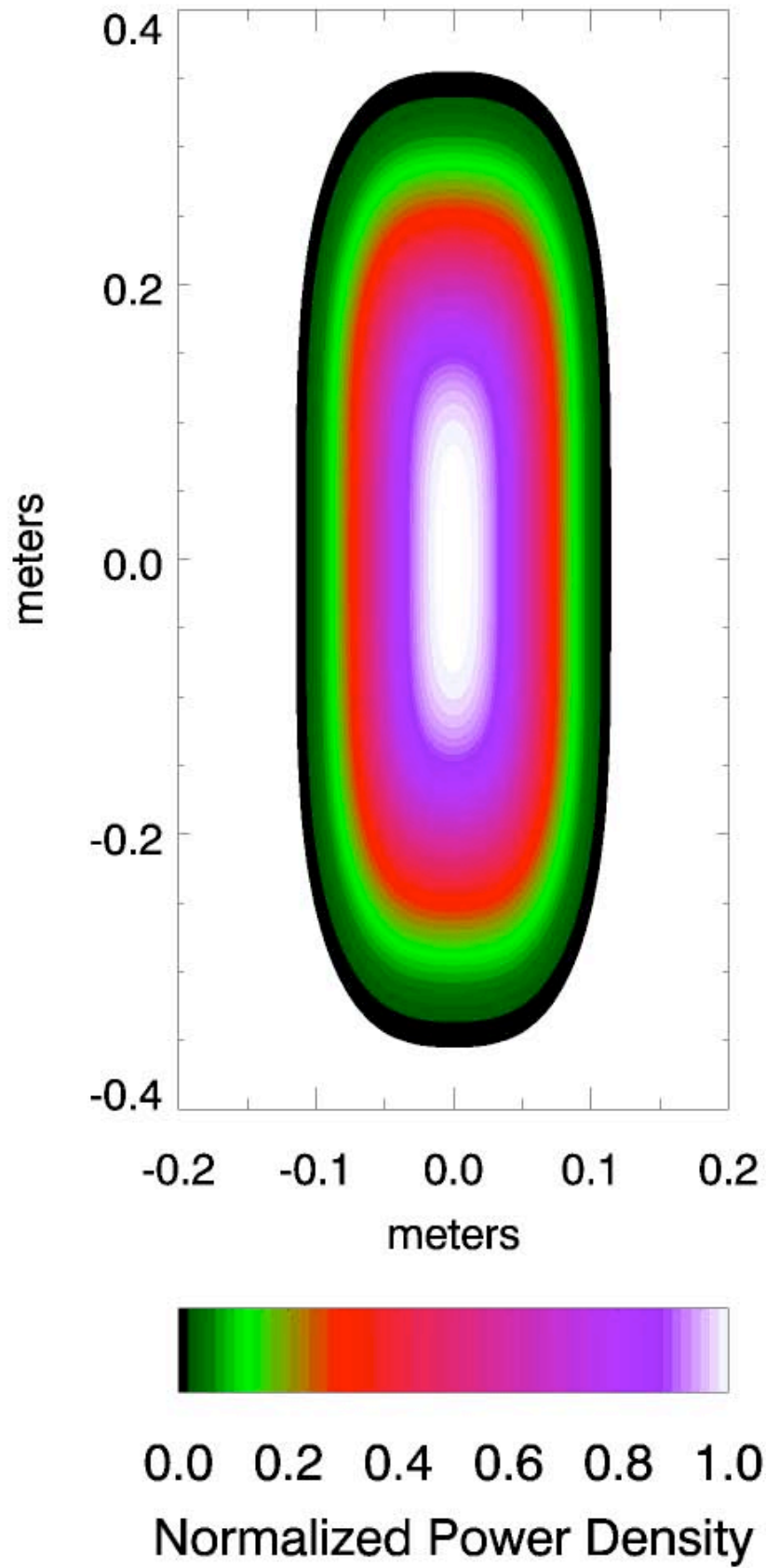


Fig. 38. Contour plot of the primary neutral footprint for an NSTX heating beam.

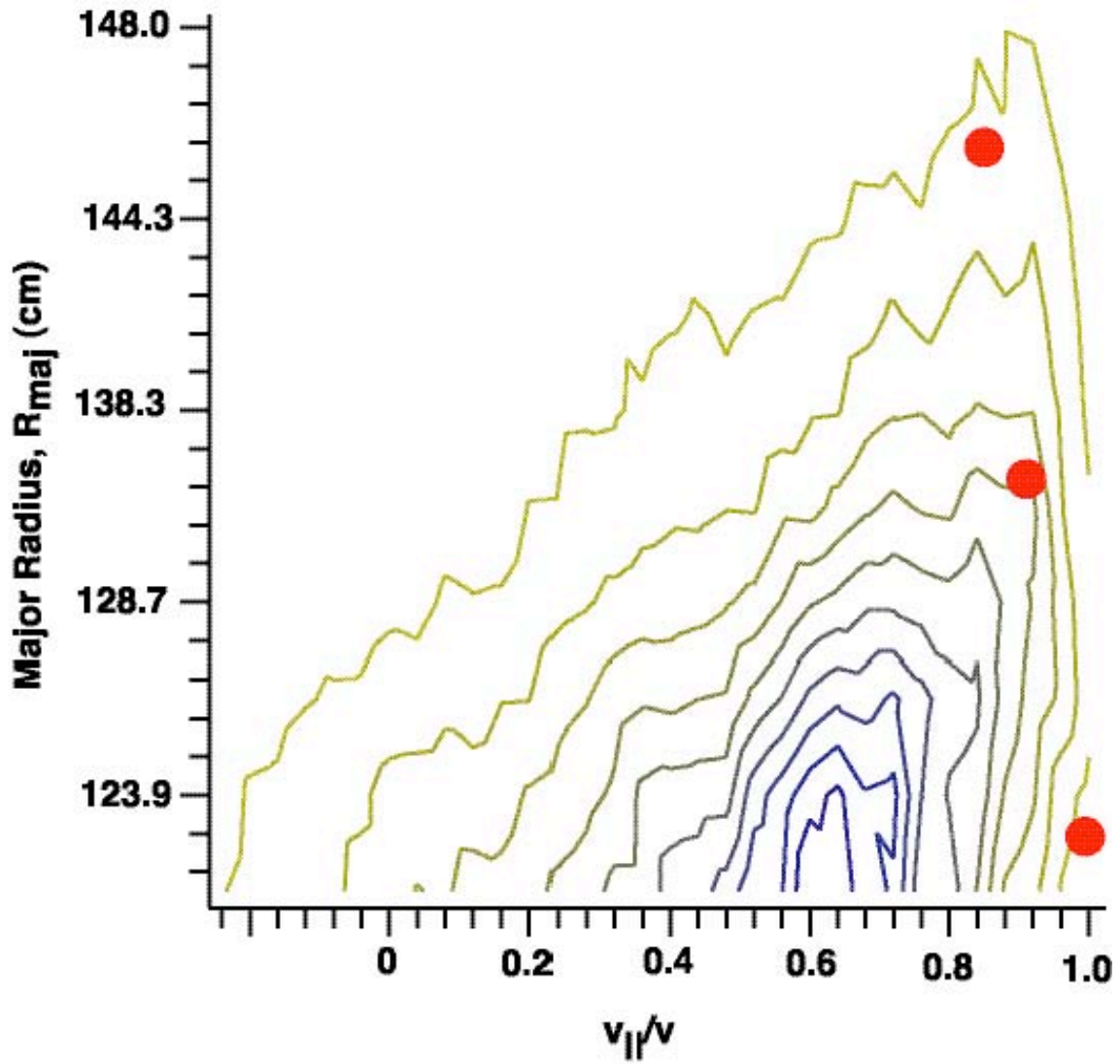


Fig. 39. Contour plot of the beam ion distribution at $E = 65$ keV showing a sample (red circles) of the pitch angles ($v_{||}/v$) that are viewed by the NPA during horizontal scanning.

The Princeton Plasma Physics Laboratory is operated
by Princeton University under contract
with the U.S. Department of Energy.

Information Services
Princeton Plasma Physics Laboratory
P.O. Box 451
Princeton, NJ 08543

Phone: 609-243-2750
Fax: 609-243-2751
e-mail: pppl_info@pppl.gov
Internet Address: <http://www.pppl.gov>